Topology Optimization of 3D Linkages

with application to morphing winglets

T.A. de Jong

Technische Universiteit Delft

Delft University of Technology

Challenge the future

TOPOLOGY OPTIMIZATION OF 3D LINKAGES

WITH APPLICATION TO MORPHING WINGLETS

by

T.A. de Jong

Faculty of Aerospace Engineering

Delft University of Technology

Supervisors:	dr. ir.	R. De Breuker
	ir.	E. Gillebaart

Picture on the cover is taken from reference [26]

DELFT UNIVERSITY OF TECHNOLOGY
DEPARTMENT AEROSPACE STRUCTURES AND MATERIALS (ASM)

The undersigned hereby certify that they have read and recommend to the Faculty of Aerospace Engineering for acceptance a thesis entitled:

TOPOLOGY OPTIMIZATION OF 3D LINKAGES

WITH APPLICATION TO MORPHING WINGLETS

by
Twan de Jong

in partial fulfilment of the requirements for the degree of Master of Science

GRADUATION COMMITTEE

Committee chairman:
Dr. S. R. Turteltaub, MSc

Signature

Date

Committee member:
Dr. Ir. R. Vos

Signature

Date

Committee member:
Dr. Ir. R. De Breuker

Signature

Date

Committee member:
Ir. E. Gillebaart

Signature

Date

ACKNOWLEDGEMENTS

I would like to start by thanking both Roeland and Erik for their daily supervision. Their experience in the field of morphing structures has been very valuable during the nine months of my thesis. I enjoyed the fruitful discussions during our biweekly meetings. In addition, I would like to thank the Sergio Turteltaub and Roelof Vos for their willingness to participate in my graduation committee.

My thesis would have not have been the same without Ron, Johan, Adriaan, and Maarten. As fellow thesis students they have proven both valuable in discussions as well as friends during the breaks.

Also, the support from my family, friends, and girlfriend was very useful. During the nine months they have seen my progress, including its ups and downs, and could cheer me up when needed.

Finally, a special thanks to Ron and Johan for taking the time to read through my thesis. I appreciated and incorporated the feedback to improve my thesis.

Thank you,
Twan de Jong

ABSTRACT

Topology optimization is the process of optimizing both the material layout and the connectivity inside a design domain [56]. The first paper on topology optimization dates back to 1904, when the Australian inventor Michell derived optimality criteria for minimum weight truss structures [48]. In 1988 Bendsøe and Kikuchi [4] published the pioneering paper "Homogenization approach to topology optimization", laying the foundation of numerical optimization methods for topology optimization. Since then, extensive research has been performed both in academia and industry trying to solve different topology optimization problems.

Due to its general applicability, topology optimization has been applied to the design of many morphing aircraft structures including morphing leading edges [41, 50, 61, 66, 73], trailing edges [1, 19, 53, 69], or both [44]. It has also been applied to complete morphing wings [14, 27, 28, 58, 59]. Morphing structures have the ability to change their shape throughout the flight. This allows for possible weight savings and/or drag reduction, resulting in a reduced fuel consumption. Despite the great interest in morphing winglets from both Airbus and Boeing, topology optimization has not yet been used to design morphing winglets, except for previous work done by E. Gillebaart and R. De Breuker [21]. This thesis continues with the research by focusing on the following research objective:

> *"Developing a software tool to design a mechanism for morphing winglets, using ground-structure based topology optimization, by improving, extending, and expanding the previous 2D inhouse tool."*

The research in this thesis is based on previous work done by the faculty. The previous 2D tool is improved, its capabilities are extended and the tool is expanded to 3D. The current tool effectively demonstrates how topology optimization, based on the ground-structure approach, can be used to obtain mechanisms for morphing winglets. A two step optimization strategy is formulated, where the mechanism is designed in the first step and sized to obtain minimum weight in the second step. Both optimizations are done using the globally convergent method of moving asymptotes (GCMMA) optimizer, combined with the adjoint sensitivity technique. Due to the large rotations of the winglet, geometric non-linearity is taken into account using the Green-Lagrange strain measure.

Various mechanisms for morphing winglets were successfully designed and sized both in 2D and in 3D. In 2D mechanisms were found where the cant angle could be regulated, in 3D mechanisms were found where both the cant angle and the toe angle could be regulated. An aerodynamic load case of 5 [kN] was defined. In 2D half of this loading was assumed to act on the mechanism, resulting in a minimum weight of 15.0 [kg]. In 3D the minimum weight was found to be 48.0 [kg].

CONTENTS

LIST OF FIGURES

LIST OF ABBREVIATIONS

AaM	**A**eroelasticity **a**nd **M**orphing
BWB	**B**lended **W**ing **B**ody
CCSA	**C**onservative **C**onvex **S**eparable **A**pproximation(s)
DOF	**D**egree(s) **O**f **F**reedom
ESO	**E**volutionary **S**tructural **O**ptimization
FEA	**F**inite **E**lement **A**nalysis
FEM	**F**inite **E**lement **M**ethod
GA	**G**enetic **A**lgorithm
GCMMA	**G**lobally **C**onvergent **M**ethod of **M**oving **A**symptotes
GL	**G**reen-**L**agrange
HECS	**H**yper-**E**lliptic **C**ambered **S**pan
KKT	**K**arush-**K**uhn-**T**ucker
LM	**L**evenberg-**M**arquardt
LSE	**L**east **S**quare **E**rror
MBB	**M**esserschmitt-**B**ölkow-**B**lohm
MDO	**M**ulti**d**isciplinary **O**ptimization
MIMO	**M**ultiple-**I**nput-**M**ultiple-**O**utput
MISO	**M**ultiple-**I**nput-**S**ingle-**O**utput
MMA	**M**ethod of **M**oving **A**symptotes
MOPBIL	**M**ulti-**O**bjective **P**opulation-**B**ased **I**ncremental **L**earning
RAMP	**R**ational **A**pproximation of **M**aterial **P**roperties
SCP	**S**equential **C**onvex **P**rogramming
SIMP	**S**olid **I**sotropic **M**aterial with **P**enalization
SISO	**S**ingle-**I**nput-**S**ingle-**O**utput
SRV	**S**um of **R**eciprocal **V**ariables
SSV	**S**um of **S**quares of **V**ariables
TO	**T**opology **O**ptimization
TPE	**T**otal **P**otential **E**nergy
UAV	**U**nmanned **A**ir **V**ehicle

LIST OF SYMBOLS

Greek Symbols

α_{in}	Minimum connectivity correction factor
α_{max}	Minimum volume correction factor
γ_{cr}	Ith critical buckling load factor
$\boldsymbol{\gamma}$	Rotation vector
Δ	Downward deflection
Δ	Distance between actual and intended nodal location
Δ^{max}	Maximum allowable distance between actual and intended nodal location
$\boldsymbol{\delta}$	Rotation vector
ϵ	Strain
ϵ_i	Strain of ith element
$\boldsymbol{\eta}$	Vector with Lagrange multipliers
λ_{cr}	Ith critical buckling load factor
λ_i	Ith buckling load factor
$\boldsymbol{\lambda}$, $\boldsymbol{\lambda}_1$, $\boldsymbol{\lambda}_2$, $\boldsymbol{\lambda}_3$, $\boldsymbol{\lambda}_4$	Vector with Lagrange multipliers
μ	Levenberg-Marquardt scaling parameter
Π	Total potential energy
ρ_i	Cross-sectional area design variable
ρ_{min}	Minimum cross-sectional area
ρ^m	Material density
$\boldsymbol{\rho}$	Vector containing design variables
σ_i	stress in ith element
σ_y	Yield stress
$\boldsymbol{\phi}_{cr}$	Ith eigenvector describing the critical eigenmode
$\boldsymbol{\phi}_i$	Eigenvector describing the ith eigenmode
Ω	Design space

Latin Symbols

A	Cross-sectional area
A_0	Maximum/original cross-sectional area
A_i	Cross-sectional area of ith element
$\boldsymbol{a}$	Volume vector
$\boldsymbol{A}$	Vector with cross-sectional areas
$\boldsymbol{b}$	$\hat{\boldsymbol{B}}\ \boldsymbol{x}$
$\boldsymbol{b}_i$	$\hat{\boldsymbol{B}}_i\ \boldsymbol{x}$
$\boldsymbol{B}$	Strain rotation matrix
$\hat{\boldsymbol{B}}$	Strain rotation matrix with rows of fixed degrees of freedom removed
$\tilde{\boldsymbol{B}}$	Strain rotation matrix with rows and columns of fixed degrees of freedom removed
$\boldsymbol{B}_i$	Strain rotation matrix of ith element
$\hat{\boldsymbol{B}}_i$	Strain rotation matrix with rows of fixed degrees of freedom removed of ith element
$\tilde{\boldsymbol{B}}_i$	Strain rotation matrix with rows and columns of fixed degrees of freedom removed of ith element
C	Compliance

$C_{input\ node}$	Connectivity at the input node
$C^{min}_{input\ node}$	Minimum connectivity at the input node
D_i	Distance between actual and intended trajectory squared
E	Young's modulus
E_0	Maximum/original cross-sectional Young's Modulus
E_i	Young's modulus of ith element
F_0	Objective function
F_i^{input}	Reaction force at the ith input node
$\boldsymbol{F}$	Force vector
$\boldsymbol{F}_{ext}$	External force vector
$\boldsymbol{F}_{int}$	Internal force vector
g	Levenberg-Marquardt gain factor
G_j	Jth constraint
$\tilde{G}_j$	Approximation of jth constraint
$G_j^{global\ buckling}$	Jth global buckling constraint
$G_j^{input\ node}$	Jth input node connectivity constraint
$G_j^{trajectory}$	Jth trajectory constraint
$G^{local\ buckling}$	Local buckling constraint
$G^{stress\ compression}$	Compression stress constraint
$G^{stress\ tension}$	Tension stress constraint
G^{volume}	Volume constraint
$\boldsymbol{h}$	Direction of descent vector
I	Second moment of area
I_i	Second moment of area of ith element
$\boldsymbol{J}_f$	Jacobian
k	Spring stiffness of truss member
K_s	Scaling parameter for Kreisselmeier-Steinhauser function
$\boldsymbol{K}_G$	Geometric stiffness matrix
$\boldsymbol{K}_H$	Higher order stiffness matrix
$\boldsymbol{K}_L$	Linear stiffness matrix
$\boldsymbol{K}_t$	Tangent stiffness matrix
l	Undeformed length
$\hat{l}$	Deformed length
l_i	Undeformed length of ith element
$\hat{l}_i$	Deformed length of ith element
L	Lower moving asymptote
M	Total number of constraints
N	Total number of design variables
N_{buckl}	Total number of global buckling constraints per step
N_c	Total number of compression stress constraints
N_d	Total number of free degrees of freedom
N_e	Total number of elements
N_{in}	Total number of input nodes
N_{lb}	Total number of local buckling constraints
N_n	Total number of nodes
N_{out}	Total number of output nodes
N_s	Total number of steps
N_t	Total number of tension stress constraints
p	Penalty factor
P_i^{cr}	Critical column buckling load for the ith element
$\boldsymbol{p}$	Nodal (external) force vector
Q	Taylor series approximation of the potential energy
$R_j^{global\ buckling}$	Critical buckling load factor of jth constraint
$R_j^{input\ node}$	Ratio of $C_{input\ node}$ over $C^{min}_{input\ node}$ of jth constraint

$R_j^{trajectory}$	Ratio Δ over Δ^{max} of jth constraint
$R_i^{local\ buckling}$	Ratio of elemental force of ith element over P_i^{cr}
R_i^{stress}	Ratio of elemental stress of ith element over yield stress
R^{volume}	Ratio of V over V^{max}
$\boldsymbol{R}$	Residual force vector
$\boldsymbol{R}^{(L)}$	Residual force vector from the second (linear) step of the finite element analysis
$\boldsymbol{R}^{(NL)}$	Residual force vector from the first (non-linear) step of the finite element analysis
u_x^{act}	Actual x-displacement of the output node
u_y^{act}	Actual y-displacement of the output node
u_z^{act}	Actual z-displacement of the output node
u_x^{traj}	Target x-displacement of the output node
u_y^{traj}	Target y-displacement of the output node
u_z^{traj}	Target x-displacement of the output node
U	Internal strain energy
U	Upper moving asymptote
$\boldsymbol{u}$	Displacement vector
$\boldsymbol{\Delta u}$	Displacement increment vector
$\boldsymbol{u}^{(L)}$	Displacement vector from the second (linear) step of the finite element analysis
$\boldsymbol{u}^{(NL)}$	Displacement vector from the first (non-linear) step of the finite element analysis
V	Work done by external forces
V	Total volume
V^{max}	Maximum volume
w_i	Weighting factor of ith load case
W	Weight
x_{max}	Upper bound design variable
x_{min}	Lower bound design variable
$\boldsymbol{x}$	Nodal location vector

1

INTRODUCTION

Topology optimization is the process of optimizing both the material layout and the connectivity inside a design domain [56]. The first paper on topology optimization dates back to 1904, when the Australian inventor Michell derived optimality criteria for minimum weight truss structures [48]. The author and his research group extended the Michell's theory to beam systems and presented the first general theory for topology optimization in the 1970s, see [48] for the contributing papers. In 1988 Bendsøe and Kikuchi [4] published the pioneering paper "Homogenization approach to topology optimization", laying the foundation of numerical optimization methods for topology optimization. Since then, extensive research has been performed both in academia and industry trying to solve different topology optimization problems.

Due to its general applicability, topology optimization has been applied to many different disciplines, including civil engineering, material science, automotive, and aerospace engineering. Within aerospace engineering extensive research has been done on how topology optimization can be used to design aircraft structures. Morphing aircraft structures are structures with the ability to change their shape, which potentially increases the structural and aerodynamic efficiency. With the continuous drive to decrease the aircraft weight, extensive research is performed on morphing aircraft structures via topology optimization. Many papers have been published where topology optimization has been used to design morphing leading edges [41, 50, 61, 66, 73], trailing edges [1, 19, 53, 69], or both [44]. It has also been applied to entire morphing wings [14, 27, 28, 58, 59], as well as to flexible skins [29].

Despite the fact that topology optimization is often applied to design morphing aircraft structures, it has hardly been applied to design morphing winglets. To the author's best knowledge only E. Gillebaart and R. De Breuker have done research in this field [21], most of the research on the design of morphing winglets does not involve topology optimization [5–8, 15–17, 22–24, 52, 60, 68, 72]. Also industry has shown great interest in morphing winglets due to the potential increase in structural and/or aerodynamic efficiency. Boeing for example has filed two patents in 2010 and 2014, related to morphing winglets [49, 71]. In addition the EU project Novel Air Vehicle Configurations: From Fluttering Wings to Morphing Flight (NOVEMOR) resulted in a paper from DLR on morphing winglets [11]. Also the CleanSky 2 project from the EU has set goals to research morphing winglets. However, the majority of these efforts focuses on 2D morphing winglets (including the work done by E. Gillebaart and R. De Breuker), which need to be extended to 3D for practical applications. In addition, only a few of these papers involve some sort of optimization [15, 16, 74]. Rather than optimizing the mechanism or device that allows for the morphing of a winglet, these papers focus on maximizing range and endurance or minimizing the drag of a wing with a morphing winglet.

The state-of-the-art of topology optimization as well as its application in the aerospace industry will be given in Section 1.1. Section 1.2 will elaborate on the research gap identified and how this research will fill the gap. Based on the gap the research objective for this thesis is formulated and stated in Section 1.3. Finally, Section 1.4 will provide the outline for this thesis.

1.1. STATE-OF-THE-ART

In this section a brief overview is given of topology optimization and how this has been used to design morphing aircraft structures. First a few important branches within topology optimization are discussed, including the continuum and the ground-structure approach, gradient and non-gradient methods, as well as some considerations regarding mechanism design. Then an overview is given of the various morphing aircraft structures that have been designed using topology optimization.

1.1.1. TOPOLOGY OPTIMIZATION

As mentioned earlier, topology optimization can be defined as the process of optimizing both the material layout and the connectivity inside a design domain [56], usually subjected to one or more constraints. Solving topology optimization problems can be done by discretizing the design domain into many finite elements. Then the density of each element, i.e. the material distribution, is determined such that the objective function is minimized while satisfying the given constraints. The two different ways of discretizing the design domain are known as the continuum and the ground-structure approach, which will be discussed in the next paragraph. Both approaches yield an optimization problem that can be solved with gradient or non-gradient based methods. The different methods are covered here as well. Finally, mechanism design has implications for the problem formulation. The different approaches to design mechanisms are discussed in the last paragraph.

CONTINUUM AND GROUND-STRUCTURE APPROACH

The two different types of topology optimization are the continuum approach and the ground-structure approach. The continuum approach is the most used both in academia and industry. The design space in this approach is completely filled with material, allowing for more flexibility in the design. Figure 1.1 shows the design space (top) and the optimized design (bottom) for the Messerschmitt-Bölkow-Blohm (MBB) beam based on the continuum approach.

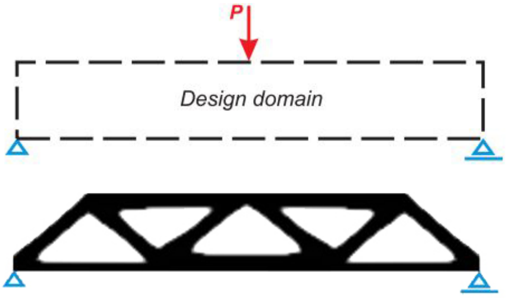

Figure 1.1: Illustration of the MBB beam based on the continuum approach [38]

When solving the continuum approach with gradient based methods like the density methods, the optimization process requires an additional step involving regularization techniques to prevent numerical issues such as checker-boarding and mesh dependency. By checker-boarding is meant the formation of solid-void elements in a checkerboard pattern. Mesh dependency means that the topologies will change with different discretization sizes, while the problem formulation remains unchanged [12]. The two primary regularization methods are filtering and constraint techniques. Filtering techniques modify the density variables or the sensitivities directly, while the constraint techniques add local or global constraints to the optimization problem. An overview of different density and sensitivity filtering techniques can be found in [12] and [55]. Density filters work by modifying the element density based on a function involving the surrounding density elements. The sensitivity filter calculates the sensitivities based on a weighted average of surrounding sensitivities [55]. The original sensitivity filter was presented by Sigmund in 1997 [54]. An overview constraint techniques can be found in [12]. As a consequence of the filtering techniques (both density and sensitivity) grey material will be present between the solid and void/empty regions. To remove the grey regions, several schemes have been developed including morphology-based operators [55, 70] and projections of filtered densities via the relaxed Heaviside function [25, 34].

The second approach is the ground-structure approach. The design space is not completely filled with material, but consists of nodes interconnected via truss members. Figure 1.2 gives an example an inverter mechanism based on the ground-structure approach. The optimizer selects which combination of truss members yields the optimal solution. The final design consists then only of a few truss members.

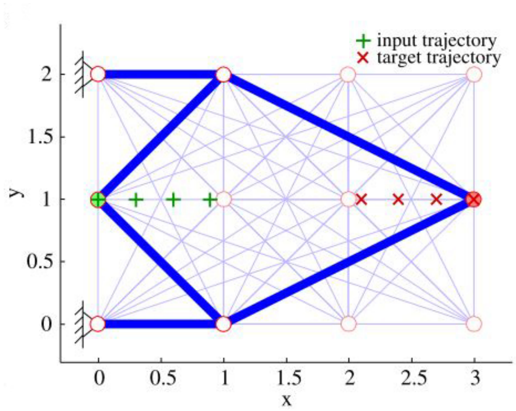

Figure 1.2: Illustration of the inverter mechanism based on the ground-structure approach [13]

The ground-structure approach is very suitable for optimizing truss structures. It has also several advantages compared to the continuum approach. One is the limited post processing time, i.e. the ease of interpretation. Especially when designing mechanisms, the continuum approach might give difficulties in the post processing step when thin regions are to be removed or function as a hinge. In addition, the density approach based on the ground-structure does not require any regularization techniques. Kawamoto has done research on how the ground structure approach can be used to design mechanisms. In his tool also the buckling is included as a constraint [30].

GRADIENT AND NON-GRADIENT OPTIMIZATION METHODS

Two different classes of gradient based methods include the density methods and the boundary variation methods. Within the non-gradient based methods one distinguishes between the hard-kill methods and bio-inspired cellular division methods. All four methods will be discussed here.

The first density-based method was proposed by Bendsøe in 1989 [3]. Since then several other methods have been developed, all with the same working principle. These methods have in common that they make use of the density variables to steer the optimizer towards a 0/1 solution. The most well known density method is the SIMP approach as proposed 1989 [3] and can be categorized as a material interpolation scheme. This implicit method penalizes intermediate densities to promote a 0/1 solution. Other approaches include the RAMP, Hashin-Shtrikman, Reuss-Voigt and quadratic penalization. Why penalization is required for gradient based optimization methods and how these different penalization schemes work, will be discussed in more detail in Chapter 3.

Boundary variation methods are more recently developed and originate from shape optimization techniques. In boundary variation methods implicit functions define the structural boundaries, in contrast to the density methods where explicit parametrization of the design space is used [12]. The two most used boundary variation methods include the level set method and the phase-field method. These methods however are not suitable for the ground-structure approach.

The first class of non-gradient based methods is the class of the hard-kill methods. These methods do not involve any sensitivities [12]. Hard-kill methods work by gradual addition and removal of finite amount of material from the design space. The addition and removal of material is based on heuristic rules. The most well known hard-kill method is the Evolutionary Structural Optimization (ESO) method. This method works with removal of material only.

The last class is the so-called bio-inspired cellular division method, proposed by Kobayashi in 2010 [37]. This method is able to generate both discrete and continuum structures and is inspired on the cellular division process. It develops the topology in stages based on a sequence of tasks. The set of rules that define the tasks are called the map-L system. When using a genetic algorithm (GA) for this method, the design variables become the set of rules.

MECHANISM DESIGN

Two common types of mechanisms are the articulated mechanisms and the compliant mechanisms. Articulated mechanisms consist of several linkages connected via (hinged) joints. These mechanisms get their mobility via their free joints. While compliant mechanisms gain their mobility via the elasticity of its components [30]. An example of both types of mechanisms can be found in Figure 1.3.

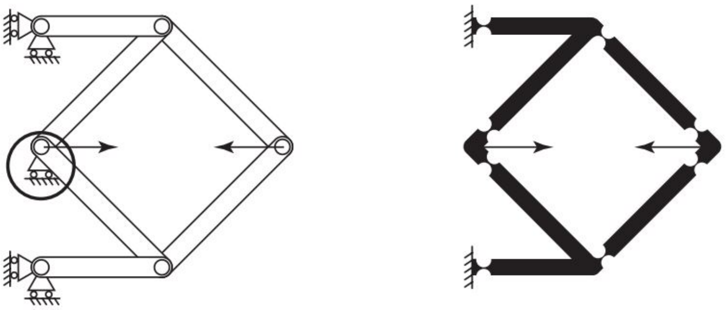

Figure 1.3: Illustration of articulated mechanism (left) and compliant mechanism (right) [30]

What is important in mechanism design (both for articulated as well as complaint mechanisms) is the trajectory of one or more nodes during the deformation, i.e. the kinematics from the mechanism. In general for mechanisms it is required that one or more nodes follow a certain trajectory. One way to incorporate the trajectory is by formulating an objective function which minimizes the least squares error between the intended trajectory and the actual trajectory of the mechanism [45].

A different way would be to include an additional constraint which specifies the allowed deviations from the intended trajectory. This approach does not optimize the mechanism for the trajectory. In this formulation the nodes follow the intended trajectory sufficiently well (as dictated by the constraint), and could then be optimized for something else instead, like minimum compliance [35]. Kawamoto's research was focused on articulated mechanisms [30], where a least squares error was formulated as the objective function. The objective results in structures that are able to follow the intended trajectory, but that does not necessarily result in mechanisms. It could very well be that the truss members are strained to be able to follow the intended trajectory. Therefore an additional constraint was included to regulate the number of degrees of freedom. Since truss structures were considered the Maxwell's rule could be adopted, which for the 2D discrete formulation looks like [33]:

$$d_m = 2n - b - r \tag{1.1}$$

In this equation d_m represents the number of DOF, n represents the number of nodes in the structure, b represents the number of independent non-redundant bars (i.e. no overlapping bars), and r represents the number of reaction forces. This rule can be used since articulated mechanisms get their mobility via one or more DOFs. The parameter b can be obtained by determining the rank of the equilibrium matrix. Kawamoto also explains how this rule can be used in the relaxed formulation [32].

1.1.2. TOPOLOGY OPTIMIZATION AND MORPHING AIRCRAFT STRUCTURES

This section focuses on the research done in the field of topology optimization and morphing aircraft structures. Various morphing structures are covered, including the leading edge, trailing edge, wing, skin and winglet. Since no research has been done on the design of morphing winglets via topology optimization, the last section is focused on research done on morphing winglets in general.

MORPHING LEADING EDGE

In 2003 Lu and Kota [39] have published a paper on the design of a compliant mechanism for a morphing leading edge. They used the ground-structure approach to parametrize the design space. Their objective function involves the Least Square Error (LSE) measure as well as a modified Fourier Transform to rank the design shapes. A GA algorithm is used to solve the optimization problem. In 2005 they published a different paper [40], which could be seen as an improvement of their previous work. In this paper a modified ground-structure approach is used, by them described as the load-path method. This method analyses a limited number of distinct load paths, rather than every truss element separately. By combining different load paths, the optimal solution is sought. This new approach should overcome the issues of disconnected structures. In addition, this approach does not require an a-priori specified mesh. In their paper they find the desired shapes effectively with their new method. The load path method is further improved from 2007 and onwards [50, 51]. This method also prevented intersecting members to guarantee manufacturability.

Also the faculty of aerospace engineering of Delft University of Technology has done research in this field. In this research a design method, using topology optimization, was presented for an actuation system of a morphing leading edge [66]. This work was done as part of the Leading Edge Actuation Topology Design and Demonstration (LeaTop) project. The Solid Isotropic Material with Penalization (SIMP) interpolation scheme was used. One year later additional research was done by the faculty and a paper on the design and demonstration of the leading edge actuation system was presented [41]. Recently, in 2015, research was presented on the experimental evaluation of the morphing leading edge. They demonstrated a rotation of the leading edge of at least 5 degrees. An extensive outline of the experimental set-up used can be found in their paper [61].

Other work has been done by the Northwestern Polytechnical University [73]. In their research, topology optimization was used to design a compliant morphing leading edge involving composite materials. The objective function was to minimize the LSE of the actual shape and the target shape. The SIMP method was adopted to penalize intermediate densities, while the sensitivities were calculated using the adjoint method. The optimized solution was also experimentally tested.

Finally, Kintscher from DLR has done research on morphing leading edges as well [36]. They have developed several leading edge devices for morphing. Experimental testing was done on a full-scale leading edge. A compliant skin has been proposed, and the internal structure is designed via topology optimization. This structure is used to morph the leading edge.

MORPHING TRAILING EDGE

Amongst others, Friswell and Baker are two well-known researchers for their work in morphing aircraft structures. They have published two papers [1, 19] on the optimization of morphing trailing edges. The paper from 2008 focused on the optimization of hierarchical structures. Their model has been applied to two examples, being the optimization of structure's anisotropy and the optimization of truss and skin elements of compliant trailing edge mechanism. Their optimization process involves both gradient based optimization algorithms and GA algorithms. In their second work they investigated truss structures for a variable camber trailing edge. In the first step a statically and kinematically stable structure is proposed, where in the second step truss members are replaced by actuators. To reduce the complexity of the design, Baker and Friswell propose for further research to consider compliant members rather than articulated truss members.

In 2008 another paper [53] was published on the design of a compliant mechanism for a morphing trailing edge. The proposed tool was written in MATLAB, which called the commercial finite element software package ANSYS to conduct the finite element analysis (FEA). The topology optimization was based on the ground-structure approach to design the compliant mechanism. Due to the large deflections geometric non-linearity was accounted for as well. Although the GA algorithm used could be able to optimize the topology and dimension simultaneously, a second optimization run (direct search) was used to optimize the dimensions.

Also Delft University of Technology has done research in this field. Vos et al. [69] used topology optimization techniques to optimize a pressure adaptive honeycomb structure for a morphing flap. The trailing edge was designed to morph and act as a flap. In further research the computational efficiency should be improved to reduce the time to find the best topology.

MORPHING LEADING AND TRAILING EDGE

Trease and Kota [67] have developed a tool to optimize a compliant mechanism with embedded actuators and sensors. The tool optimizes simultaneously the structural topology as well as the location of the actuators and sensors for maximum efficiency and adaptive performance. The efficiency is specified as the work done by the output node(s) divided by the work done by the input node(s). Their research is also compatible with one or more input and output nodes. They classify the problems as single-input-single-output (SISO) problems, multiple-input-single-output (MISO), and multiple-input-multiple-output (MIMO) problems. Their work is based on the general ground-structure approach and was applied to morph an airfoil. Further improvements would be to include non-linear FEA and the load-path approach, as previously proposed in 2005 [40].

In 2004 Maute and Allen presented a paper on 3D aeroelastic structures [43]. In their work they consider fluid-structure interaction as well. Central in the work is a Sequential Augmented Lagrangian method for solving the optimization problem. The analytical adjoint method is used to determine the sensitivities. In 2006 Maute and Reich [44] came up with an integrated design tool, where both an aerodynamic and structural module are combined. Their approach is compared to the traditional two step process, where first the aerodynamic shape is optimized and then the structure that could maintain the shape. The problem is solved via the sequential convex programming (SCP) algorithm method of moving asymptotes (MMA). The sensitivities required for MMA were calculated using the adjoint method and the SIMP material interpolation scheme was adopted. It was found that the design performed better compared to the two step process, but the computational time increased by a factor ten.

MORPHING WINGS

Topology optimization has also been applied to design complete wings. Eves et al. for example have published a paper in 2009 [14] on the wing design of non-conventional aircraft. Topology optimization turned out to be a very effective tool to use in the design for unconventional aircraft, where little knowledge in advance is available for the optimal structure. In their research they optimized the wing of a blended wing body (BWB) unmanned air vehicle (UAV), using the SIMP material interpolation scheme. Also, special attention was given to wing skin buckling and two different approaches were suggested to incorporate this into the design. They suggested to include the aerodynamic performance in further research.

Topology optimization has also been applied to design an in-plane morphing wing [27]. In this paper the ground-structure approach is adopted. The optimization problem is relaxed and solved by using the globally convergent method of moving asymptotes (GCMMA) with adjoint sensitivities. In addition to the topology, also the location and the relative force intensities of distributed actuators are optimized. In addition, both single and multi-objective formulations were used in the optimizations. In 2008 [28] the authors published a second paper, with the aim of improving and extending their previous work. In the first paper the wing possessed only two stable configurations. In their second paper multiple configurations of the wing were possible. For further research the authors propose to include out-of-plane deflection of the wing as well as aeroelastic effects.

Sleesongsom, Bureerat and Tai published a paper on the design of a morphing wing in 2013 [59]. Their work is based on the ground-structure approach, split up into two different strategies. The first strategy uses topology and sizing optimization for the design variables, the second strategy includes the nodal locations as well. They used a multi-objective formulation, to minimize the mass, prevent aeroelastic effects such as divergence and flutter, as well as stress limits. The optimization problem was solved with a multi-objective population-based incremental learning (MOPBIL) algorithm. Both strategies give Pareto fronts with unconventional results.

MORPHING SKINS

The majority of the research on morphing structures is focused on the internal structure. This structure is designed to morph and should be able to carry the external loads. As a consequence of these morphing motions, the requirements on the morphing skin are challenging. Not only does the skin experience very large in-plane deformations, usually there are also requirements on the out-of-plane behavior of the skin. As a result, often regular materials are not able to cope with these requirements and man-made materials have to be designed. The importance of morphing skins has also being stressed in the paper of Friswell et al. that focused on the design of morphing trailing edges [18].

Work that deals with the design of morphing skins is performed by Joo, Reich, and Westfall [29, 46]. Their work focused on the development of an engineered composite skin for morphing aircraft applications by a two-step process. The first step determines the macroscopic bulk properties across the three layer skin, while the second step optimizes the micro-structure of the skin. The authors mentioned that the manufacturing process would be easier for monolithic skins with equivalent properties.

Thuwis et al. [65] have also published a paper on the optimization of skins. This work proposes a tool to optimize a variable-stiffness composite skin suitable for morphing applications. The variable-stiffness is achieved by changing the skin thickness and the spatial fibre angle. A two-dimensional aero-solvo-elastic framework has been developed. The skin optimization is performed by a gradient-based algorithm, making use of adjoint sensitivities. The authors suggest to include the aerodynamic behavior in the early design stage due to its large effect on the skin.

MORPHING WINGLETS

This section is concerned with the research field of morphing wingtips/winglets. Many different papers have been published about research in this field. Important papers will be discussed here, starting with those from P. Bourdin, A. Gatto, and M.I. Friswell.

Over the years Bourdin, Gatto, and Friswell have published several papers on morphing winglets. They proposed variable cant angle winglets for morphing aircraft control [5, 7]. These winglets are proposed as an alternative to the conventional control surfaces such as the aileron and rudder. Both experimental and numerical tests were performed and it was found that these winglets result in a highly coupled flight control system. In addition, they found that not the complete flight envelope could be realized with only one morphing winglet per wing, additional control surfaces were necessary to support the manoeuvres. A different suggestion was made to split the winglets, such that on each wingtip two winglets are present. The suggestion of articulated split wingtips was further researched and two paper were published [6, 8]. Again numerical and experimental methods were used to analyze the model. It was found that these split wingtips were capable of providing the required control moments. In fact multiple different wingtip configurations existed for a particular control moment, meaning that a second objective (such as drag) could be minimize. The proposed model worked well at moderate and high lift coefficients, making it suitable for low speed aircraft. In Figure 1.4 the prototype used in the wind tunnel tests of Friswell can be found.

Figure 1.4: Picture of the model with articulated split wingtips used in the wind tunnel tests [8]

Friswell has also contributed to other research entitled "Morphing Winglets for Aircraft Multi-phase Improvement" [68]. This paper focuses on the hierarchical methodology towards the final morphing application (MORPHLET). The paper starts with the selection process of smart materials, followed by an optimization of non-planar wing schedules. This optimization tool includes an aerodynamic module, wing weight module, and a Breguet range module. The optimization is performed by a GA algorithm.

In addition, DLR presented their work on the 4th EASN Association International Workshop on Flight Physics & Aircraft Design Conference [11] in Germany. The research, as part of the NOVEMOR project, focused on a droop-nose morphing wingtip. In the design tool first the composite skin was optimized, followed by the internal compliant structure. The full-scale wind tunnel model demonstrated the working principle of the morphing wingtip.

Three other researchers (J. Wittmann, H. Baier, and M. Hornung) have also presented their work [72] on the German Aerospace Congress in 2010. Friswell has done research with them as well, but that was focused on an hierarchical approach for the conceptual design of morphing devices. The research done by Wittmann, Baier, and Hornung was focused on the mission performance optimization by making use of morphing wing tip devices. More on this work can be found in reference [72].

Also Gomes, Falcão and Suleman have done research in this field. Their first work dates back to 2009 [22]. In this work a multidisciplinary optimization (MDO) strategy is proposed to design multi stable composite plate configurations for morphing wingtips. One year later additional work has been presented on MDO of a morphing wingtip [15]. In this work the wingtip is able to rotate over the vertical axis (toe angle) and the aircraft's longitudinal axis (cant angle). Their work focuses on optimizing a performance metric (such as lift, drag, lift-to-drag-ratio, etc.), subjected to stress an displacement constraints. The structural analysis was done in ANSYS and the computational fluid dynamics in CFX. In 2011 additional work was presented [16]. This work included experimental tests of the morphing wingtip. A major improvement of 20% reduction in ground roll was found. Also, a 2% increase in fuel efficiency in cruise was realized. Also in 2013, research concerned with morphing winglets was presented [23]. This work involved significant experimental work and a detailed prototype was manufactured. Two separate servos were used to change the cant angle and the toe angle respectively. The experimental work included tip displacement measurements for different cant and toe angles.

Other work has been done by the Georgia Institute of Technology [52, 60]. Their first work dates back to 2001, focusing on active multiple winglets to improve the performance of UAVs. By applying numerous active winglets it was found that these could replace ailerons. In addition, these winglets provide gust alleviation, which improved the handling quality as well as the sensor performance. Two different methods were used to predict the performance of the winglets. The first method adopted a panel method and CAD geometry for the analysis. The second method used the characteristics of the baseline model combined with results from winglets from a generic wing. It was concluded that up to 40% increase in range and endurance could be achieved. Also, due to the active winglets a higher lift coefficient was found for cruise conditions, which could be used to increase the payload. Their second paper was in collaboration with Star Technology and Research, Inc. on the performance analysis of a wing with multiple winglets. In this work a NACA 0012 airfoil was used with morphing winglets and tested in the wind tunnel. A reduction of induced drag and an increase in lift-over-drag (L/D) of 15-50% was experimentally found.

1.2. BEYOND STATE-OF-THE-ART

In this section the research gap derived from the state-of-the-art will be addressed. In addition, the relevance will be covered as well. Hence this section covers the progress beyond state-of-the art, which forms the basis for the research goals mentioned in the next section. From the previous section two things become apparent. To the best of the author's knowledge, the following statements can be made:

1. Topology optimization has not been applied to design the mechanism for morphing winglets
2. 3D ground-structure based topology optimization has not been used to design mechanisms in the aerospace industry

Topology optimization techniques are common in the design of morphing aircraft structures. However, the research done was mainly focused on 2D. In addition, it was observed that topology optimization has not yet been applied to design the mechanism of morphing winglets. Optimizations have been performed where morphing winglets were included, but the objective was to maximize range and endurance or to minimize drag. Here the ability of the winglet to deflect was used to increase the range, rather than optimizing the material distribution to design a morphing winglet.

It has been observed that topology optimization had not been applied to design a mechanism for morphing winglets. This is interesting given the great interest shown in the design of morphing winglets and the use of topology optimization for morphing aircraft structures. Many project including those from the EU (NOVEMOR and Clean Sky) and Airbus (MORPHLET) have shown interest in morphing winglets. Given the gap and its relevance it has been decided to focus the research on the design of morphing winglets using topology optimization. As mentioned earlier, most research was limited to 2D, whereas 3D is required for practical applications. Therefore, the research will also focus on 3D morphing winglets using topology optimization . Since this research area is very broad, a specific research objective and corresponding goals are defined in the next section.

1.3. RESEARCH OBJECTIVE AND RESEARCH GOALS

In the previous section it was mentioned that only limited research has been done on 3D topology optimization. It was also found that no research has been done on the design of morphing winglets using topology optimization techniques. Given this research gap and the significant interest the industry has shown in morphing winglets, it would be interesting to explore the field of topology optimization to design a 3D morphing winglet. In this section the specific objective and goals are formulated, which will be researched for this thesis.

1.3.1. RESEARCH OBJECTIVE

As mentioned in Section 1.1.1 there exist two ways of discretizing the design space. The first approach is the continuum approach, the second is the discrete or ground-structure approach [30]. Advantages of the ground-structure approach include the limited post processing, the absence of additional filtering techniques, and the limited problem size due to the less dense design space compared to the continuum approach [30]. Based on these advantages it has been decided to develop a tool to design 3D morphing winglets using the ground-structure topology optimization approach based on the previous work done by E. Gillebaart and R. De Breuker [21]. The research objective can be more formally stated as:

"Developing a software tool to design a mechanism for morphing winglets, using ground-structure based topology optimization, by improving, extending, and expanding the previous 2D inhouse tool."

1.3.2. RESEARCH GOALS

The research objective can be split into three sub-goals, i.e. improving, extending and expanding of the previous tool. Improving the tool can be achieved by improving the robustness of the tool, the computational time of the tool and the separation of the design vector. The tool is not always stable and could converge towards non-feasible solutions. In addition, the computational efficiency of the previous implementation could be improved, which is highly favorable once the tool will be expanded to 3D. Also, in some design cases rather poor separation was observed, where several elements had densities unequal to 0 or 1. These results could not be interpreted and therefore not used. In addition, the tool can be extended in terms of its capabilities. Buckling criteria can be included to guarantee stability of the mechanism. Also, the previous tool is only compatible with one input node and one output node. Multiple input and output nodes increases the flexibility of the tool. Finally, as mentioned before, the tool designs 2D mechanisms. Once the tool is improved and extended in terms of capabilities, the tool will be expanded to 3D. These goals can be summarized as follows.

1. Improve previous tool
    (a) Increase robustness
    (b) Reduce computational time
    (c) Increase separation
2. Extend previous tool
    (a) Include multiple input nodes
    (b) Include multiple output nodes
    (c) Include buckling

3. Expand previous tool
    (a) Expand to 3D

1.4. OUTLINE

To meet the research goals defined in the previous section, a tool has been developed. The tool is schematically represented in Figure 1.5. The tool consists of four steps, the input, mechanism design, mechanism sizing, and output step. First the steps are briefly covered, then the structure of the thesis will be explained. The structure of the thesis can be better understood by going through the steps of the tool first.

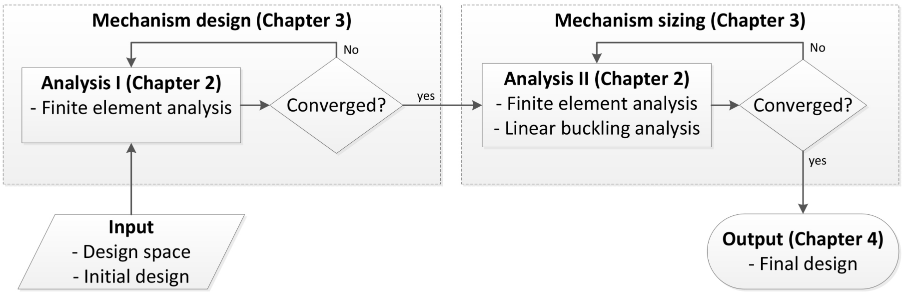

Figure 1.5: Flowchart of the design procedure

In the input step the design space is defined. This means that the size of the design space has to be chosen, where the nodes are located, how many elements are included, how the mechanism is supported and which nodes are used for actuation (input nodes) of which nodes are traced (output nodes). Also, the initial design vector (the cross-sectional areas of the truss members) has to be chosen.

In the second step the mechanism is designed. This is an optimization where the optimizer determines which elements are needed to be able to follow the trajectory. The objective and constraints used, will be discussed in Chapter 3. The (initial) design vector/geometry is evaluated in the analysis section. How the structure deforms, what the internal forces are, what the reaction forces are, etc. are determined here. Then the optimizer determines how the design vector/geometry should change to minimize the objective while satisfying the constraints. The output is a converged design vector which tells which elements are needed for the mechanism.

The next step then removes all elements except for those that are needed according to the previous step. Then a second optimization is performed to minimize the weight of the mechanism while satisfying several failure constraints. This step finds the minimum weight of the mechanism, while preventing failure.

In the final step, the output step, the sizing optimization is converged a final geometry will result. This mechanism is able to follow the given trajectories, will have minimum weight and will not fail under the given loading.

In Chapter 2 will cover the different analysis tools from both optimizations. The finite element tool and the linear buckling analysis will be covered. The tools determine its structural behavior, which functions as input for the objective functions and constraints. Chapter 3 elaborates on the optimization process. It will cover which optimizer is used, what strategy is used to design morphing winglets, and covers in detail the objective, constraints, and their sensitivities of both the mechanism design as well as the sizing optimization. Then Chapter 4 contains the results obtained from the optimizations. Both a 2D winglet and a 3D winglet design case has been included. Finally, Chapter 5 contains the conclusions and recommendations for future research.

2

ANALYSIS

This chapter describes the analysis tools used in the optimization procedure to design the morphing winglet. Two different analyses can be identified, the finite element analysis (Section 2.1) and the linear buckling analysis (Section 2.2). The FEA calculates the nodal displacements that result in equilibrium. The FEA also calculates the elemental strains and reaction forces that result from this equilibrium. In the linear buckling analysis, an eigenvalue analysis is performed to calculate the buckling load factors. When load factors are found between 0 and 1, the structure is unable to withstand the applied loading and will buckle. Finally, Section 2.3 covers how the output from the analysis tools are post-processed. Here the structural behavior is compared to predefined limits to assess how the structure performs.

2.1. FINITE ELEMENT ANALYSIS

As discussed previously, the FEA is used in the optimization procedure. The module solves for the displacement vector $\boldsymbol{u}$ which satisfies equilibrium. These equilibrium equations are derived from the total potential energy (TPE). The tool calculates the structural deformation as a result of prescribed displacements and/or applied loading. The tool also calculates the elemental strains as well as the nodal reaction forces. These structural responses are used as in input for the optimizer. Objective functions and constraint functions are formulated based on these outputs, which will be explained in the next chapter.

The developed finite element tool consists of two steps. In the first step the structure is only actuated, i.e. only the prescribed displacements are enforced. Then, the corresponding displacement vector for equilibrium is calculated. This displacement field corresponds to the movement of the nodes when no loading is applied. In the second step the loading is applied and the deformations due to the loading are obtained. In this finite element tool it is assumed that the large displacements and rotations result from the actuation step. The deformations of the elements due to the loading are assumed to be small. As a result, in the first step it is assumed that the stiffness matrix is a function of the displacements. This requires an iterative procedure to calculate the displacement vector $\boldsymbol{u}^{(NL)}$. Here the superscript (NL) refers to the non-linear/iterative solver used in the first step of the finite element analysis. Once that equilibrium is found, the loading is applied. Here it is assumed that the stiffness matrix remains constant and equal to the converged stiffness matrix obtained in the first step. The displacement vector obtained in second (linear) step is denoted as $\boldsymbol{u}^{(L)}$. The finite element tool is schematically represented in Figure 2.1.

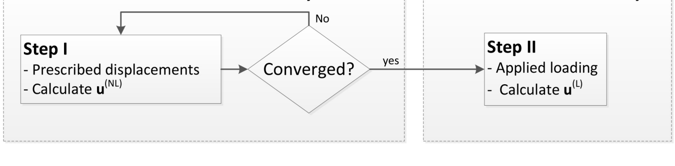

Figure 2.1: Flowchart of the finite element analysis

The decoupling of the prescribed displacements and applied loading is done to be able to calculate the displacements only caused by the loading. These displacements, or deviations from the equilibrium state due to loading, are used in the objective function for the mechanism design, covered in the next chapter.

First the TPE will be formulated, followed by how the equilibrium equations are obtained from it. Then, the strain measure used will be covered, followed by which iterative algorithm is used to solve the equilibrium equations (in step I). The displacement vector obtained in this step is denoted as $\boldsymbol{u}^{(NL)}$. The method used here is based on the PhD work of Kawamoto [30]. Then briefly the linear step is covered to calculate $\boldsymbol{u}^{(L)}$. In addition, the FEA is able to solve the equilibrium equations both for 2D as well as 3D structures, hence the changes required to extend the FEA from 2D to 3D will be covered, followed by the verification for both 2D and 3D.

2.1.1. DESCRIPTION

The TPE (Π) is defined as the sum of the internal strain energy (U) and the work done by the external conservative forces (V).

$$\Pi = U + V \tag{2.1}$$

The structures considered here solely consist of truss members, which can only carry axial loading. As a consequence the strain energy of the structure can be written as the sum of the elemental axial strain energies. In addition, the forces are assumed to be constant. This allows the external work to be written as a constant external force vector times the displacement vector. Rewriting the TPE gives:

$$\Pi(\boldsymbol{A},\boldsymbol{x},\boldsymbol{u}) = \frac{1}{2}\sum_{i=1}^{N_e} A_i E_i l_i(\boldsymbol{x})\epsilon_i(\boldsymbol{u},\boldsymbol{x})^2 - \boldsymbol{p}^T\boldsymbol{u} \tag{2.2}$$

Here $\boldsymbol{A} \in \mathbb{R}^{N_e}$ represents the vector containing the cross-sectional areas of all truss members, $\boldsymbol{x} \in \mathbb{R}^{2N_n}$ is the vector containing all nodal locations, $\boldsymbol{u}$ is the nodal displacement vector, and $\boldsymbol{p}$ is the nodal force vector. Furthermore, N_e represents the total number of elements (truss members) of the mechanism, N_n is the total number of nodes of the structure, and N_d is the total number of free degree of freedoms (DOF). This number is (in 2D) equal to twice the number of nodes minus the fixed DOF. The fixed DOF are the ones constrained by the supports. Finally, A_i represents the cross-sectional area, E_i the Young's modulus, l_i the undeformed length, and ϵ_i the strain of the i^{th} element.

Minimizing the TPE will yield equilibrium. Therefore Equation 2.3 can be solved to find the displacement vector that yields equilibrium. However, solving Equation 2.3 will yield stationary values for the TPE, which could also maximize the TPE. Therefore Equation 2.4 has to be satisfied as well to guarantee that the solution found minimizes the TPE.

$$\nabla_{\boldsymbol{u}}\Pi(\boldsymbol{A},\boldsymbol{x},\boldsymbol{u}) = 0 \tag{2.3}$$

$$\nabla^2_{\boldsymbol{uu}}\Pi(\boldsymbol{A},\boldsymbol{x},\boldsymbol{u}) \geq 0 \tag{2.4}$$

STRAIN MEASURE

As was already indicated in Equation 2.2, the strain is a function of both the nodal location as well as the nodal displacement. The dependence on the displacement vector will be non-linear, which is required to model the large displacements and rotations that occur during actuation. Even though the displacements and rotations are large, the strains are assumed to be small and the material is assumed to behave linear elastic. The large nodal displacements are a result of the kinematics of the mechanism, the deformation of the members of the structure will be small. This would mean that the functionality for mechanisms is not changed when the members were replaced by rigid elements. A suitable strain measure for modelling large displacements and rotations, while the strains remain small, is the Green-Lagrange (GL) strain measure. This strain measure is therefore used. Consider a single element, which is under uni-axial loading, then the GL strain can be written as:

$$\epsilon = \frac{\hat{l}^2 - l^2}{2l^2} \tag{2.5}$$

Here $\hat{l}$ is the deformed length of the element. In 2D the strain can also be written as:

$$\epsilon = \frac{\partial \boldsymbol{u}_1}{\partial x} + \frac{1}{2}\left[\left(\frac{\partial \boldsymbol{u}_1}{\partial x}\right)^2 + \left(\frac{\partial \boldsymbol{u}_2}{\partial x}\right)^2\right] \tag{2.6}$$

In Equation 2.6 the partial derivatives are in local coordinates. These partial derivatives can be expressed in terms of the global displacement coordinates and the corresponding rotations, given by Equation 2.7.

$$\begin{aligned}
\frac{\partial \boldsymbol{u}_1}{\partial x} &= \frac{1}{l}\boldsymbol{\gamma}\boldsymbol{u} \\
\frac{\partial \boldsymbol{u}_1}{\partial x} &= \frac{1}{l}\boldsymbol{\delta}\boldsymbol{u} \\
\boldsymbol{\gamma} &= [-cos(\alpha) \quad -sin(\alpha) \quad cos(\alpha) \quad sin(\alpha)] \\
\boldsymbol{\delta} &= [sin(\alpha) \quad -cos(\alpha) \quad -sin(\alpha) \quad cos(\alpha)]
\end{aligned} \tag{2.7}$$

Substituting Equation 2.7 into Equation 2.6 gives:

$$\epsilon = \frac{1}{l}\boldsymbol{\gamma}\boldsymbol{u} + \frac{1}{2l^2}\left[(\boldsymbol{\gamma}\boldsymbol{u})^2 + (\boldsymbol{\delta}\boldsymbol{u})^2\right] \tag{2.8}$$

Carrying out the multiplication gives the following for the second term:

$$(\boldsymbol{\gamma}\boldsymbol{u})^2 + (\boldsymbol{\delta}\boldsymbol{u})^2 = \begin{bmatrix} 1 & 0 & -1 & 0 \\ 0 & 1 & 0 & -1 \\ -1 & 0 & 1 & 0 \\ 0 & -1 & 0 & 1 \end{bmatrix} \tag{2.9}$$

Calling this matrix $\boldsymbol{B}$ allows one to rewrite Equation 2.8 as a function of this matrix. Also the matrices $\hat{\boldsymbol{B}}$ and $\tilde{\boldsymbol{B}}$ are introduced. Matrix $\hat{\boldsymbol{B}}$ is defined as matrix $\boldsymbol{B}$ after removing the rows corresponding to the fixed DOF. Matrix $\tilde{\boldsymbol{B}}$ is defined as matrix $\boldsymbol{B}$ after removing both the rows and columns equal to the fixed DOF. Then for the single element the strain can be written as:

$$\epsilon = \frac{1}{l^2}\hat{\boldsymbol{B}}\boldsymbol{x}\boldsymbol{u} + \frac{1}{2l^2}\boldsymbol{u}^T\tilde{\boldsymbol{B}}\boldsymbol{u} \tag{2.10}$$

or

$$\epsilon = \frac{1}{l^2}\boldsymbol{b}^T\boldsymbol{u} + \frac{1}{2l^2}\boldsymbol{u}^T\tilde{\boldsymbol{B}}\boldsymbol{u} \tag{2.11}$$

Here $\boldsymbol{b}$ divided by l will yield the direction cosines of the element. Translating this concept to a mechanism consisting of several elements, will result in a strain for the i$^{\text{th}}$ element given by:

$$\epsilon_i = \frac{1}{l_i^2}\hat{\boldsymbol{B}}_i\boldsymbol{x}\boldsymbol{u} + \frac{1}{2l_i^2}\boldsymbol{u}^T\tilde{\boldsymbol{B}}_i\boldsymbol{u} \tag{2.12}$$

Where $\hat{\boldsymbol{B}}_i \in \mathbb{R}^{d\times 2N_n}$ is equal to $\boldsymbol{B}$ with the rows corresponding to the fixed DOF removed. It can also be written as:

$$\epsilon_i = \frac{1}{l_i^2}\boldsymbol{b}_i^T\boldsymbol{u} + \frac{1}{2l_i^2}\boldsymbol{u}^T\tilde{\boldsymbol{B}}_i\boldsymbol{u} \tag{2.13}$$

Note that $\boldsymbol{b}_i$ and $\tilde{\boldsymbol{B}}_i$ are determined by the connectivity of the element. Here $\boldsymbol{b}_i \in \mathbb{R}^{N_d}$ is equal to $\hat{\boldsymbol{B}}_i\boldsymbol{x}$ and $\tilde{\boldsymbol{B}}_i \in \mathbb{R}^{N_d\times N_d}$ is equal to $\boldsymbol{B}_i$ with the rows and columns corresponding to the fixed DOF removed. Also note that the linear strain measure is recovered if the non-linear contribution is neglected. Finally, due to the non-linear GL strain measure, solving the equilibrium equations has to be done iteratively. This will explained in the next section.

ITERATIVE ROOT FINDING

Due to the non-linear strain formulation, the minimization of the TPE will has to be done iteratively. Over the years many different iterative algorithms have been developed for iterative root finding. The standard algorithm looks as follows:

```
$\boldsymbol{x} = \boldsymbol{x}_0$
$k = 0$
repeat
        find $\boldsymbol{h}$                      (2.14)
        $\boldsymbol{x} = \boldsymbol{x} + \alpha \boldsymbol{h}$
        $k = k + 1$
until stop
```

Here $\boldsymbol{x}$ is updated iteratively until a certain convergence criteria is met. The variable $\boldsymbol{h}$ is the direction of descent and a is the step size. A popular algorithm is the steepest descent approach, where the direction is calculated from:

$$\boldsymbol{h} = -\boldsymbol{F}'(\boldsymbol{x}) \tag{2.15}$$

The algorithm is robust, even when the initial guess $\boldsymbol{x}_0$ lies far from the converged solution. The convergence, however, is rather poor close to the optimum. A different algorithm with faster convergence is Newton's method, where $\boldsymbol{h}$ is calculated from:

$$\boldsymbol{F}''(\boldsymbol{x})\boldsymbol{h} = -\boldsymbol{F}'(\boldsymbol{x}) \tag{2.16}$$

The downside of this algorithm is its lack of robustness and the computational time required to calculate the Hessian $\boldsymbol{F}''$. If the higher order derivatives are neglected, the Hessian can be written as the product of the Jacobian ($\boldsymbol{J}_f$) transposed times the Jacobian. Then $\boldsymbol{h}$ is calculated from:

$$\boldsymbol{J}_f(\boldsymbol{x})^T \boldsymbol{J}_f(\boldsymbol{x})\boldsymbol{h} = -\boldsymbol{F}'(\boldsymbol{x}) \tag{2.17}$$

This method is known as the Gauss-Newton's method. Another type of algorithm combines the fast convergence from the Gauss-Newton's method and the robustness of the steepest descent. This algorithm is known as the Levenberg-Marquardt, and $\boldsymbol{h}$ is calculated from:

$$(\boldsymbol{J}_f(\boldsymbol{x})^T \boldsymbol{J}_f(\boldsymbol{x}) + \mu \boldsymbol{I})\boldsymbol{h} = -\boldsymbol{F}'(\boldsymbol{x}) \tag{2.18}$$

The LM parameter μ influences the direction $\boldsymbol{h}$, for small values of μ the search direction will be close to the Gauss-Newton's direction. For large values of μ the search direction will be close to the steepest descent direction. The algorithm was improved by Marquardt to avoid slow convergence in the direction of small gradients. Here $\boldsymbol{h}$ is calculated from:

$$\left(\boldsymbol{J}_f(\boldsymbol{x})^T \boldsymbol{J}_f(\boldsymbol{x}) + \mu\, diag\left[\boldsymbol{J}_f(\boldsymbol{x})^T \boldsymbol{J}_f(\boldsymbol{x})\right]\right)\boldsymbol{h} = -\boldsymbol{F}'(\boldsymbol{x}) \tag{2.19}$$

When the LM algorithm is applied to minimize the TPE, then $\boldsymbol{F} = \Pi$ and $\boldsymbol{x} = \boldsymbol{u}^{(NL)}$. For clarity the superscript is left out and the displacement vector is represented as $\boldsymbol{u}$.

```
$\boldsymbol{u} = \boldsymbol{u}_0$
$k = 0$
$\mu = \mu_0$
repeat
        solve      $(\boldsymbol{K}_t + \mu\, diag[\boldsymbol{K}_t])\boldsymbol{h} = -\boldsymbol{R}$      (2.20)
        $\boldsymbol{u} = \boldsymbol{u} + \Delta\boldsymbol{u}$
        $k = k + 1$
until stop
```

The LM parameter both influences the direction as well as the size of $\boldsymbol{h}$. Now the LM parameter μ will be updated based on a gain factor g, given by:

$$g = \frac{\Pi(\boldsymbol{u}) - \Pi(\boldsymbol{u} + \Delta\boldsymbol{u})}{Q(0) - Q(\Delta\boldsymbol{u})} \tag{2.21}$$

$$
\begin{aligned}
\Pi(\boldsymbol{u}+\boldsymbol{\Delta u}) &\approx Q(\boldsymbol{\Delta u}) \\
&= \Pi(\boldsymbol{u}) + \frac{\partial \Pi}{\partial \boldsymbol{u}}\boldsymbol{\Delta u} + \frac{1}{2}\boldsymbol{\Delta u}^T \frac{\partial^2 \Pi}{\partial \boldsymbol{u}^2}\boldsymbol{\Delta u} \\
&= \Pi(\boldsymbol{u}) + \boldsymbol{R}\boldsymbol{\Delta u} + \frac{1}{2}\boldsymbol{\Delta u}^T \boldsymbol{K}_t \boldsymbol{\Delta u}
\end{aligned} \tag{2.22}
$$

Therefore the algorithm can be written as:

```
$\boldsymbol{u} = \boldsymbol{u}_0$
$k = 0$
$\mu = \mu_0$
repeat
        solve        $(\boldsymbol{K}_t + \mu\, diag[\boldsymbol{K}_t])\boldsymbol{h} = -\boldsymbol{R}$
        Compute $g$
        if $g > \delta$                                                         (2.23)
                     $\boldsymbol{u} = \boldsymbol{u} + \boldsymbol{\Delta u}$
                     $\mu = \mu\, max\{1/\gamma, 1-(\beta-1)(2g-1)^p\}$
        else
                     $\mu = 2\mu$
        $k = k+1$
until stop
```

For a converged displacement vector the incremental change $\boldsymbol{\Delta u}$ should be (almost) zero. The vector should also give equilibrium, which results in the residual vector $\boldsymbol{R}$ being (close to) zero. Therefore both the norm of the vector $\boldsymbol{\Delta u}$ or the norm of the vector $\boldsymbol{R}$ could be used as a stopping criteria. In the current implementation the norm of $\boldsymbol{\Delta u}$ has to be below a certain threshold for equilibrium.

The next step is to derive the residual force vector and tangent stiffness matrix. The residual force factor is defined as the gradient of the TPE and the tangent stiffness matrix is defined as the Hessian of the TPE.

RESIDUAL FORCE VECTOR

The residual force vector can be calculated as shown in Equation 2.24. Note that the partial derivative of a summation is the same as the summation of the partial derivatives. The order can be interchanged.

$$
\begin{aligned}
\boldsymbol{R} &= \frac{\partial \Pi}{\partial \boldsymbol{u}} \\
&= \frac{\partial}{\partial \boldsymbol{u}}\left(\frac{1}{2}\sum_{i=1}^{N_e} A_i E_i l_i \epsilon_i^2\right) - \frac{\partial}{\partial \boldsymbol{u}}\left(\boldsymbol{p}^T\boldsymbol{u}\right) \\
&= \sum_{i=1}^{N_e} A_i E_i l_i \epsilon_i \frac{\partial \epsilon_i}{\partial \boldsymbol{u}} - \boldsymbol{p}^T
\end{aligned} \tag{2.24}
$$

The next step is to calculate $\frac{\partial \epsilon_i}{\partial \boldsymbol{u}}$, which is shown below.

$$
\begin{aligned}
\frac{\partial \epsilon_i}{\partial \boldsymbol{u}} &= \frac{\partial}{\partial \boldsymbol{u}}\left(\frac{1}{l_i^2}\boldsymbol{b}_i^T\boldsymbol{u} + \frac{1}{2l_i^2}\boldsymbol{u}^T\tilde{\boldsymbol{B}}_i\boldsymbol{u}\right) \\
&= \frac{\partial}{\partial \boldsymbol{u}}\left(\frac{1}{l_i^2}\boldsymbol{b}_i^T\boldsymbol{u}\right) + \frac{\partial}{\partial \boldsymbol{u}}\left(\frac{1}{2l_i^2}\boldsymbol{u}^T\tilde{\boldsymbol{B}}_i\boldsymbol{u}\right) \\
&= \frac{1}{l_i^2}\boldsymbol{b}_i^T + \frac{1}{2l_i^2}\boldsymbol{u}^T(\tilde{\boldsymbol{B}}_i + \tilde{\boldsymbol{B}}_i^T) \\
&= \frac{1}{l_i^2}\boldsymbol{b}_i^T + \frac{1}{l_i^2}\boldsymbol{u}^T\tilde{\boldsymbol{B}}_i
\end{aligned} \tag{2.25}
$$

Realizing that the matrix $\tilde{\boldsymbol{B}}_i$ is symmetric, which means that the transpose of the matrix is equal to the matrix itself, allows for further simplifications as done in the last step. Substituting this expression into Equation 2.24 gives the final expression for the residual force factor. This can also be written as the internal force vector minus the external force vector. Once the internal force vector balances the external force vector, the structure is in equilibrium.

$$\begin{aligned} \boldsymbol{R} &= \sum_{i=1}^{N_e} A_i E_i l_i \left(\frac{1}{l^2} \boldsymbol{b}_i^T \boldsymbol{u} + \frac{1}{2l^2} \boldsymbol{u}^T \tilde{\boldsymbol{B}} \boldsymbol{u} \right) \left(\frac{1}{l_i^2} \boldsymbol{b}_i^T + \frac{1}{l_i^2} \boldsymbol{u}^T \tilde{\boldsymbol{B}}_i \right) - \boldsymbol{p}^T \\ &= \boldsymbol{F}_{int} - \boldsymbol{F}_{ext} \end{aligned} \tag{2.26}$$

TANGENT STIFFNESS MATRIX

Similarly, the tangent stiffness matrix can be calculated.

$$\begin{aligned} \boldsymbol{K_t} &= \frac{\partial^2 \Pi}{\partial \boldsymbol{u}^2} \\ &= \frac{\partial \boldsymbol{R}}{\partial \boldsymbol{u}} \\ &= \frac{\partial}{\partial \boldsymbol{u}} \left(\sum_{i=1}^{N_e} A_i E_i l_i \epsilon_i \frac{\partial \epsilon_i}{\partial \boldsymbol{u}} \right) - \frac{\partial}{\partial \boldsymbol{u}} \left(\boldsymbol{p}^T \right) \\ &= \sum_{i=1}^{N_e} A_i E_i l_i \left(\frac{\partial \epsilon_i}{\partial \boldsymbol{u}}^T \frac{\partial \epsilon_i}{\partial \boldsymbol{u}} + \epsilon_i \frac{\partial^2 \epsilon_i}{\partial \boldsymbol{u}^2} \right) \end{aligned} \tag{2.27}$$

The term $\frac{\partial \epsilon_i}{\partial \boldsymbol{u}}$ has already been determined. Only an expression for the second derivative of the strains has not yet been derived. This is done in Equation 2.28.

$$\begin{aligned} \frac{\partial^2 \epsilon_i}{\partial \boldsymbol{u}^2} &= \frac{\partial}{\partial \boldsymbol{u}} \left(\frac{\partial \epsilon_i}{\partial \boldsymbol{u}} \right) \\ &= \frac{\partial}{\partial \boldsymbol{u}} \left(\frac{1}{l_i^2} \boldsymbol{b}_i^T + \frac{1}{l_i^2} \boldsymbol{u}^T \tilde{\boldsymbol{B}}_i \right) \\ &= \frac{1}{l_i^2} \tilde{\boldsymbol{B}}_i \end{aligned} \tag{2.28}$$

Substituting gives the final expression for the tangent stiffness matrix:

$$\boldsymbol{K}_t = \sum_{i=1}^{N_e} A_i E_i l_i \left[\left(\frac{1}{l_i^2} \boldsymbol{b}_i^T + \frac{1}{l_i^2} \boldsymbol{u}^T \tilde{\boldsymbol{B}}_i \right)^T \left(\frac{1}{l_i^2} \boldsymbol{b}_i^T + \frac{1}{l_i^2} \boldsymbol{u}^T \tilde{\boldsymbol{B}}_i \right) + \left(\frac{1}{l^2} \boldsymbol{b}_i^T \boldsymbol{u} + \frac{1}{2l^2} \boldsymbol{u}^T \tilde{\boldsymbol{B}} \boldsymbol{u} \right) \left(\frac{1}{l_i^2} \tilde{\boldsymbol{B}}_i \right) \right] \tag{2.29}$$

As a consequence of the GL strain measure, the stiffness matrix is a function of the nodal displacements. The stiffness matrix is no longer constant, as is the case for a linear analysis. This dependence requires therefore an iterative procedure to solve for the nodal displacements. In the linear case the stiffness matrix is assumed to be independent of the displacement vector and will therefore remain constant, then the displacement vector could be obtained in a single step. The linear step will be covered next.

LINEAR STEP

Once the actuation step has converged the second step will be performed, where the loading is applied. The equation to be solved is given by Equation 2.30. Here $\boldsymbol{K}_t$ is the converged tangent stiffness matrix from first step.

$$\boldsymbol{K}_t \boldsymbol{u}^{(L)} = \boldsymbol{F} \tag{2.30}$$

As mentioned in the beginning of this chapter in the second step the stiffness matrix is assumed to remain constant. Hence solving for $\boldsymbol{u}^{(L)}$ can be done in a single step by pre-multiplying both sides of Equation 2.30

with the inverse of $\boldsymbol{K}_t$. The displacement field obtained in this step can be interpreted as the deviation from the intended trajectory, resulting from the applied loading. This deviation will be minimized in the mechanism design optimization process, as will be explained in the next chapter. If the loading was applied simultaneously with the prescribed displacements, then only one displacement field would be found and the deviation from the intended trajectory would remain unknown.

THREE DIMENSIONAL

In this section the changes in the FEA required for 3D are discussed. In 2D the nodal displacements were arranged as follows in the vector $\boldsymbol{u}$:

$$\boldsymbol{u} = \begin{bmatrix} u_1^{(1)} \\ u_2^{(1)} \\ u_1^{(2)} \\ u_2^{(2)} \\ \vdots \\ u_1^{(N_n)} \\ u_2^{(N_n)} \end{bmatrix} \tag{2.31}$$

On the first entry the displacement in the 1-direction of node 1 is displayed, on the second entry the displacement in the 2-direction of node 1 is displayed. Similarly, on the third and fourth entry the displacements in the 1- and 2-direction of the second node are located. This resulted in the following $\boldsymbol{B}$ matrix for the formulation of the strains, as was given by Equation 2.9 and repeated here:

$$\boldsymbol{B} = \begin{bmatrix} 1 & 0 & -1 & 0 \\ 0 & 1 & 0 & -1 \\ -1 & 0 & 1 & 0 \\ 0 & -1 & 0 & 1 \end{bmatrix} \tag{2.32}$$

For 3D the nodal displacements will be arranged as follows:

$$\boldsymbol{u} = \begin{bmatrix} u_1^{(1)} \\ u_2^{(1)} \\ u_3^{(1)} \\ u_1^{(2)} \\ u_2^{(2)} \\ u_3^{(2)} \\ \vdots \\ u_1^{(N_n)} \\ u_2^{(N_n)} \\ u_3^{(N_n)} \end{bmatrix} \tag{2.33}$$

In analogy to the 2D strain formulation, the following $\boldsymbol{B}$ matrix can be used to calculate the strains.

$$\boldsymbol{B} = \begin{bmatrix} 1 & 0 & 0 & -1 & 0 & 0 \\ 0 & 1 & 0 & 0 & -1 & 0 \\ 0 & 0 & 1 & 0 & 0 & -1 \\ -1 & 0 & 0 & 1 & 0 & 0 \\ 0 & -1 & 0 & 0 & 1 & 0 \\ 0 & 0 & -1 & 0 & 0 & 1 \end{bmatrix} \tag{2.34}$$

The expression for the strain therefore remains unchanged and the strain can in 3D be written as was already given by Equation 2.11, and repeated here:

$$\epsilon = \frac{1}{l^2}\boldsymbol{b}^T\boldsymbol{u} + \frac{1}{2l^2}\boldsymbol{u}^T\tilde{\boldsymbol{B}}\boldsymbol{u} \tag{2.35}$$

Carrying out the multiplications yields as expected the strain measure for 3D, which is given by Equation 2.36.

$$\epsilon = \frac{\partial \boldsymbol{u}_1}{\partial x} + \frac{1}{2}\left[\left(\frac{\partial \boldsymbol{u}_1}{\partial x}\right)^2 + \left(\frac{\partial \boldsymbol{u}_2}{\partial x}\right)^2 + \left(\frac{\partial \boldsymbol{u}_3}{\partial x}\right)^2\right] \tag{2.36}$$

The entire approach previously described remains the same. Only the ***B*** matrix is slightly changed and as a consequence the dimensions of the problem, accounting for the third dimension. With this newly defined matrix the total potential energy can be minimized.

2.1.2. VERIFICATION

An important step in developing a software tool is verification. Verification is done by answering the following question:

"Are we building the system right?"

Answering the question means that the different components of the tool developed for this thesis should be checked with other (numerical) tools, if available, to see whether the tool developed behaves the way it is supposed to behave. For the finite element tool both 2D and 3D will be verified.

In 2D the tool will be verified with the Von Mises truss structure, since the analytical solution is known. In 3D no analytical solution is known, therefore a simple geometry (a 3D version of the Von Mises truss) has been sketched in Abaqus to see how the forces and displacements compare. The input file for the Abaqus model is included in Appendix A.

TWO DIMENSIONAL

The Von Mises truss is a relatively simple structure of which the analytical solution is known. Which makes this structure very suitable for verification. The force-displacement curve will be compared for this verification. An illustration of the structure can be found in Figure 2.2. The symmetric structure consists of two connected truss members, each at one end pinned. In the tool the deformation was displacement controlled to prevent snap-through.

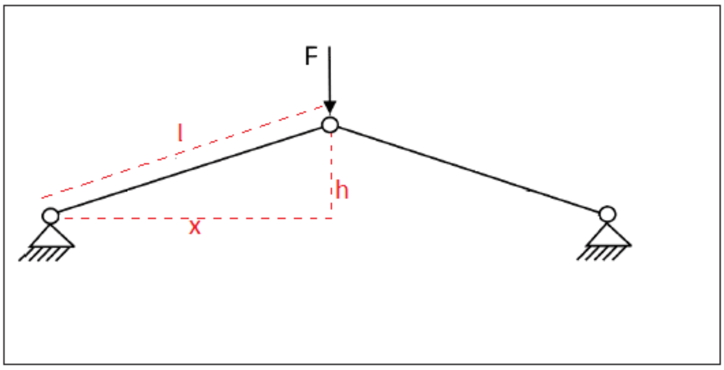

Figure 2.2: Illustration of the 2D Von Mises truss

Two verification cases of the Von Mises truss will be used to verify the finite element tool in 2D. The first verification case has an initial inclination of 15 degrees and the second one has 45 degrees. For the first verification case the analytical solution presented by Bathe [2] will be used. The analytical solution for the structure gives the relation between the applied force and the nodal displacement. The assumption, however, is that the axial force of the truss member could be modeled as $\boldsymbol{F} = \boldsymbol{k}\boldsymbol{u}$. Hence it is assumed that the axial stiffness of the member remains constant, which is only valid for small strains. The following solution was derived by Bathe:

$$F = 2kl\left(-1 + \frac{1}{\left[1 - 2\frac{\Delta}{l}sin(15°) + \left(\frac{\Delta}{l}\right)^2\right]^{1/2}}\right)\left(sin(15°) - \frac{\Delta}{l}\right) \tag{2.37}$$

Here l represents the length of each truss, k is the axial stiffness, equal to EA/l. E here is the Young's Modulus and A is the cross-sectional area. Finally, Δ represents the downward deflection.

Since the first verification case is only able to verify small strains accurately, another verification case has been used. This case has been obtained from the book of Crisfield [10]. The inclination angle is 45 degrees, resulting in larger strains. Furthermore in the book is Crisfield the following parameters were used:

$$
\begin{aligned}
x &= 2500 \\
h &= 2500 \\
A &= 100 \\
E &= 5\text{x}10^5
\end{aligned}
$$

The length of the truss member, l, can be calculated by $\sqrt{x^2+h^2}$. It has been decided that the same values for the cross-sectional area, Young's modulus and length of the truss members were used in both verification cases. Therefore the only difference is the initial inclination.

As can be clearly seen from Figure 2.3a, the results of the tool developed match very well the analytical solution from Bathe. Only a very small deviation can be seen at the peak and the valley of the force-displacement curve. This minor difference can be explained by the fact that only for small strains the analytical solution can be used for verification, while at the peak and valley the strains are the largest. It can be concluded that the finite element tool matches the results from Bathe and the tool has been verified for small strains.

Even for large strains the FEM code is able to calculate the force displacement relation. This, however, can no longer be compared to the analytical solution. Therefore a different numerical implementation, shown in the book of Crisfield, has been used. Figure 2.3b shows the force displacement curves of both tools. One can clearly see that both implementations give the same result. It can be concluded that the finite element tool is able to correctly calculate the force-displacement curve, even for large deformations. Hence, the tool has been successfully verified.

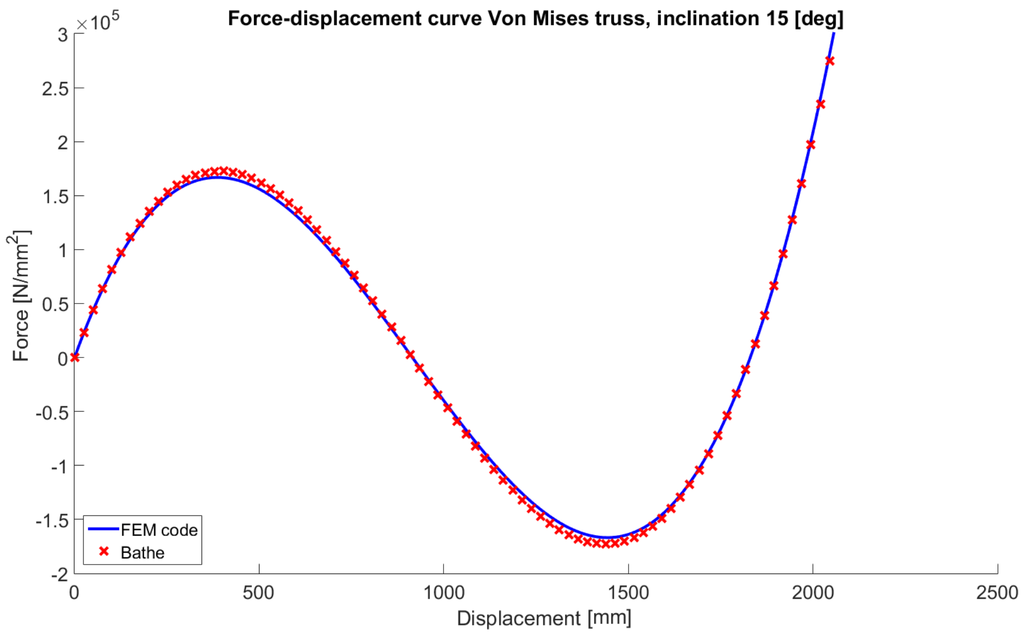

(a) Force-displacement curves of FEM code and analytical solution by Bathe with initial inclination 15°

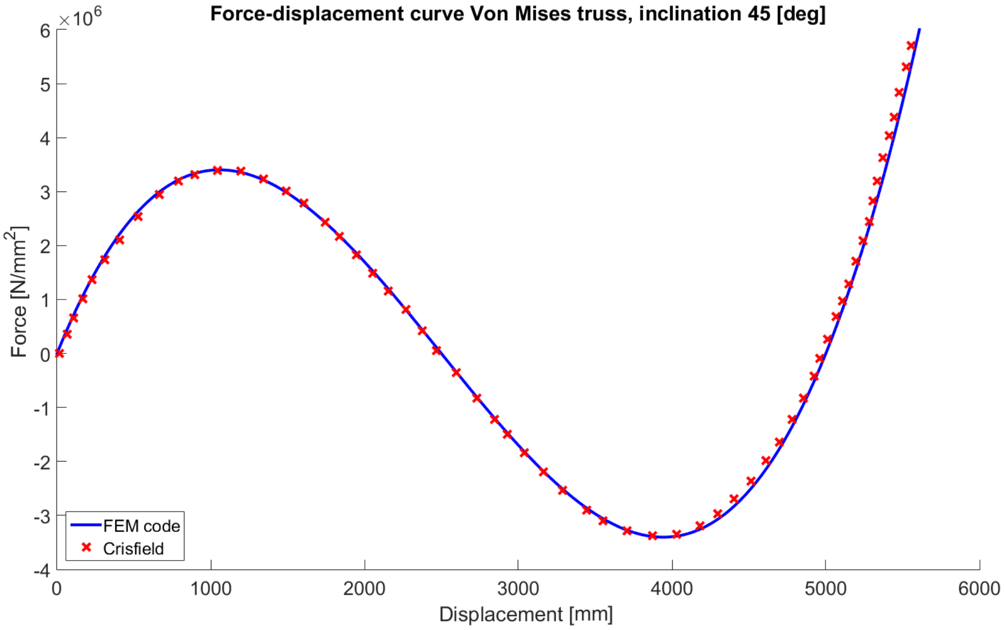

(b) Force-displacement curves of FEM code and numerical solution by Crisfield with initial inclination 45°

Figure 2.3: Verification of FEM code, 2D Von Mises truss with inclinations of 15° and 45°

THREE DIMENSIONAL

For the 3D verification of the finite element tool no analytical solution is known, which could be used. Therefore it has been decided to draw a structure in Abaqus, which is then compared to the results obtained from the finite element tool. The structure chosen for the verification is shown in Figure 2.4.

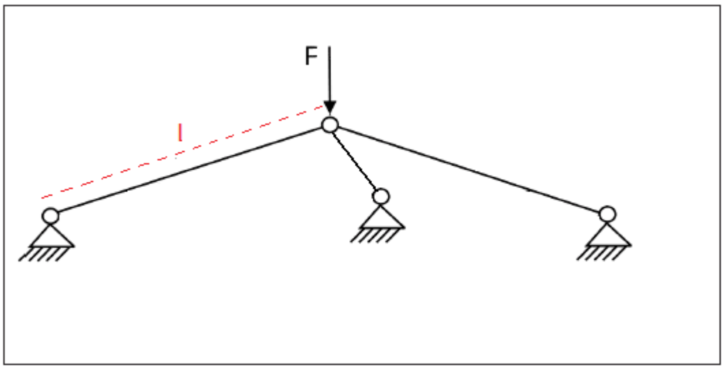

Figure 2.4: Illustration of the 3D Von Mises truss

The structure behaves similar to the 2D Von Mises truss. The structure will experience snap through as well. However the deformation is displacement controlled, thereby capturing also the unstable parts of the force displacement path. Similar to the 2D verification case, the initial inclination of 15 degrees is used, and the same length and cross-sectional area (for all three elements) were used. Only the angles between the elements are not yet defined, this can best be seen in Figure 2.5, which represents the model used in Abaqus. The angles between the three elements are defined as α, β, and γ. For this structure the angles are chosen such that no symmetry plane exists. As a consequence displacements in all three dimensions will occur, hereby verifying all three dimensions. The angles are defined in the xz-plane and set equal to:

$$\begin{aligned} \alpha &= 90^\circ \\ \beta &= 112.5^\circ \\ \gamma &= 157.5^\circ \end{aligned}$$

The geometry as described above was modeled in Abaqus, the three lower nodes were all pinned, thereby constraining the three translational degrees of freedom. On the top node a displacement was enforced in the y- or U2-direction. The last step was to apply a mesh with elements that have the same strain measure. Different strain measures will solve a different set of equilibrium equations and as a result a different displacement field is obtained. However, the truss element in Abaqus uses logarithmic strain, rather than the GL strain used in the current finite element model. Therefore the truss members had to be meshed with 2 node cubic beam elements (B33 elements), which use the GL strain. The mesh had to be chosen such that each member had a single element. To reproduce the pinned connection at the top node, only the translational degrees of freedom were coupled. However, having a coupling constraint at the top node does not allow any other boundary conditions, such as the prescribed displacement in the y-direction. To overcome this, a reference node was added. This node was via a MPC constraint coupled with the top nodes of each element. Again, only the translational degrees of freedom were coupled to reproduce the pinned joint. Finally, the prescribed displacement could be applied to the reference node.

Of the four nodes three are pinned, hence only three degrees of freedom remain. The top node has three displacements in the x-, y-, and z-direction, called U1, U2, and U3 respectively. In addition, there will be a reaction force at the top node in the y-direction, as a result of the prescribed displacements. Hence, as an output the force displacement curve of U2 and R2 are plotted, shown in Figure 2.6. As can be seen a similar structural behavior is observed as was done in the 2D case. The structure will experience snap-through. In addition, the displacements U1 and U3 will be plotted as a function of U2, also shown in Figure 2.6. Comparing the results of Abaqus with the finite element code, the result match perfectly. Both for the force displacement curve as well as the displacements in U1 and U3. Hereby the tool is also verified in 3D and it works as intended.

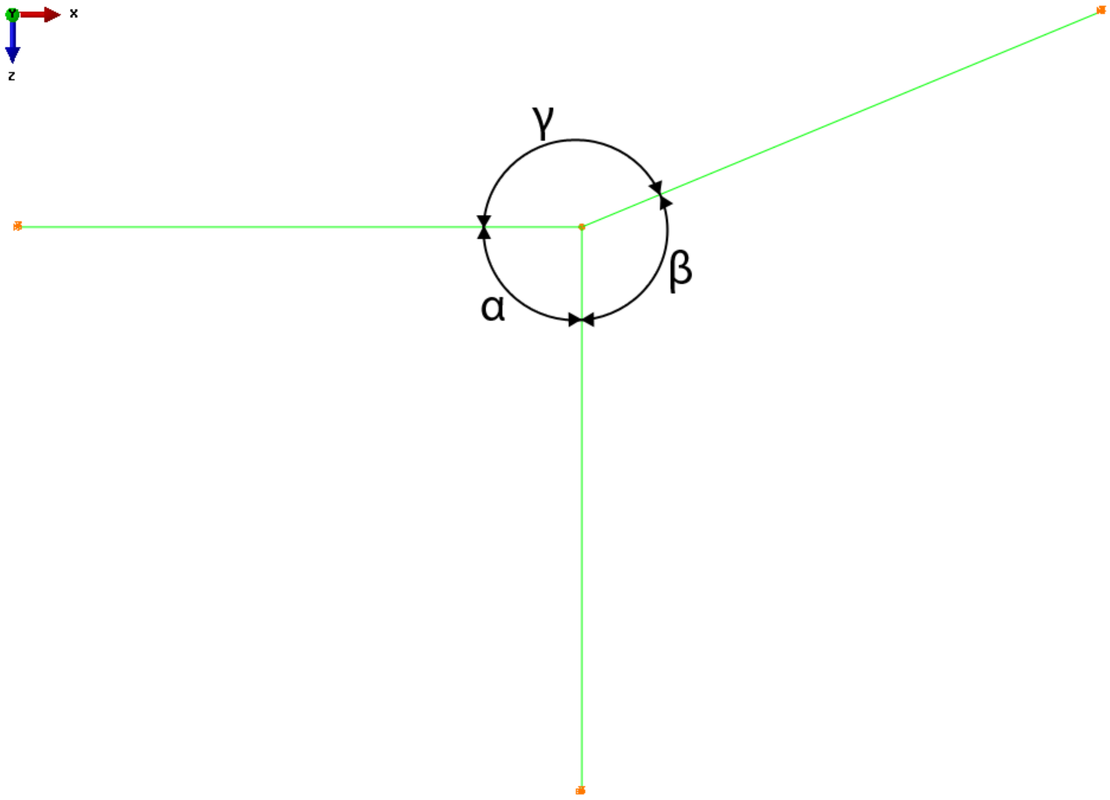

(a) top view

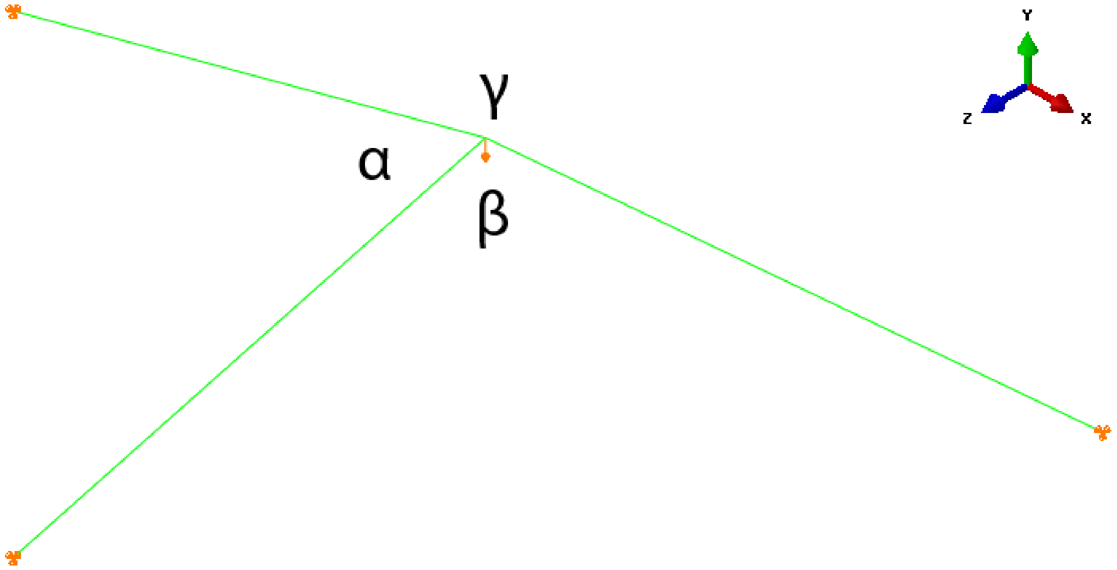

(b) 3D view

Figure 2.5: Schematic views of the 3D Von Mises truss in Abaqus with inclination of 15°

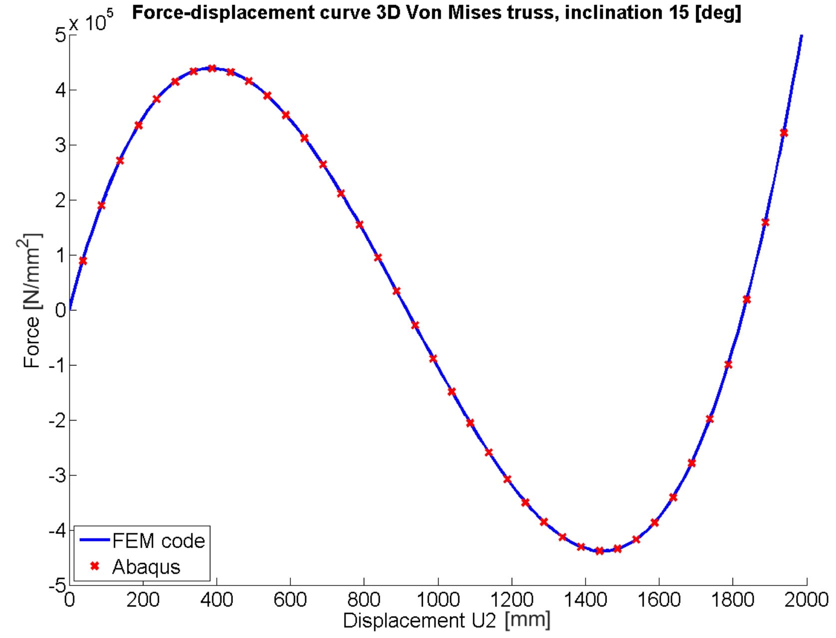

(a) Force-displacement curves of FEM code and Abaqus with initial inclination 15°

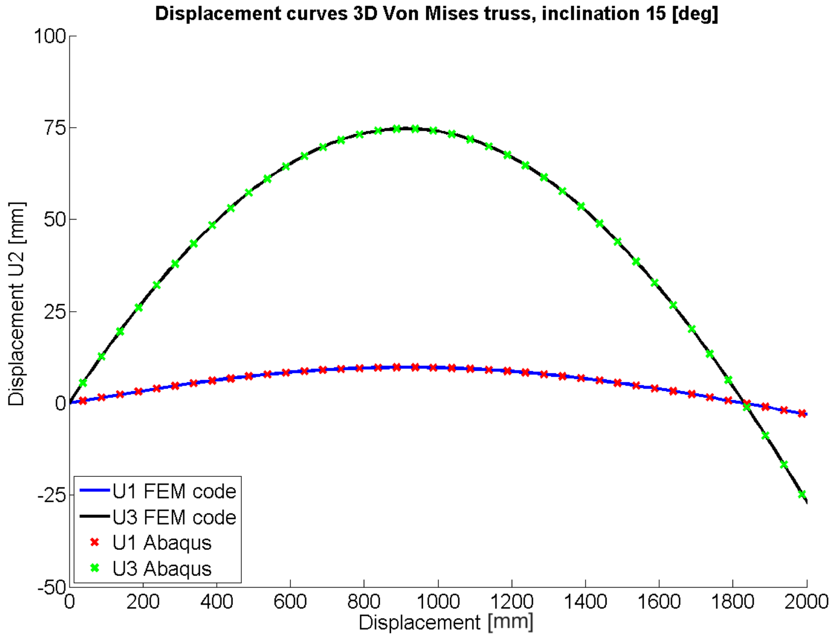

(b) Displacement curves of FEM code and Abaqus with initial inclination 45°

Figure 2.6: Verification of FEM code, 3D Von Mises truss with inclination of 15°

2.2. LINEAR BUCKLING ANALYSIS

Buckling is a critical state of the structure at certain load levels at which the structure exhibits large displacements or collapses. Global buckling, buckling of the structure as a whole, is often a critical failure mode and is always associated with compressive forces. When the mechanism is sized, i.e. when the cross-sectional areas of all elements are determined, they should be sufficient thick to prevent buckling failure.

The tool explained in this section performs a linear buckling analysis which calculates the buckling load factors and the corresponding buckling modes. When these factors are multiplied with the applied loading, the critical buckling loads are obtained. Hence as long as the factors are not between 0 and 1, the applied loading will not cause buckling. First will be explained how these buckling load factors and buckling modes are obtained, followed by the verification of the linear buckling analysis.

2.2.1. DESCRIPTION

The first step would be to rewrite the TPE as a function of the linear stiffness matrix ($\boldsymbol{K}_L$), the geometric stiffness matrix ($\boldsymbol{K}_G$), and the stiffness matrix containing the higher order terms ($\boldsymbol{K}_H$). Here the linear stiffness matrix is the initial stiffness of the structure, which contains the terms that are not a function of the displacement. Hence, this matrix would describe the stiffness of the structure when there are no displacements. The geometric stiffness matrix contains all the terms that are linear in displacement. Finally, the higher order terms (in displacement) are collected in $\boldsymbol{K}_H$, this term only becomes significant for large displacements. The TPE can be written as [30]:

$$\Pi(\boldsymbol{A},\boldsymbol{x},\boldsymbol{u}) = \frac{1}{2}\sum_{i=1}^{N_e} \boldsymbol{u}^T \left(\boldsymbol{K}_L(\boldsymbol{A},\boldsymbol{x}) + \boldsymbol{K}_G(\boldsymbol{A},\boldsymbol{u},\boldsymbol{x}) + \boldsymbol{K}_H(\boldsymbol{A},\boldsymbol{u},\boldsymbol{x})\right) - \boldsymbol{p}^T\boldsymbol{u} \tag{2.38}$$

With:

$$\begin{aligned} \boldsymbol{K}_L &= \sum_{i=1}^{N_e} \frac{A_i E_i}{l_i^3} \boldsymbol{b}_i \boldsymbol{b}_i^T \\ \boldsymbol{K}_G &= \sum_{i=1}^{N_e} \frac{A_i E_i}{l_i^3} \boldsymbol{b}_i^T \boldsymbol{u} \tilde{\boldsymbol{B}}_i \\ \boldsymbol{K}_H &= \sum_{i=1}^{N_e} \frac{A_i E_i}{l_i^3} \left(\tilde{\boldsymbol{B}}_i \boldsymbol{u}\right)\left(\tilde{\boldsymbol{B}}_i\, \boldsymbol{u}\right)^T \end{aligned} \tag{2.39}$$

In a linear buckling analysis the following generalized eigenvalue problem is solved:

$$(\boldsymbol{K}_L + \lambda_i \boldsymbol{K}_G)\,\boldsymbol{\phi}_i = 0 \tag{2.40}$$

Here λ_i is the i$^{\text{th}}$ buckling load factor and $\boldsymbol{\phi}_i$ describes the corresponding i$^{\text{th}}$ buckling mode. The buckling load factors are the solutions for which the geometric stiffness matrix results in a loss of stability. The smallest positive eigenvalue (λ_{cr}) gives the critical buckling load. To prevent buckling, λ_{cr} should be larger than one. As long as that is the case, the load is allowed to increase and no buckling will occur for the applied load.

To solve the generalized eigenvalue problem, both sides of the equations can be left-multiplied with the eigenvector transposed, giving:

$$\boldsymbol{\phi}_{cr}^T\,(\boldsymbol{K}_L + \lambda_{cr}\boldsymbol{K}_G)\,\boldsymbol{\phi}_{cr} = 0 \tag{2.41}$$

Solving this equation for the λ_{cr} gives:

$$\lambda_{cr} = -\frac{\boldsymbol{\phi}_{cr}^T \boldsymbol{K}_L \boldsymbol{\phi}_{cr}}{\boldsymbol{\phi}_{cr}^T \boldsymbol{K}_G \boldsymbol{\phi}_{cr}} \tag{2.42}$$

However, instead of solving the generalized eigenvalue problem given by equation 2.40, a slightly modified eigenvalue problem is solved as proposed by Bathe [2]. The reason is the possible indefiniteness of the geometric stiffness matrix. The linear stiffness matrix is real, symmetric and positive definite, whereas the geometric stiffness matrix is real, symmetric, but could be indefinite. Numerical difficulties could occur due to the indefiniteness of the geometric stiffness matrix. The modified problem solved is a generalized eigenvalue problem where both matrices are definite:

$$\boldsymbol{\phi}_{cr}^{T}\left((\boldsymbol{K}_L+\boldsymbol{K}_G)+\gamma_{cr}\boldsymbol{K}_L\right)\boldsymbol{\phi}_{cr}=0 \tag{2.43}$$

Now λ_{cr} can be obtained from:

$$\lambda_{cr}=\frac{1}{1-\gamma_{cr}} \tag{2.44}$$

The relation given by Equation 2.44 can be verified by calculating λ_{cr} from Equation 2.42. Both equations give indeed the same eigenvalue.

2.2.2. VERIFICATION

Also the linear buckling analysis tool will be verified. This will be done by using the same structure as used for the 2D finite element analysis. The Von Mises truss with an inclination of 45 degrees is used here. Also, since the geometry is symmetric, the structure could be reduced to a single truss member when applying the symmetry boundary conditions. Due to the symmetry, the upper node will only move up and down, it will not move left or right. Hence, the structure can be reduced to the geometry given by Figure 2.7. Since the structure only a a single free degree of freedom, the verification will be done analytically.

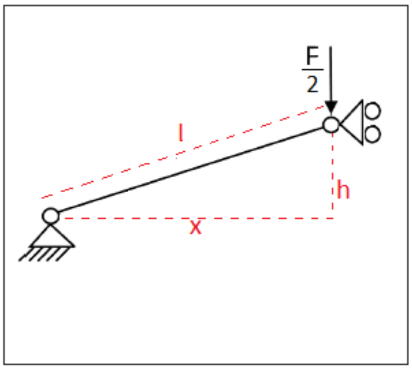

Figure 2.7: Illustration of the Von Mises truss, symmetry conditions applied

The exact same geometry is used as was done for the verification case with 45 degrees inclination. Hence the parameters used are:

$$\begin{aligned} x &= 2500 \\ h &= 2500 \\ A &= 100 \\ E &= 5\text{x}10^5 \end{aligned}$$

In addition, a unit force F pointing downward is assumed. This yields a buckling factor which is equal to the critical buckling load. In the reduced structure the applied loading will therefore be equal to a half.

Since this structure consists of a single element, the linear stiffness matrix and geometric stiffness matrix reduce to a scalars and no summation over the elements drops out as well. Hence, dropping the subscript i, the linear and geometric stiffness can be written as:

$$K_L=\frac{AE}{l^3}\boldsymbol{b}\boldsymbol{b}^T \tag{2.45}$$

$$K_G=\frac{AE}{l^3}\boldsymbol{b}^T\boldsymbol{u}\tilde{\boldsymbol{B}} \tag{2.46}$$

Recall that $\boldsymbol{b}$ is defined as $\hat{\boldsymbol{B}}\boldsymbol{x}$. Hence $\boldsymbol{b}$ is given by:

$$\boldsymbol{b} = b = \hat{\boldsymbol{B}}\boldsymbol{x} = \begin{bmatrix} 0 & -1 & 0 & 1 \end{bmatrix} \begin{bmatrix} 0 \\ 0 \\ x \\ h \end{bmatrix} = h \tag{2.47}$$

The displacement vector is the solution of the equilibrium equation after the force has been applied. This can be obtained by solving the following:

$$K_L u = -\frac{F}{2} \tag{2.48}$$

Since the structure has only a single degree of freedom, the equation reduces to a scalar equation and the downward displacement is simply equal to the applied loading (-1/2) divided by the stiffness. This gives:

$$u = -\frac{1}{2K_L} \tag{2.49}$$

The matrix $\tilde{\boldsymbol{B}}$ is equal to $\boldsymbol{B}$, where the rows and columns equal to the fixed degrees of freedom are removed. Since this structure has only a single degree of freedom (the 4^{th} one), the first three rows and columns will be removed. This yield simply the value 1 for $\tilde{\boldsymbol{B}}$.

Substituting all this gives the following expressions for the linear and geometric stiffness:

$$K_L = \frac{AEh^2}{l^3} \tag{2.50}$$

$$K_G = -\frac{AEh}{2l^3 K_L} = -\frac{AEhl}{2l^3 AEh^2} = -\frac{1}{2h} \tag{2.51}$$

Substituting Equations 2.50 and 2.51 into Equation 2.40 gives:

$$\left(\frac{AEh^2}{l^3} + \lambda\left(-\frac{1}{2h}\right)\right)\phi = 0 \tag{2.52}$$

Since the equation is a scalar equation, the critical buckling factor can be calculated as:

$$\lambda = -\frac{K_L}{K_G} = \frac{2AEh^3}{l^3} \tag{2.53}$$

And the normalized eigen mode would then be equal to 1 or -1, hence:

$$\phi = 1 \text{ or} -1 \tag{2.54}$$

Substituting the values yields a critical buckling factor of 3.5355e+07 for the analytical solution. Running the linear buckling analysis yields also 3.5355e+07 for λ. Also, the normalized buckling mode is the same. The results are shown in Table 2.1. Based on this it can be concluded that the linear buckling analysis performs as intended. Hence the tool has been verified.

Table 2.1: Verification of linear buckling analysis

Implementation	Eigenvalue	Eigenmode
Analytically	3.5355e+07	1 or -1
Numerically	3.5355e+07	1 or -1

2.3. POST-PROCESSING

The research objective defined in the previous chapter is to develop a tool to design a mechanism for morphing winglets, using ground-structure based topology optimization. Hence the primary objective is to design a suitable mechanism for a morphing winglet. This will be done using ground-structure based topology optimization techniques. Now a mechanism is characterized by its kinematics, its ability to perform a certain motion. The actuation of the mechanism is done by applying prescribed displacements at one or more nodes, defined as the input node(s). The desired motion of the mechanism is checked at different nodes, the output nodes. The post-processing is therefore tailored to calculate parameters which are needed in the optimizations to design and size a mechanism which is able to perform a specified motion without failure. This section elaborates on how these different parameters are calculated. How these parameters are used in the optimizations, will be covered in the next chapter.

2.3.1. FINITE ELEMENT ANALYSIS

In the previous sections the finite element analysis and linear buckling analysis were explained. The FEA solves the equilibrium equations, calculates the corresponding nodal displacements and reaction forces, as well as the elemental strains. The tool performs these calculations twice, the first time after the prescribed displacements were enforced (to obtain $\boldsymbol{u}^{(NL)}$), the second time in a single step after the loading is applied (to obtain $\boldsymbol{u}^{(L)}$). The first step is done incrementally, since the displacements and rotations as a result of the actuation could be large. In the second step the nodal displacements as a result of the loading are assumed to be small, hence this step is a linear one. How the displacements, reaction forces and strains are post-processed, will be explained in this section.

Compliance

The first parameter calculated is the compliance, which is defined as [62]:

$$C = \boldsymbol{F}^T \boldsymbol{u}^{(L)} \tag{2.55}$$

Here $\boldsymbol{F}$ is the external force vector and $\boldsymbol{u}^{(L)}$ is the displacement vector that is calculated in the linear step of the finite element analysis. A slightly different definition is $1/2\boldsymbol{F}^T\boldsymbol{u}^{(L)}$, but the definition given by [62] is often used in topology optimization and is therefore used here. Furthermore, the problems considered in this thesis assume a constant force vector, hence the loading does neither change over time nor change with the deformations. Compliance can be interpreted as the ability to deform. The smaller the compliance is, the greater the resistance to deform. Since the force vector is constant, the smaller the compliance, the smaller the displacement vector $\boldsymbol{u}^{(L)}$ must be. This results in a greater resistance against the deformations caused by the loading.

Actuation Force

The internal force vector calculates the nodal forces as a result of the prescribed displacements and/or applied loading. In the first step of the FEA only the prescribed displacements were enforced, hence this internal force vector represents their resistance against the prescribed displacements. The force required to enforce the prescribed displacement, i.e. the actuation force, is given by the entry of the internal force vector corresponding to the prescribed displacement. Defining a row vector $\boldsymbol{I}^{input}$ which contains all zeros except for the entry of the prescribed displacement, where it contains a one. Then the actuation force is given by:

$$F^{input} = \boldsymbol{I}^{input}\boldsymbol{F}_{int} \tag{2.56}$$

How $\boldsymbol{F}_{int}$ is calculated, is given by Equation 2.26. Note that the variable F^{input} is zero for mechanisms, but will be nonzero otherwise. Mechanisms, which posses a degree of freedom, can be actuated without deforming the elements.

Trajectory

The desired motion is checked at one or more the output nodes. Assuming a single output node, then the distance Δ between the actual location of the output node and the intended location is in 2D given by Equation 2.57 and in 3D given by 2.58.

$$\Delta = \sqrt{\left(u_x^{act} - u_x^{traj}\right)^2 + \left(u_y^{act} - u_y^{traj}\right)^2} \tag{2.57}$$

$$\Delta = \sqrt{\left(u_x^{act} - u_x^{traj}\right)^2 + \left(u_y^{act} - u_y^{traj}\right)^2 + \left(u_z^{act} - u_z^{traj}\right)^2} \tag{2.58}$$

Here u_x^{act}, u_y^{act}, and u_z^{act} are the actual x-, y-, and z-displacements of the output node, respectively. Similarly, u_x^{traj}, u_y^{traj}, and u_z^{traj} are the displacements corresponding to the intended trajectory. Defining a distance Δ^{max}, then the following ratio can be calculated:

$$R^{trajectory} = \frac{\Delta}{\Delta^{max}} \tag{2.59}$$

If this ratio is smaller than 1, the distance between the specified location and the actual location is smaller than Δ^{max}. For values larger than 1, this distance is larger than Δ^{max}. How this will be used in the optimizations, will be covered in the next chapter.

Local Buckling
For a pinned truss the critical column buckling load is given by 2.60:

$$P_i^{cr} = \frac{\pi^2 E_i I_i}{l_i^2} \tag{2.60}$$

Here E_i is the Young's modulus, I_i is the second moment of area (the moment of inertia), and l_i is the length of the i$^{\text{th}}$ member. Once the compressive force in element i exceeds P_i^{cr}, column/local buckling will occur. Assuming a solid cylinder as he shape for the truss members, the second moment of area is given by:

$$I_i = \frac{\pi}{4} r^4 = \frac{\pi}{4} r^4 = \frac{A_0^2 \rho_i^2}{4\pi} \tag{2.61}$$

A similar ratio as was done for the trajectory can be introduced.

$$R_i^{local\ buckling} = \frac{\rho_i A_0 E_i \epsilon_i}{P_i^{cr}} = \frac{F_i^{internal}}{P_i^{cr}} = -\frac{4 l_i^2 \epsilon_i}{\pi A_0 \rho_i} \tag{2.62}$$

As long as the ratio is smaller than 1, the compressive force in the i$^{\text{th}}$ truss member is smaller than the critical load and no buckling will occur. As soon as the ratio exceeds 1 for an element, it will fail due to column buckling.

Stress
In the beginning of this chapter it was assumed that the material remains linear elastic and that Hooke's law applies. Therefore the stress in the i$^{\text{th}}$ element is simply given by:

$$\sigma_i = E\epsilon_i \tag{2.63}$$

Dividing the stress by the yield stress σ_y, the following ratio can be introduced.

$$R_i^{stress} = \frac{\sigma_i}{\sigma_y} \tag{2.64}$$

As soon as the ratio exceeds one, the element stress exceeds the yield stress. This ratio can be defined for material failure in tension as well as in compression.

2.3.2. LINEAR BUCKLING ANALYSIS

The second analysis tool, the linear buckling analysis, solves a generalized eigenvalue problem to obtain the buckling load factors and the buckling modes. The post-processing of these results will also be covered here, which only applies to global buckling.

Global Buckling
It was previously covered that values smaller than 1 for λ_{cr} mean global buckling. To keep the consistency within the post-processing, λ_{cr} is renamed $R^{global\ buckling}$.

$$R^{global\ buckling} = \lambda_{cr} \tag{2.65}$$

2.3.3. GEOMETRY

The last section of the post-processing covers the geometry. For a given geometry, its weight, number of elements and input node connectivity can be determined.

Weight

The weight of the mechanism is calculated by multiplying the density of the material ρ^m with the volume of the structure. The total volume is simply the sum of the volume of each element. The weight calculation is given by Equation 2.66.

$$W = \rho^m \sum_{i=1}^{N_e} A_i l_i \tag{2.66}$$

Volume

Topology optimization was defined as the process of optimizing both the material layout and the connectivity inside a design domain [56]. For the ground-structure approach this means that the optimizer determines which elements are needed and which ones can be removed from the design space. The presence of the elements are determined by the vector $\boldsymbol{\rho}$. The entries of this vector range from (almost) 0 to 1, thereby expressing the required presence (or absence). If for the i$^{\text{th}}$ element this value is 1, the element should be maintained, if it is 0 then it should be removed. How this vector is updated (and thereby changing the geometry) will be covered in the next chapter. Now, summing over all the entries of this vector, the number of element in the geometry can be determined. This is mathematically shown in Equation 2.67.

$$V = \sum_{i=1}^{N_e} \rho_i \tag{2.67}$$

Now introducing a maximum number of elements V^{max}, the following ratio can be determined.

$$R^{volume} = \frac{V}{V^{max}} \tag{2.68}$$

Below 1 the number of elements is smaller than V_{max}, above 1 the maximum number of elements is exceeded.

Input node connectivity

The input node connectivity describes the number of elements attached to the input node. It was already explained that the vector $\boldsymbol{\rho}$ contains the informations which elements are present in the geometry. Now define a set $inp.node$ which contains the elements connected to the input node, then summing over those elements only will give the input node connectivity.

$$C_{input\ node} = \sum_{i \in inp.node} \rho_i \tag{2.69}$$

Now introducing a lower limit $C^{min}_{input\ node}$, the ratio $R^{inputnode}$ can be determined.

$$R^{input\ node} = \frac{C_{input\ node}}{C^{min}_{input\ node}} \tag{2.70}$$

For values greater than 1, the number of elements is larger than the $C^{min}_{input\ node}$. And for values smaller than 1 $C^{min}_{input\ node}$ is larger than the input node connectivity number. How this will be incorporated in the optimizations, will be covered in the next chapter.

3

OPTIMIZATION

As mentioned in the introduction, topology optimization can be defined as the process of optimizing both the material layout and the connectivity inside a design domain [56]. Within this context topology optimization can be described in general as the optimization problem of finding the material distribution that minimizes an objective function F_0, usually subjected to (1) a volume constraint in the form of $G_1 \leq 0$, and (2) possibly $M-1$ other constraints $G_j \leq 0, j = 2, ..., M$. In mathematical form the problem can be written as [56]:

$$\begin{aligned} &\underset{\rho}{min}\, F_0 = F_0(\mathbf{u}(\rho), \rho) = \int_\Omega f(\mathbf{u}(\rho), \rho) dV \\ &s.t. = \begin{cases} G_1(\rho) = \int_\Omega \rho(\mathbf{x}) dV - V_0 & \leq 0 \\ G_j(\mathbf{u}(\rho), \rho) & \leq 0 \qquad j = 2, ..., M \\ \rho(\mathbf{x}) & = \{0, 1\} \quad \forall\, \mathbf{x} \in \Omega \end{cases} \end{aligned} \tag{3.1}$$

In this formulation the material distribution is described by the density variable $\rho(\mathbf{x})$, which takes the values 0 (no material present) or 1 (material present) throughout the design space Ω. The state field $\mathbf{u}$ satisfies the (non-)linear state equations. As is commonly done to solve Equation 3.1, the design space Ω is discretized into many finite elements. Each element i ($i = 1, ..., N$) is then described by the density variable ρ_i, being either 0 or 1. Defining the density variables as the design variables, then the optimizer determines which elements remain in the design space ($\rho_i = 1$) and which elements need to be removed ($\rho_i = 0$) in order to minimize the objective function, while satisfying the constraints. The problem can be rewritten as shown in Equation 3.2 [56].

$$\begin{aligned} &\underset{\rho\rho}{min}\, F_0 = F_0(\mathbf{u}(\boldsymbol{\rho}), \boldsymbol{\rho}) = \sum_i \int_{\Omega_i} f(\mathbf{u}(\rho_i), \rho_i) dV \\ &s.t. = \begin{cases} G_1(\boldsymbol{\rho}) = \sum_i v_i \rho_i - V_0 & \leq 0 \\ G_j(\mathbf{u}(\boldsymbol{\rho}), \boldsymbol{\rho}) & \leq 0 \qquad j = 2, ..., M \\ \rho_i & = \{0, 1\} \quad i = 1, ..., N \end{cases} \end{aligned} \tag{3.2}$$

However, it is well-known that problems described by Equations 3.1 and 3.2 may lack solutions [57], closedness of the design space, and/or exhibit mesh-dependent solutions [56]. Attempts have been made to solve these issues by relaxation of the integer constraints. By relaxing is meant that the density variables are no longer discrete, but can take all values between 0 and 1. Mathematically, the optimization problem can be represented as [56]:

$$\begin{aligned} &\underset{\rho\rho}{min}\, F_0 = F_0(\mathbf{u}(\boldsymbol{\rho}), \boldsymbol{\rho}) = \sum_i \int_{\Omega_i} f(\mathbf{u}(\rho_i), \rho_i) dV \\ &s.t. = \begin{cases} & G_1(\boldsymbol{\rho}) = \sum_i v_i \rho_i - V_0 & \leq 0 \\ & G_j(\mathbf{u}(\boldsymbol{\rho}), \boldsymbol{\rho}) & \leq 0 \quad j = 2, ..., M \\ 0 \leq & \rho_i & \leq 1 \quad i = 1, ..., N \end{cases} \end{aligned} \tag{3.3}$$

This problem formulation allows for gradient-based solvers. These solvers are in general faster, because they make use of derivatives (sensitivities) to determine in which direction to proceed the search. In this way not the entire design space has to be searched, thereby reducing the computational time. A downside for non-convex problems is that gradient based algorithms tend to find only a local minimum rather than the global minimum.

By relaxing the problem formulation, the design variables ρ_i are also relaxed. This means that the design variables are no longer discrete, i.e. either 0 or 1, but are continuous and therefore range from 0 to 1. However, interpreting intermediate values is difficult, since the design variable ρ_i reflects the presence of element i. The element cannot be partially present, therefore in the optimization the design vector should be stimulated to yield either 0 or 1 for the design variables. This is done by introducing a penalization method for the intermediate densities. Within the different penalization techniques the implicit and explicit methods can be distinguished. The explicit methods are characterized by a constraint (or additional term in the objective function) which promotes a 0/1 design. Examples of these constraints include the quadratic penalization method, the sum of reciprocal variables (SRV) and the squared sum of variables (SSV). The implicit penalization methods are characterized by a material interpolation scheme where intermediate densities are penalized to make these elements less efficient in carrying the load. In combination with a volume constraint and a loading the optimizer will be steered towards using only efficient members. This also promotes a 0/1 design. Examples of different implicit penalization schemes include the Rational Approximation of Material Properties (RAMP), Hashin-Shtrikman, and the Reuss-Voigt models. However, the most popular implicit penalization is the Solid Isotropic Material with Penalization (SIMP) method, as proposed by Bendøe and originally introduced for continuum topology optimization in 1989 [3]. The penalization scheme is given by equation 3.4.

$$E = \rho^p E_0 \qquad p \geq 2 \tag{3.4}$$

The penalized Young's modulus is plotted as a function of ρ for three different values of the penalization factor p in Figure 3.1.

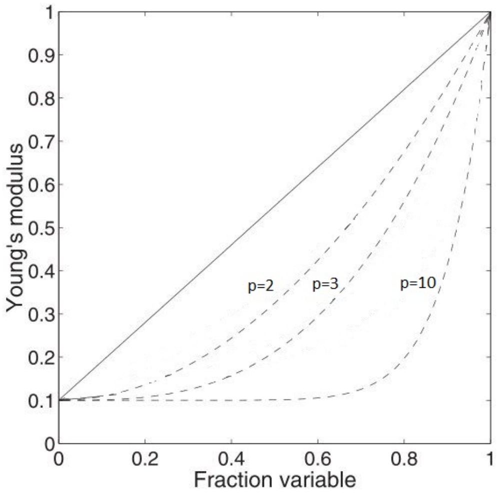

Figure 3.1: Penalized Young's Moduli for the SIMP approach (p = 2,3,10)

The continuous line represents the actual stiffness, the dashed lines represent the penalized stiffnesses. At ρ equal to 0 or 1, the actual stiffness is recovered but for all intermediates densities a reduced stiffness will result. As a consequence the members with an intermediate value for ρ encounter a penalized stiffness and are therefore less efficient in carrying load. If the objective contains a term that tries to maximize the stiffness and problem is subjected to a volume constraint, then the optimizer will steer the design variables to 0 and 1 to maximize stiffness. As an example, due to the penalization the optimizer prefers one element on a certain location with the density equal to 1 than two (overlapping) elements with densities equal to a half.

A very similar approach has been used by Kawamoto [30] for the ground structure approach. Instead of penalizing the Young's modulus, the cross-sectional areas of the elements are penalized:

$$A_i = \rho_i^p A_0 \qquad p \geq 2 \tag{3.5}$$

Common practice is to introduce a lower bound on the density variables (ρ_{min}). This prevents numerical issues such as a singular stiffness matrix and/or insensitivity of the objective function to changes in the design variables below a lower bound [32]. The lower bound is a small number, slightly larger than zero:

$$0 < \rho_{min} \leq \rho_i \leq 1 \tag{3.6}$$

Due to the limited computational time, a gradient-based method has been selected to solve the optimization problems. The optimizer used is GCMMA as developed by professor Svanberg [64]. SIMP has been selected as the penalization method. The penalty factors was set to 3, which is common for the SIMP method. In Section 3.1 the optimizer GCMMA will be discussed in more detail. The optimizer is used for the optimizations. In the next section the optimization strategy will be covered. Here will be explained why the tool developed consists of two optimizations (i.e. mechanism design and mechanism sizing) and how these optimization problems are formulated. Finally, the Sections 3.3 and 3.4 will cover each optimization problem in more detail, including the derivation of the sensitivities. These sensitivities are used by the GCMMA optimizer to determine the search direction.

3.1. GLOBALLY CONVERGENT METHOD OF MOVING ASYMPTOTES

This section starts with the basics of the optimizer. The globally convergent method of moving asymptotes is a convex sequential programming technique. The optimizer replaces the objective function and constraints by convex approximations, which are then solved. How these approximations are formulated, will be discussed here. Once the approximations are solved, the sensitivities will be calculated to determine how the design vector is updated to solve the optimization problem. The method selected for obtaining the sensitivities is the adjoint method. Why this method is selected and how this method works, will be covered here as well.

3.1.1. DESCRIPTION

A powerful approach to solve non-linear structural optimization problems is to replace the (usually implicit) objective and constraint functions with convex explicit separable functions. This technique is known as convex sequential programming. There are several ways to construct a separable explicit approximations via Taylor expansions, including convex expansion, reciprocal expansion, direct (linear) expansion, diagonal quadratic expansion, shifted convex expansion (incl. MMA and GCMMA), and power expansion [47]. The basic steps in the algorithms are [63]:

- In each iteration, start with the current design vector $\boldsymbol{x}^{(k)}$
- Formulate a sub-problem by replacing the objective and constraints with convex approximations
- The unique and optimal solution of the sub-problem will be the next design vector $\boldsymbol{x}^{(k+1)}$

For the MMA it is possible not to converge, based on the chosen initial vector. If an infeasible solution is used as the initial vector, in might not find a local minimum. Svanberg has improved the MMA algorithm to make sure it finds a local minimum even for an infeasible starting point. The new updated algorithm is known as GCMMA. It stands for globally convergent method of moving asymptotes. Globally convergent refers to its ability to find a local minimum even for infeasible starting points. It does not mean the algorithm will find the global minimum. The GCMMA makes use of an inner and an outer loop. The inner loop checks, based on the function and constraint values, whether the approximation is conservative or not. If that is the case, then the conservative convex separable approximations (CCSA) are solved [64], according to the steps described previously. The solution to these approximations will be the updated design vector.

The choice of these approximations are based on the first derivatives of the function at the current iteration and on the parameters $U^{(k)}$ and and $L^{(k)}$. These parameters are known as the moving asymptotes. These moving asymptotes increase both the stability and convergence rate of the optimization process. The approximations are constructed as follows [63]:

$$\tilde{G}_j(\boldsymbol{x}^{(k)})) = G_j(\boldsymbol{x}^{(k)}) + \sum_{i=1}^{N} p_{ij}^{(k)} \left(\frac{1}{U_i^{(k)} - x_i} - \frac{1}{U_i^{(k)} - x_i^{(k)}} \right) + \sum_{i=1}^{N} q_{ij}^{(k)} \left(\frac{1}{x_i - L_i^{(k)}} - \frac{1}{x_i^{(k)} - L_i^{(k)}} \right) \tag{3.7}$$

With

$$\begin{aligned} p_{ij}^{(k)} &= (U_i^{(k)} - x_i^{(k)})^2 \left[1.001 \left(\frac{\delta G_j}{\delta x_i}(\boldsymbol{u}^{(k)}) \right)^+ + 0.001 \left(\frac{\delta G_j}{\delta x_i}(\boldsymbol{u}^{(k)}) \right)^- + \frac{10^{-5}}{x_i^{max} - x_i^{min}} \right] \\ q_{ij}^{(k)} &= (x_i^{(k)} - L_i^{(k)})^2 \left[0.001 \left(\frac{\delta G_j}{\delta x_i}(\boldsymbol{u}^{(k)}) \right)^+ + 1.001 \left(\frac{\delta G_j}{\delta x_i}(\boldsymbol{u}^{(k)}) \right)^- + \frac{10^{-5}}{x_i^{max} - x_i^{min}} \right] \end{aligned} \tag{3.8}$$

Where

$$\begin{aligned} \left(\tfrac{\delta G_j}{\delta x_i}(\boldsymbol{u}^{(k)}) \right)^+ &= max\left\{ \tfrac{\delta G_j}{\delta x_i}(\boldsymbol{u}^{(k)}),\, 0 \right\} \\ \left(\tfrac{\delta G_j}{\delta x_i}(\boldsymbol{u}^{(k)}) \right)^- &= max\left\{ -\tfrac{\delta G_j}{\delta x_i}(\boldsymbol{u}^{(k)}),\, 0 \right\} \end{aligned} \tag{3.9}$$

In these equations the index i indicates the i$^{\text{th}}$ entry of the design vector, i.e. the i$^{\text{th}}$ design variable. It runs from 1 to N, where N is the total number of variables in the design vector. The index j describes the j$^{\text{th}}$ constraint function. The exact formulation applies also to the objective function. The index j runs from 1 to M, where M is the total number of constraints. Finally, the superscript k indicates the k$^{\text{th}}$ sub-problem, which is being solved. This will continue until all sub-problems are solved.

As one can see from Equation 3.7 to 3.9, the chosen convex approximation depends on the sign of the sensitivities. For positive values for the sensitivities, the first summation of Equation 3.7 is dominant. This term contains the upper bound U_i of the variable x_i. If the sensitivity becomes negative, the second summation will be dominant. In that case the second term will be used in the summation, which involves the lower bound L_i. The lower bound will always between $\boldsymbol{x}_{min}$ and $\boldsymbol{x}$, the upper bound will always be between $\boldsymbol{x}$ and $\boldsymbol{x}_{max}$.

The GCMMA algorithm updates the design vector based on the objective, constraints and their sensitivities. Hence, each iteration will have a different design vector (i.e. a different geometry) until the optimizer is converged. The optimizer is said to be converged when the Karush-Kuhn-Tucker (KKT) convergence criteria are met.

3.1.2. ADJOINT METHOD

Gradient-based optimizers make use of derivatives/sensitivities to search for the optimum. The derivatives can be determined both numerically and analytically. For very complicated derivatives doing this analytically could be hard if not impossible, in such cases numerical derivatives will be used. The disadvantage, however, is the increased computational effort required to calculate the derivatives compared to the analytical derivatives. Calculating the derivatives numerically can be done via the finite difference scheme, such as the forward difference, backward difference, and the central difference schemes [20]. The forward difference scheme is defined as:

$$f'(x) = \frac{f(x+h) - f(x)}{h} - \frac{f''(\xi)}{2!} h \tag{3.10}$$

The scheme makes use of the next function value $f(x+h)$ to calculate the derivative. Similarly, the backward difference scheme makes use of the previous function value $f(x-h)$, as shown in Equation 3.11.

$$f'(x) = \frac{f(x) - f(x-h)}{h} - \frac{f''(\xi)}{2!} h \tag{3.11}$$

Both these methods have a first order accuracy, which might not be sufficient for some applications. The central difference scheme on the other hand has a second order accuracy, as shown in Equation 3.12.

$$f'(x) = \frac{f(x+h) - f(x-h)}{2h} - \frac{f'''(\xi)}{3!} h^2 \tag{3.12}$$

Calculating the sensitivities analytically can be done directly or via the adjoint method [9]. Consider a function of the form:

$$G_j = f(\boldsymbol{u}(\boldsymbol{\rho}), \boldsymbol{\rho}) \tag{3.13}$$

Then the sensitivity will be:

$$\frac{dG_j}{d\rho_i} = \frac{\delta G_j(\boldsymbol{u}(\boldsymbol{\rho}), \boldsymbol{\rho})}{\delta \rho_i} + \frac{\delta G_j(\boldsymbol{u}(\boldsymbol{\rho}), \boldsymbol{\rho})}{\delta \boldsymbol{u}} \frac{d\boldsymbol{u}(\boldsymbol{\rho})}{d\rho_i} \tag{3.14}$$

In the direct method the term $d\boldsymbol{u}(\boldsymbol{\rho})/d\rho_i$ is obtained by differentiating the equilibrium equations. This requires an inverted stiffness matrix for every design variable. Inverting large matrices is computationally expensive, therefore it is preferred to reduce the required number of inverted matrices.

A different approach which prevents the calculation of $d\boldsymbol{u}(\boldsymbol{\rho})/d\rho_i$ and could therefore save computational time, is the adjoint method. In the adjoint method the residual force vector, multiplied with Lagrange multipliers, is added. Since the residual force vector is zero, the problem is not altered and the Lagrange multipliers can be chosen freely. The function can now be written as:

$$G_j = G_j(\boldsymbol{u}(\boldsymbol{\rho}), \boldsymbol{\rho}) + \boldsymbol{\lambda}_j^T \boldsymbol{R}(\boldsymbol{u}(\boldsymbol{\rho}), \boldsymbol{\rho}) \tag{3.15}$$

The sensitivity will be:

$$\frac{dG_j}{d\rho_i} = \frac{\delta G_j(\boldsymbol{u}(\boldsymbol{\rho}), \boldsymbol{\rho})}{\delta \rho_i} + \frac{\delta G_j(\boldsymbol{u}(\boldsymbol{\rho}), \boldsymbol{\rho})}{\delta \boldsymbol{u}} \frac{d\boldsymbol{u}(\boldsymbol{\rho})}{d\rho_i} + \boldsymbol{\lambda}_j^T \left(\frac{\partial \boldsymbol{R}(\boldsymbol{u}(\boldsymbol{\rho}), \boldsymbol{\rho})}{\partial \rho_i} + \frac{\partial \boldsymbol{R}(\boldsymbol{u}(\boldsymbol{\rho}), \boldsymbol{\rho})}{\partial \boldsymbol{u}} \frac{d\boldsymbol{u}(\boldsymbol{\rho})}{d\rho_i} \right) \tag{3.16}$$

Rewriting gives:

$$\frac{dG_j}{d\rho_i} = \left(\frac{\delta G_j(\boldsymbol{u}(\boldsymbol{\rho}), \boldsymbol{\rho})}{\delta \boldsymbol{u}} + \boldsymbol{\lambda}_j^T \frac{\partial \boldsymbol{R}(\boldsymbol{u}(\boldsymbol{\rho}), \boldsymbol{\rho})}{\partial \boldsymbol{u}} \right) \frac{d\boldsymbol{u}(\boldsymbol{\rho})}{d\rho_i} + \frac{\delta G_j(\boldsymbol{u}(\boldsymbol{\rho}), \boldsymbol{\rho})}{\delta \rho_i} + \boldsymbol{\lambda}_j^T \frac{\partial \boldsymbol{R}(\boldsymbol{u}(\boldsymbol{\rho}), \boldsymbol{\rho})}{\partial \rho_i} \tag{3.17}$$

Since the Lagrange multipliers could be chosen freely, they can be chosen such that the first term vanishes. As a result the term $d\boldsymbol{u}(\boldsymbol{\rho})/d\rho_i$ does not need to be calculated. Then the expression reduces to:

$$\frac{dG_j}{d\rho_i} = \frac{\delta G_j(\boldsymbol{u}(\boldsymbol{\rho}), \boldsymbol{\rho})}{\delta \rho_i} + \boldsymbol{\lambda}_j^T \frac{\partial \boldsymbol{R}(\boldsymbol{u}(\boldsymbol{\rho}), \boldsymbol{\rho})}{\partial \rho_i} \tag{3.18}$$

Where $\boldsymbol{\lambda}_j$ is obtained from:

$$\boldsymbol{\lambda}_j^T \frac{\partial \boldsymbol{R}(\boldsymbol{u}(\boldsymbol{\rho}), \boldsymbol{\rho})}{\partial \boldsymbol{u}} = -\frac{\delta G_j(\boldsymbol{u}(\boldsymbol{\rho}), \boldsymbol{\rho})}{\delta \boldsymbol{u}} \tag{3.19}$$

In the direct method one inverts the equilibrium equations N times, where N is the total number of variables. In the adjoint method the first step is to calculate $\boldsymbol{\lambda_j}$ M+1 times (including the objective), where M is the number of constraints. The calculation of the Lagrange multipliers requires also inverted matrices, as a consequence it is computationally less expensive to use the adjoint method if the design problem has more design variables than constraints. If the number of constraints is greater or equal to the number of variables, then the direct method is computationally less expense. The optimization problems solved for the morphing winglet there are much more elements (i.e. design variables) compared to the number of constraints defined. Therefore the adjoint method has been selected.

3.2. OPTIMIZATION STRATEGY

The optimization strategy is focused on designing and sizing a mechanism which is able to perform a specified motion without failure. This will be done by improving, extending, and expanding the previous tool. To understand where these research goals come from and how the current model meets these research goals, first the previous model will be covered briefly, then the areas of improvement will be identified, which result in the research goals. Finally, two optimization problems will be formulated. Here will be explained how the problem formulations meet the research goals.

3.2.1. PREVIOUS MODEL

The approach in the previous tool for the design of mechanisms is largely based on the approach Kawamoto took to design truss mechanisms. Kawamoto used in the non-linear finite element tool the LM-algorithm to solve the equilibrium equations. The objective function formulated was the least squares error between the intended trajectory and the actual trajectory of the mechanism. Hence the optimizer will try to find the mechanism that is best able to follow the trajectory, i.e. to minimize the error between the target and actual trajectory. To make sure no additional degrees of freedom are present (and the mechanism is able to carry a load), two additional load cases were formulated, each with a small disturbance force. By defining the objective function as a weighted sum of the three load cases, the mechanism that will follow the intended trajectory best, while not deviating from the trajectory due to the disturbance forces, will be the optimal solution. If additional degrees of freedom were present, the disturbance forces would result in a large deviation from the intended trajectory. Hence by including these two additional load cases no additional degrees of freedom, other than those required to perform the trajectory, will be present in the solution. The objective function can therefore be written as:

$$F_0 = \sum_{i=1}^{3} w_i D_i \tag{3.20}$$

The subscript i indicates the $\mathrm{i^{th}}$ load case, w_i are the weighting factors for each load case, and D_i is given by:

$$D_i = \left(u_x^{act} - u_x^{traj}\right)^2 + \left(u_y^{act} - u_y^{traj}\right)^2 \tag{3.21}$$

Here u_x^{act} and u_y^{act} represent the actual x- and y-displacement of the output node and u_x^{traj} and u_y^{traj} the intended displacements in x and y, respectively. In addition, multiple constraints were specified, including a volume constraint on the number of elements.

As mentioned at the beginning of this section, the previous tool is largely based on the on the approach described by Kawamoto. The tool uses the LM-algorithm as well. Similarly, the objective function is defined as the least squares error, with one small extension. The lease squares error is calculated at different instances of the trajectory and then summed. In this way the trajectory is checked throughout the entire path. The objective function used in the previous tool can be written as:

$$F_0 = \sum_{i=1}^{3} w_i \sum_{j=1}^{N_s} \left(u_x^{act} - u_x^{traj}\right)^2 + \left(u_y^{act} - u_y^{traj}\right)^2 \tag{3.22}$$

Here N_s represents the number of steps that the trajectory consists of. In addition, several constraints were formulated. One constraints was a volume constraints on the number of elements, the other constraints were related to the connectivity at the supports, input node, and output node. At the supports at least one member must be present, to make sure all supports are included in the final design. At the input and output nodes at least two elements must be present to be load carrying. The optimization problem was solved with the GCMMA algorithm, also using the adjoint method for the sensitivities. The optimizer often yielded a design vector with intermediate densities, where the elastic deformation of the members influenced the trajectory. Now, the 0/1 design depends on a couple of parameters, which include a penalization scheme, volume constraint and an applied force. Therefore, to improve the separation, the applied loading was incrementally increased, where for each load increment an additional optimization has to be performed.

Once a mechanism was found, a linear finite element analysis was performed to size the structure. For each step j in the trajectory a finite element analysis was performed to calculate the required cross-sectional areas of the elements to prevent material failure. Then for each member the largest cross-sectional area was selected to be conservative.

3.2.2. AREAS OF IMPROVEMENT

With the previous implementation of the tool, several improvements could be made, which could be categorized in robustness, computational time and separation (or 0/1 solution). Improving the robustness of the tool can be achieved by removing the incremental load. For a given load the optimizer will search in a particular direction for the minimum, however when the load is increased, the minimum could lie elsewhere. As a consequence the optimizer searches in a direction which later during the optimization no longer is a minimum. Changing its search direction is sometimes not possible since that would require a large increase in the objective. As a result the optimizer was unable to find a feasible solution. Hence the robustness could be improved by removing the incremental load.

An additional disadvantage of the incremental load is the increased computational time. For each load increment an optimization is performed. Another costly aspect of the previous tool is the formulation of the objective function. For each step j three analyses have to be performed, one for the trajectory and two additional ones to regulate the degrees of freedom. If this could be reduces to a single load case, the computational is reduced to approximately a third of the original computational time. Finally, more vector operations and additional preallocation of variables could save some time as well.

Another aspect area of improvement is limited separation that occurred. In the previous tool the majority of the runs resulted in intermediate densities, which are difficult to interpret and its elastic deformation might influence the motion of the mechanism. Improving the separation is therefore preferred.

Once these aspects are improved, the functionality of the tool could be extended. The previous tool for example is only compatible with a single input and single output node. The tool could be extended to handle multiple input and output nodes. Also, in the sizing step, only material failure was considered as a failure mode. An important failure mode is buckling, or the loss of stability. Both column buckling as well as global buckling can be included in the sizing step as well. These aspects could be implemented to extend the previous capabilities.

Finally, the previous tool is only compatible for 2D structures. Expanding the tool to 3D is another improvement, necessary for practical applications. All these improvements are considered the research goals for this thesis, which were already introduced in Chapter 1. The goals are summarized below.

1. Improve previous tool
    (a) Increase robustness
    (b) Reduce computational time
    (c) Increase separation
2. Extend previous tool
    (a) Include multiple input nodes
    (b) Include multiple output nodes
    (c) Include buckling
3. Expand previous tool
    (a) Expand to 3D

3.2.3. CURRENT MODEL

Designing and sizing a mechanism would ideally be done in a single optimization, but that is not possible for two reasons:

1. For the mechanism design, penalization was introduced to steer the design variables to 0 or 1. Sizing, on the other hand, tries to minimize the cross-sectional areas to be as light as possible, just to prevent failure. This would result in a design vector that has intermediate values for which the failure constraints are not accurate. Members with intermediate densities are penalized and will be able to carry less load that it actually could. Therefore once a failure constraint becomes active, this might not yet be active when the penalization was not applied. Due to the penalization the structure would be able to carry less load that it actually could.
2. The elements that need to be removed will have a density variable equal to ρ_{min}, as determined by the optimizer. These very small and slender members are only there in the model, but would be removed after post-processing. However, these members can hardly carry any load and would violate a stress or local buckling constraint, while in practice they would not exist.

Therefore, it has been decided to decouple the mechanism design and mechanism sizing. For the mechanism design an optimization will be performed, taking into account the research objectives as discussed in the previous section. The approach to design a mechanism is partially based on the approach Kawamoto took to design truss mechanisms [31] and partially based on the work done by Kim [35]. The mechanism sizing step has also been formulated as an optimization problem. In the previous tool the largest cross-sectional areas were selected from each step to be conservative. But by minimizing the weight with different failure modes as constraints, possible weight reductions could be achieved. The selected formulation which complies with the research goals for both the mechanism design and sizing will be covered here.

Mechanism Design

In the previous tool the least squares error will be minimized for the mechanism design. As a result the optimizer steers towards a solution which is able to perform the trajectory as good as possible. This objective function does not steer the solution towards a 0/1 design. A proper applied load and volume constraint in combination with penalization could overcome this, as was shown by Kawamoto [31]. However, Kawamoto had applied other optimizations to find out what the solution must be. Hence with this knowledge the optimization problem could be tailored. In general this information is not known a priori, therefore it was observed that with the previous objective function it was very difficult to obtain a 0/1 design.

The objective function selected is based on the objective function used by Kim [35]. The objective function was equivalent to the compliance. The minimization of the compliance yields the stiffest structure possible, given the constraints. Then with the trajectory specified as a constraint, the optimizer will search for the stiffest possible structure. Hence the optimizer actively steers towards a 0/1 design, thereby improving the separation. Another very important aspect of the compliance minimization is the regulation of the degrees of freedom. Having a mechanism which is able to follow the intended trajectory, then minimizing the compliance means a minimization of the displacements ($\boldsymbol{u}^{(L)}$) at the node(s) where the load is applied. If additional degrees of freedom would be present, then the displacements would be large. This, however, is prevented by the minimization of the displacements as a result of the compliance [35]. The objective function could then be written as:

$$F_0 = C = \boldsymbol{F}^T \boldsymbol{u}^{(L)} \tag{3.23}$$

However, it was observed that with the minimization of the compliance not always mechanisms were obtained, sometimes the elements were stretched to be able to perform the required motion. The compliance of those geometries was indeed smaller than mechanisms that were able to perform the trajectory without stretching elements. Therefore the reaction force at the input node (after step 1 of the finite element) was included as an additional term in the objective function. In the first step of the finite element analysis no loading was applied, hence the reaction force should be zero for mechanisms, and will be non-zero when there is no degree of freedom. Including the reaction force as an additional term yields the following objective function:

$$F_0 = C + \left(F^{input}\right)^2 \tag{3.24}$$

The term is squared to also minimize negative reaction forces in magnitude. Otherwise the optimizer would be able to find negative objective function values, due to the reaction force. This formulation is able to find a mechanism due to the reaction force term. The mechanism will also be as stiff as possible (i.e. 0/1 solution) due to compliance term $\boldsymbol{F}^T \boldsymbol{u}^{(L)}$. By having an objective function which promotes 0/1 designs and regulates the degrees of freedom automatically, there incremental load and additional load cases could be removed. This improves the robustness, separation and computational time. To include multiple input nodes, the objective function can be written as:

$$F_0 = C + \sum_{i=1}^{N_{in}} \left(F_i^{input}\right)^2 \tag{3.25}$$

Here N_{in} is the total number of actuations at the various input nodes. Assuming that at each actuation/input node only one degree of freedom has a prescribed displacement, then this number is also equal to the number of input nodes.

As mentioned earlier, the trajectory must be included as a constraint. In the post-processing section of the previous chapter the ratio $R^{trajectory}$ was introduced. For values smaller than 1, the mechanism is able to follow the specified trajectory. Note that for the ability to follow the specified trajectory the displacement vector $\boldsymbol{u}^{(NL)}$ is used. Using this displacement vector the applied loading will not influence the structure's ability to follow the specified trajectory. If the displacements after the applied loading were taken, then a different loading would mean a different trajectory the mechanism follows. This could mean a violation of the trajectory, which should be prevented. The trajectory constraint can be written as:

$$R^{trajectory} < 1 \tag{3.26}$$

Rewriting this in standard form gives:

$$G^{trajectory} = R^{trajectory} - 1 < 0 \tag{3.27}$$

To include multiple output nodes, for each node a trajectory constraint can be formulated. This gives:

$$G_j^{trajectory} = R_j^{trajectory} - 1 < 0 \quad j = 1, ..., N_{out} \tag{3.28}$$

Here, N_{out} is the total number of output nodes. Similarly, for the volume constraint the ratio should be smaller than 1 which yields:

$$G^{volume} = R^{volume} - 1 < 0 \tag{3.29}$$

However, due to the lower limit of ρ_{min} for the design variables, the constraint needs to be modified slightly. The volume will at least be equal to the total number of elements times ρ_{min}. Therefore, defining α_{max} as $(N_e - V_{max})\rho_{min}$, the constraint will be redefined as:

$$G^{volume} = \frac{V^{volume}}{V_{max} + \alpha_{max}} - 1 = R^{volume} - 1 < 0 \tag{3.30}$$

To prevent the optimizer to yield mechanisms without any element at the input node (thereby having no reaction force). The input node connectivity ratio should be larger than 1 to have at least the number of elements specified by V_{max} Rewriting this in standard form gives:

$$G^{input\ node} = 1 - R^{input\ node} < 0 \tag{3.31}$$

Similar to the volume constraint, the introduction of a lower bound of ρ_{min} has to be incorporated. Therefore α_{in} will be introduced. This will be equal to the number of elements at the input node minus the minimum number of elements ($C^{min}_{input\ node}$), then multiplied with ρ_{min}. The constraint will be redefined as:

$$G^{input\ node} = 1 - \frac{C_{input\ node}}{C^{min}_{input\ node} + \alpha_{in}} = 1 - R^{input\ node} < 0 \tag{3.32}$$

Finally, multiple input nodes can be included. Similar to the trajectory constraint, for each input node a constraint can be defined.

$$G_j^{input\ node} = 1 - R_j^{input\ node} < 0 \quad j = 1, ..., N_{in} \tag{3.33}$$

Combining all this gives the following optimization problem for mechanism design:

$$\begin{aligned} \underset{\rho}{min}\, F_0 &= C + \sum_{i=1}^{N_{in}} \left(F_i^{input}\right)^2 \\ s.t. &= \begin{cases} G_j^{trajectory} & = R_j^{trajectory} - 1 & < 0 & j = 1, ..., N_{out} \\ G^{volume} & = R^{volume} - 1 & < 0 & \\ G_j^{input\ node} & = 1 - R_j^{input\ node} & < 0 & j = 1, ..., N_{in} \\ 0 \le \rho_{min} & \le \rho_i & \le 1 & \end{cases} \end{aligned} \tag{3.34}$$

However, the actuation can be applied in a number of steps (N_s). This changes the optimization problem slightly, where now the average of these steps is taken as the objective function and the average of the trajectory steps. The constraints for the volume and input node connectivity do not change during the actuation steps, hence no average was taken. Then the optimization problem can finally be written as:

$$
\begin{aligned}
&\min_{\rho} F_0 = \frac{1}{N_s}\sum_{k=1}^{N_s}\left[C_k + \sum_{i=1}^{N_{in}}\left(F_{i,k}^{input}\right)^2\right] \\
&s.t. = \left\{\begin{array}{llll}
G_j^{trajectory} & = \frac{1}{N_s}\sum_{k=1}^{N_s}\left[R_{j,k}^{trajectory} - 1\right] & < 0 & j = 1,\ldots,N_{out} \\
G^{volume} & = R^{volume} - 1 & < 0 & \\
G_j^{input\ node} & = 1 - R_j^{input\ node} & < 0 & j = 1,\ldots,N_{in} \\
0 \leq \rho_{min} & \leq \rho_i & \leq 1 &
\end{array}\right.
\end{aligned}
\tag{3.35}
$$

Mechanism Sizing
The mechanism design yields a mechanism which is able to follow the specified trajectory. The elements, however, are not optimized for weight. So far only their required presence was determined. Hence in the sizing step the mechanism will be optimized for weight, while preventing failure as a result of the aerodynamic loading. The objective to be minimized is weight and can be written as:

$$F_0 = W = \rho^m \sum_{i=1}^{N_e} \rho_i A_0 l_i \tag{3.36}$$

Here ρ^m is the density of the material.

The failure modes taken into account are global buckling, material failure in tension, material failure in compression, and local buckling. Of these different failure modes only global buckling is specified for the entire structure, whereas the other three are specified for each element individually. Starting with the global buckling constraint, if the critical eigenvalue is greater than 1, no global buckling will occur. Hence the constraint can be written as:

$$G^{global\ buckling} = 1 - R^{global\ buckling} \tag{3.37}$$

Taking only the lowest buckling mode into account might result in mode jumping. The optimizer will prevent the lowest buckling mode to occur, but the second buckling mode could become critical. Therefore it has been decided to take the lowest three buckling modes into account. In addition, in every step the geometry has changed (due to the actuation). As a result, different buckling loads and possibly different buckling modes are encountered for each step. Therefore, for every step the lowest three buckling modes are taken into account during the sizing by specifying a constraint for each buckling mode:

$$G_j^{global\ buckling} = 1 - R_j^{global\ buckling} < 0 \quad j = 1,\ldots,N_{buckl} \times N_s \tag{3.38}$$

Here N_{buckl} is the number of buckling modes taken into account per step. Hence the total number of constraints for global buckling are the product of N_{buckl} and the number of steps N_s.

The next constraint would be material failure in tension, which would occur if the stress in the element exceeds the yield stress. For the ith element in the kth step the constraint would be:

$$G_{i,k}^{stress\ tension} = \frac{\sigma_{i,k}}{\sigma_y} - 1 < 0 \tag{3.39}$$

In contrast to the global buckling constraint, all stress constraints can be combined in a single Kreisselmeier-Steinhauser function [12]. This function will always be more strict than any of the constraints put into this function. Hence when this single function is satisfied, none of the constraints will be violated. The function is given by:

$$G = \frac{1}{K_s} ln\left(\sum_{j=1}^{N} e^{K_s G_j}\right) \tag{3.40}$$

Here K_s is a scaling parameter, the larger the value the closer the approximation of the actual constraints. Also, N represents the total number of constraints combined in the single constraint and G_j is the jth constraint. Applying this function of the stress constraints would give the following constraint for tension:

$$G^{stress\ tension} = \frac{1}{K_s} ln\left(\sum_{j=1}^{N_t} e^{K_s G_j^{stress\ tension}}\right) < 0 \tag{3.41}$$

Note that j represents a single combination of i and k. And N_t would be the product of the number of steps times the number of elements in the mechanism. For example, if the actuation is done in five steps and the mechanism consists of 4 elements, N_t would be equal to twenty.

Similarly, the compression constraint can be formulated, with the small difference that the stress is now negative. Here is assumed that the yield stress in compression is equal but opposite in sign to the yield stress in tension. It is assumed that the material yields at the same stress level in tension as it does in compression.

$$G_{i,k}^{stress\ compression} = -\frac{\sigma_{i,k}}{\sigma_y} - 1 < 0 \tag{3.42}$$

And the final stress constraint for compression would be:

$$G^{stress\ compression} = \frac{1}{K_s} ln\left(\sum_{j=1}^{N_c} e^{K_s G_j^{stress\ compression}}\right) < 0 \tag{3.43}$$

Here N_c is equal to N_t. The last constraint is local buckling, which is again specified for each element in each step. For the i$^{\text{th}}$ element and the k$^{\text{th}}$ step, the constraint would be written as:

$$G_{i,k}^{local\ buckling} = R_{i,k}^{local\ buckling} - 1 = \frac{\rho_i A_0 E_i \epsilon_{i,k}}{P_{i,k}^{cr}} - 1 < 0 \tag{3.44}$$

Or

$$G_{i,k}^{local\ buckling} = -\frac{4\epsilon_{i,k} l_i^2}{\rho_i \pi A_0} - 1 < 0 \tag{3.45}$$

Again, combining all these constraints into a single local buckling constraint would give:

$$G^{local\ buckling} = \frac{1}{K_s} ln\left(\sum_{j=1}^{N_{lb}} e^{K_s G_j^{local\ buckling}}\right) < 0 \tag{3.46}$$

Here the subscripts i and k are replaced by j. Also, N_{lb} is the number total number of local buckling constraints. This is also equal to N_t.

Now combining all this into a single optimization would give:

$$\begin{aligned} \min_{\rho} F_0 &= \rho^m \sum_{i=1}^{N_e} \rho_i A_0 l_i \\ s.t. &= \begin{cases} G_j^{global\ buckling} & < 0 \quad j = 1, ..., N_{buckl} \times N_s \\ G^{stress\ tension} & < 0 \\ G^{stress\ compression} & < 0 \\ G^{local\ buckling} & < 0 \\ 0 \le \rho_{min} \quad \le \rho_i & \le 1 \end{cases} \end{aligned} \tag{3.47}$$

3.3. MECHANISM DESIGN

In the previous section the problem formulation for mechanism design was introduced. This section will cover the problem formulation in more detail, elaborates on how the functions depend on the design variables, and derives the sensitivities of the objective function and constraints. First the objective function will be discussed, then the constraints, followed by the sensitivities, and finally the verification of the mechanism design is done. For simplicity a single actuation step is assumed here. If the actuation was done in multiple steps, then the average of the function values and sensitivities has to be taken.

3.3.1. OBJECTIVE

The objective function chosen for the mechanism design, assuming that the actuation is done in a single step, was:

$$F_0 = C + \sum_{i=1}^{N_{in}} \left(F_i^{input}\right)^2 \tag{3.48}$$

or

$$F_0 = \boldsymbol{F}^T \boldsymbol{u}^{(L)} + \sum_{i=1}^{N_{in}} \left(\boldsymbol{I}_i^{input} \boldsymbol{F}_{int}\right)^2 \tag{3.49}$$

In this equation $\boldsymbol{u}^{(L)}$ and $\boldsymbol{F}_{int}$ are a function of the design variables.

3.3.2. CONSTRAINTS

Several constraints are included in the optimization problem, these include the trajectory constraint, volume constraint, and input node connectivity constraint. Each of these constraints will be covered here.

TRAJECTORY CONSTRAINT

The trajectory constraint(s) can be written as:

$$G_j^{trajectory} = R_j^{trajectory} - 1 < 0 \quad j = 1, ..., N_{out} \tag{3.50}$$

or

$$G_j^{trajectory} = \frac{\Delta_j}{\Delta_j^{max}} - 1 < 0 \quad j = 1, ..., N_{out} \tag{3.51}$$

Where Δ_j (in 3D) was given by:

$$\Delta_j = \sqrt{\left(u_x^{act} - u_x^{traj}\right)^2 + \left(u_y^{act} - u_y^{traj}\right)^2 + \left(u_z^{act} - u_z^{traj}\right)^2} \tag{3.52}$$

The actual nodal locations (u_x^{act}, u_y^{act} and u_z^{act}) are entries of the displacement vector $\boldsymbol{u}^{(NL)}$. Hence these variables are a function of the design variables.

VOLUME CONSTRAINT

The volume constraint was defined as:

$$G^{volume} = R^{volume} - 1 < 0 \tag{3.53}$$

or

$$G^{volume} = \frac{V}{V_{max} + \alpha_{max}} - 1 < 0 \tag{3.54}$$

Here the volume of the structure is calculated by summing over the design variables, hence V_{max} is a function of ρ_i.

INPUT NODE CONNECTIVITY CONSTRAINT

The last constraint is the input node connectivity. This is a constraint on the number of elements attached to the input node(s). For each input node a constraint is specified of the form:

$$G^{input\ node} = 1 - R^{input\ node} < 0 \tag{3.55}$$

or

$$G^{input\ node} = 1 - \frac{C_{input\ node}}{C_{input\ node}^{min} + \alpha_{in}} < 0 \tag{3.56}$$

Each input node should have at least 2 elements attached to it to be able to transfer any load. Therefore, for each input node a value of 2 is used for the minimum number of elements $C_{input\ node}^{min}$.

$$G^{input\ node} = 1 - \frac{C_{input\ node}}{2+\alpha_{in}} < 0 \tag{3.57}$$

Here $C_{input\ node}$ is a function of the design variables.

3.3.3. SENSITIVITIES

In this section the sensitivities, using the adjoint method, are determined for the objective function as well as the constraints. First the objective will be covered, followed by the trajectory constraint(s), volume constraint, and input node connectivity constraint(s).

OBJECTIVE FUNCTION

The objective function consisted of two parts, one involving the compliance, the other involving the reaction forces. For a single-step actuation, the sensitivity can be written as:

$$\frac{dF_0}{d\rho_i} = \frac{d}{d\rho_i}\left(\boldsymbol{F}^T\boldsymbol{u}^{(L)}(\boldsymbol{\rho})\right) + \frac{d}{d\rho_i}\left(\sum_{i=1}^{N_{in}}\left(F_i^{input}\right)^2\right) \tag{3.58}$$

If the actuation is done in multiple steps, simply the average of these steps is taken as the objective function and its sensitivities. The two terms (compliance and reaction force) will be determined separately and added in the end. First, the sensitivity of the compliance term will be calculated.

Compliance

The adjoint method adds an additional term to the sensitivity, which is the product of unknown Lagrange multipliers and the residual force vector. This would not change the sensitivities, since the residual force vector is zero. However, by rearranging the terms, the computationally intensive term of the total derivative of the displacement with respect to the design variables is not necessary. Since the compliance calculation involves $\boldsymbol{u}^{(L)}$, the residual added should eliminate the sensitivities $d\boldsymbol{u}^{(L)}(\boldsymbol{\rho})/d\rho_i$. This will be achieved when adding the residual force vector from the linear (second) step of the finite element analysis. Hence the residual $\boldsymbol{R}^{(L)}$ will be added. Important to note is that this residual is a function of both $\boldsymbol{\rho}$ and $\boldsymbol{u}^{(NL)}(\boldsymbol{\rho})$.

$$\begin{aligned}
\frac{d}{d\rho_i}\left(\boldsymbol{F}^T\boldsymbol{u}^{(L)}(\boldsymbol{\rho})\right) &= \frac{d}{d\rho_i}\left(\boldsymbol{F}^T\boldsymbol{u}^{(L)}(\boldsymbol{\rho}) + \boldsymbol{\lambda}_1^T\left[\boldsymbol{R}^{(L)}(\boldsymbol{\rho},\boldsymbol{u}^{(NL)}(\boldsymbol{\rho}),\boldsymbol{u}^{(L)}(\boldsymbol{\rho}))\right]\right) \\
&= \frac{d}{d\rho_i}\left(\boldsymbol{F}^T\boldsymbol{u}^{(L)}(\boldsymbol{\rho}) + \boldsymbol{\lambda}_1^T\left[\boldsymbol{K}_t(\boldsymbol{\rho},\boldsymbol{u}^{(NL)}(\boldsymbol{\rho}))\boldsymbol{u}^{(L)}(\boldsymbol{\rho}) - \boldsymbol{F}\right]\right) \\
&= \frac{d}{d\rho_i}\left(\boldsymbol{F}^T\boldsymbol{u}^{(L)}(\boldsymbol{\rho})\right) + \boldsymbol{\lambda}_1^T\left[\frac{d}{d\rho_i}\left(\boldsymbol{K}_t(\boldsymbol{\rho},\boldsymbol{u}^{(NL)}(\boldsymbol{\rho}))\boldsymbol{u}^{(L)}(\boldsymbol{\rho})\right) - \frac{d}{d\rho_i}\boldsymbol{F}\right] \\
&= \boldsymbol{F}^T\frac{d}{d\rho_i}\left(\boldsymbol{u}^{(L)}(\boldsymbol{\rho})\right) + \boldsymbol{\lambda}_1^T\left[\frac{d\boldsymbol{K}_t(\boldsymbol{\rho},\boldsymbol{u}^{(NL)}(\boldsymbol{\rho}))}{d\rho_i}\boldsymbol{u}^{(L)}(\boldsymbol{\rho}) + \boldsymbol{K}_t(\boldsymbol{\rho},\boldsymbol{u}^{(NL)}(\boldsymbol{\rho}))\frac{d\boldsymbol{u}^{(L)}(\boldsymbol{\rho})}{d\rho_i}\right] \\
&= \boldsymbol{F}^T\frac{d\boldsymbol{u}^{(L)}(\boldsymbol{\rho})}{d\rho_i} + \boldsymbol{\lambda}_1^T\left[\frac{d\boldsymbol{K}_t(\boldsymbol{\rho},\boldsymbol{u}^{(NL)}(\boldsymbol{\rho}))}{d\rho_i}\boldsymbol{u}^{(L)}(\boldsymbol{\rho}) + \boldsymbol{K}_t(\boldsymbol{\rho},\boldsymbol{u}^{(NL)}(\boldsymbol{\rho}))\frac{d\boldsymbol{u}^{(L)}(\boldsymbol{\rho})}{d\rho_i}\right] \\
&= \left(\boldsymbol{F}^T + \boldsymbol{\lambda}_1^T\left[\boldsymbol{K}_t(\boldsymbol{\rho},\boldsymbol{u}^{(NL)}(\boldsymbol{\rho}))\right]\right)\frac{d\boldsymbol{u}^{(L)}(\boldsymbol{\rho})}{d\rho_i} + \boldsymbol{\lambda}_1^T\left[\frac{d\boldsymbol{K}_t(\boldsymbol{\rho},\boldsymbol{u}^{(NL)}(\boldsymbol{\rho}))}{d\rho_i}\boldsymbol{u}^{(L)}(\boldsymbol{\rho})\right]
\end{aligned} \tag{3.59}$$

Note that the tangent stiffness matrix evaluated for the non-linear displacement vector is called $\boldsymbol{K}_t$. This is done since the tangent stiffness matrix for both steps in the finite element analysis are the same. Now choose $\boldsymbol{\lambda}_1^T$ such that $\boldsymbol{F}^T + \boldsymbol{\lambda}_1^T\left[\boldsymbol{K}_t(\boldsymbol{\rho},\boldsymbol{u}^{(NL)}(\boldsymbol{\rho}))\right]$ becomes zero, thereby eliminating the need to calculate $d\boldsymbol{u}^{(L)}(\boldsymbol{\rho})/d\rho_i$. This yields the following expression for the sensitivity, taking the displacement vector out of the brackets.

$$\begin{aligned}
\frac{d}{d\rho_i}\left(\boldsymbol{F}^T\boldsymbol{u}^{(L)}(\boldsymbol{\rho})\right) &= \boldsymbol{\lambda}_1^T\left[\frac{d\boldsymbol{K}_t(\boldsymbol{\rho},\boldsymbol{u}^{(NL)}(\boldsymbol{\rho}))}{d\rho_i}\right]\boldsymbol{u}^{(L)}(\boldsymbol{\rho}) \\
&= \boldsymbol{\lambda}_1^T\left[\frac{\partial\boldsymbol{K}_t(\boldsymbol{\rho},\boldsymbol{u}^{(NL)}(\boldsymbol{\rho}))}{\partial\rho_i} + \frac{\partial\boldsymbol{K}_t(\boldsymbol{\rho},\boldsymbol{u}^{(NL)}(\boldsymbol{\rho}))}{\partial\boldsymbol{u}^{(NL)}(\boldsymbol{\rho}))}\frac{d\boldsymbol{u}^{(NL)}(\boldsymbol{\rho})}{d\rho_i}\right]\boldsymbol{u}^{(L)}(\boldsymbol{\rho})
\end{aligned} \tag{3.60}$$

To avoid evaluating $d\boldsymbol{u}^{(NL)}(\boldsymbol{\rho})/d\rho_i$, the adjoint technique will be applied again. This time the non-linear residual force vector will be added, the vector obtained from the first step of the finite element analysis.

$$\begin{aligned}
\frac{d\boldsymbol{u}^{(NL)}(\boldsymbol{\rho})}{d\rho_i} &= \frac{d\boldsymbol{u}^{(NL)}(\boldsymbol{\rho})}{d\rho_i} + \boldsymbol{\lambda}_2^T \frac{d\boldsymbol{R}^{(NL)}(\boldsymbol{\rho},\boldsymbol{u}^{(NL)}(\boldsymbol{\rho}))}{d\rho_i} \\
&= \frac{d\boldsymbol{u}^{(NL)}(\boldsymbol{\rho})}{d\rho_i} + \boldsymbol{\lambda}_2^T \left[\frac{\partial \boldsymbol{R}^{(NL)}(\boldsymbol{\rho},\boldsymbol{u}^{(NL)}(\boldsymbol{\rho}))}{\partial\rho_i} + \frac{\partial \boldsymbol{R}^{(NL)}(\boldsymbol{\rho},\boldsymbol{u}^{(NL)}(\boldsymbol{\rho}))}{\partial \boldsymbol{u}^{(NL)}(\boldsymbol{\rho})} \frac{d\boldsymbol{u}^{(NL)}(\boldsymbol{\rho})}{d\rho_i} \right] \\
&= \frac{d\boldsymbol{u}^{(NL)}(\boldsymbol{\rho})}{d\rho_i} + \boldsymbol{\lambda}_2^T \left[\frac{\partial \boldsymbol{R}^{(NL)}(\boldsymbol{\rho},\boldsymbol{u}^{(NL)}(\boldsymbol{\rho}))}{\partial\rho_i} + \boldsymbol{K}_t(\boldsymbol{\rho},\boldsymbol{u}^{(NL)}(\boldsymbol{\rho})) \frac{d\boldsymbol{u}^{(NL)}(\boldsymbol{\rho})}{d\rho_i} \right] \\
&= \left(\boldsymbol{I} + \boldsymbol{\lambda}_2^T \boldsymbol{K}_t(\boldsymbol{\rho},\boldsymbol{u}^{(NL)}(\boldsymbol{\rho}))\right) \frac{d\boldsymbol{u}^{(NL)}(\boldsymbol{\rho})}{d\rho_i} + \boldsymbol{\lambda}_2^T \left[\frac{\partial \boldsymbol{R}^{(NL)}(\boldsymbol{\rho},\boldsymbol{u}^{(NL)}(\boldsymbol{\rho}))}{\partial\rho_i} \right]
\end{aligned} \tag{3.61}$$

Now choose $\boldsymbol{\lambda}_2^T$ such that $\boldsymbol{I} + \boldsymbol{\lambda}_2^T \boldsymbol{K}_t(\boldsymbol{\rho},\boldsymbol{u}^{(NL)}(\boldsymbol{\rho}))$ becomes zero, thereby eliminating the need to calculate $d\boldsymbol{u}^{(NL)}(\boldsymbol{\rho})/d\rho_i$. This yields the following expression for the sensitivity.

$$\frac{d\boldsymbol{u}^{(NL)}(\boldsymbol{\rho})}{d\rho_i} = \boldsymbol{\lambda}_2^T \left[\frac{\partial \boldsymbol{R}^{(NL)}(\boldsymbol{\rho},\boldsymbol{u}^{(NL)}(\boldsymbol{\rho}))}{\partial\rho_i} \right] \tag{3.62}$$

Recall from Chapter 2 the expressions for the residual force vector and tangent stiffness matrix, which are repeated below and evaluated for $\boldsymbol{u}^{(NL)}$.

$$\boldsymbol{R}^{(NL)} = \sum_{i=1}^{N_e} A_i E_i l_i \left(\frac{1}{l^2} \boldsymbol{b}_i^T \boldsymbol{u}^{(NL)} + \frac{1}{2l^2} \left(\boldsymbol{u}^{(NL)}\right)^T \tilde{\boldsymbol{B}} \boldsymbol{u}^{(NL)} \right) \left(\frac{1}{l_i^2} \boldsymbol{b}_i^T + \frac{1}{l_i^2} \left(\boldsymbol{u}^{(NL)}\right)^T \tilde{\boldsymbol{B}}_i \right) - \boldsymbol{p}^T \tag{3.63}$$

$$\begin{aligned}
\boldsymbol{K}_t = \sum_{i=1}^{N_e} & A_i E_i l_i \\
\times & \left[\left(\frac{1}{l_i^2} \boldsymbol{b}_i^T + \frac{1}{l_i^2} \left(\boldsymbol{u}^{(NL)}\right)^T \tilde{\boldsymbol{B}}_i \right)^T \left(\frac{1}{l_i^2} \boldsymbol{b}_i^T + \frac{1}{l_i^2} \left(\boldsymbol{u}^{(NL)}\right)^T \tilde{\boldsymbol{B}}_i \right) \right. \\
+ & \left. \left(\frac{1}{l^2} \boldsymbol{b}_i^T \boldsymbol{u}^{(NL)} + \frac{1}{2l^2} \left(\boldsymbol{u}^{(NL)}\right)^T \tilde{\boldsymbol{B}} \boldsymbol{u}^{(NL)} \right) \left(\frac{1}{l_i^2} \tilde{\boldsymbol{B}}_i \right) \right]
\end{aligned} \tag{3.64}$$

As mentioned at the beginning of this chapter, all cross-sectional areas are penalized with the SIMP interpolation scheme. Substituting this into the expressions for the residual force vector and tangent stiffness matrix and simplifying the expressions give:

$$\boldsymbol{R}^{(NL)} = \sum_{i=1}^{N_e} \frac{\rho^p A_{max} E_i}{l_i^3} \left(\boldsymbol{b}_i^T \boldsymbol{u}^{(NL)} + \frac{1}{2} \left(\boldsymbol{u}^{(NL)}\right)^T \tilde{\boldsymbol{B}} \boldsymbol{u}^{(NL)} \right) \left(\boldsymbol{b}_i^T + \left(\boldsymbol{u}^{(NL)}\right)^T \tilde{\boldsymbol{B}}_i \right) - \boldsymbol{p}^T \tag{3.65}$$

$$\boldsymbol{K}_t = \sum_{i=1}^{N_e} \frac{\rho^p A_{max} E_i}{l_i^3} \left[\left(\boldsymbol{b}_i^T + \left(\boldsymbol{u}^{(NL)}\right)^T \tilde{\boldsymbol{B}}_i \right)^T \left(\boldsymbol{b}_i^T + \left(\boldsymbol{u}^{(NL)}\right)^T \tilde{\boldsymbol{B}}_i \right) + \left(\boldsymbol{b}_i^T \boldsymbol{u}^{(NL)} + \frac{1}{2} \left(\boldsymbol{u}^{(NL)}\right)^T \tilde{\boldsymbol{B}} \boldsymbol{u}^{(NL)} \right) \left(\tilde{\boldsymbol{B}}_i \right) \right] \tag{3.66}$$

Calculating the remaining derivatives:

$$\frac{\partial \boldsymbol{R}^{(NL)}}{\partial\rho_i} = \frac{p\rho_i^{p-1} A_{max} E_i}{l_i^3} \left(\boldsymbol{b}_i^T \boldsymbol{u}^{(NL)} + \frac{1}{2} \left(\boldsymbol{u}^{(NL)}\right)^T \tilde{\boldsymbol{B}} \boldsymbol{u}^{(NL)} \right) \left(\boldsymbol{b}_i^T + \left(\boldsymbol{u}^{(NL)}\right)^T \tilde{\boldsymbol{B}}_i \right) - \boldsymbol{p}^T \tag{3.67}$$

$$\frac{\partial \boldsymbol{K}_t}{\partial\rho_i} = \frac{p\rho^{p-1} A_{max} E_i}{l_i^3} \left(\boldsymbol{b}_i^T + \left(\boldsymbol{u}^{(NL)}\right)^T \tilde{\boldsymbol{B}}_i \right)^T \left(\boldsymbol{b}_i^T + \left(\boldsymbol{u}^{(NL)}\right)^T \tilde{\boldsymbol{B}}_i \right) + \left(\boldsymbol{b}_i^T \boldsymbol{u}^{(NL)} + \frac{1}{2} \left(\boldsymbol{u}^{(NL)}\right)^T \tilde{\boldsymbol{B}} \boldsymbol{u}^{(NL)} \right) \left(\tilde{\boldsymbol{B}}_i \right) \tag{3.68}$$

$$
\begin{aligned}
\frac{\partial \boldsymbol{K}_t}{\partial \boldsymbol{u}^{(NL)}} \frac{d\boldsymbol{u}^{(NL)}}{d\rho_i} &= \sum_{j=1}^{N_d} \frac{\partial \boldsymbol{K}_t}{\partial u_j^{(NL)}} \frac{d u_j^{(NL)}}{d\rho_i} \\
&= \sum_{j=1}^{N_d} \frac{\partial \boldsymbol{K}_t}{\partial u_j^{(NL)}} \frac{d\boldsymbol{u}^{(NL)}(j)}{d\rho_i} \\
&= \sum_{j=1}^{N_d} \sum_{i=1}^{N_e} \frac{\rho^p A_{max} E_i}{l_i^3} \\
&\quad \times \left[\left(\boldsymbol{I}_j^T \tilde{\boldsymbol{B}}_i \right)^T \left(\boldsymbol{b}_i^T + \left(\boldsymbol{u}^{(NL)} \right)^T \tilde{\boldsymbol{B}}_i \right) + \left(\boldsymbol{b}_i^T + \left(\boldsymbol{u}^{(NL)} \right)^T \tilde{\boldsymbol{B}}_i \right)^T \left(\boldsymbol{I}_j^T \tilde{\boldsymbol{B}}_i \right) \right. \\
&\quad \left. + \left(\boldsymbol{b}_i^T \boldsymbol{I}_j + \frac{1}{2} \left(\boldsymbol{I}_j^T \tilde{\boldsymbol{B}} \boldsymbol{u}^{(NL)} + \left(\boldsymbol{u}^{(NL)} \right)^T \tilde{\boldsymbol{B}} \boldsymbol{I}_j \right) \right) \left(\tilde{\boldsymbol{B}}_i \right) \right] \frac{d\boldsymbol{u}^{(NL)}(j)}{d\rho_i}
\end{aligned}
\tag{3.69}
$$

The partial derivative of the tangent stiffness matrix with respect to the displacement vector would be a 3D matrix, multiplying this with the second term reduces it to a matrix. Note that j runs from 1 to the number of free DOF. To summarize, the final sensitivity of the compliance term is given by:

$$
\frac{d}{d\rho_i} \left(\boldsymbol{F}^T \boldsymbol{u}^{(L)}(\boldsymbol{\rho}) \right) = \boldsymbol{\lambda}_1^T \left[\frac{\partial \boldsymbol{K}_t(\boldsymbol{\rho}, \boldsymbol{u}^{(NL)}(\boldsymbol{\rho}))}{\partial \rho_i} + \frac{\partial \boldsymbol{K}_t(\boldsymbol{\rho}, \boldsymbol{u}^{(NL)}(\boldsymbol{\rho}))}{\partial \boldsymbol{u}^{(NL)}(\boldsymbol{\rho}))} \frac{d\boldsymbol{u}^{(NL)}(\boldsymbol{\rho})}{d\rho_i} \right] \boldsymbol{u}^{(L)}(\boldsymbol{\rho}) \tag{3.70}
$$

Where the three derivative terms are given by the Equations 3.62, 3.68, and 3.69.

Reaction force

As mentioned earlier the internal force vector in the first step is used in the formulation of the reaction force term. The internal force vector $\boldsymbol{F}_{int}$, defined in the previous chapter, is a function of $\boldsymbol{\rho}$ and $\boldsymbol{u}^{(NL)}(\boldsymbol{\rho})$. Hence the non-linear residual force vector will be added for the adjoint approach. Also, there has been made use of the following rule, where the order (summation versus derivative) has been interchanged.

$$
\frac{d}{d\rho_i} \sum_{i=1}^{N_{in}} \left(\boldsymbol{I}_i^{input} \boldsymbol{F}_{int}(\boldsymbol{\rho}, \boldsymbol{u}^{(NL)}(\boldsymbol{\rho})) \right)^2 = \sum_{i=1}^{N_{in}} \frac{d}{d\rho_i} \left(\boldsymbol{I}_i^{input} \boldsymbol{F}_{int}(\boldsymbol{\rho}, \boldsymbol{u}^{(NL)}(\boldsymbol{\rho})) \right)^2 \tag{3.71}
$$

Now for a single reaction force i the sensitivity will be determined. Then summing those individual sensitivities will yield the sensitivity of all the reaction forces.

$$
\begin{aligned}
\frac{d}{d\rho_i} \left(\boldsymbol{I}_i^{input} \boldsymbol{F}_{int}(\boldsymbol{\rho}, \boldsymbol{u}^{(NL)}(\boldsymbol{\rho})) \right)^2 &= \frac{d}{d\rho_i} \left(\boldsymbol{I}_i^{input} \boldsymbol{F}_{int} \right)^2 + \boldsymbol{\lambda_3}^T \frac{d}{d\rho_i} \left(\boldsymbol{R}^{(NL)}(\boldsymbol{\rho}, \boldsymbol{u}^{(NL)}(\boldsymbol{\rho})) \right) \\
&= 2 \left(\boldsymbol{I}_i^{input} \boldsymbol{F}_{int} \right) \boldsymbol{I}_i^{input} \frac{d\boldsymbol{F}_{int}(\boldsymbol{\rho}, \boldsymbol{u}^{(NL)}(\boldsymbol{\rho}))}{d\rho_i} \\
&\quad + \boldsymbol{\lambda_3}^T \frac{d}{d\rho_i} \left(\boldsymbol{R}^{(NL)}(\boldsymbol{\rho}, \boldsymbol{u}^{(NL)}(\boldsymbol{\rho})) \right)
\end{aligned}
\tag{3.72}
$$

Note that the residual force vector added $\boldsymbol{R}^{(NL)}$ has been used in the sensitivity calculation for the compliance as well. Hence the derivatives of the residual force vector do not have to be recalculated. Also, the dependencies will be removed for clarity.

$$\begin{aligned}
\frac{d}{d\rho_i}\left(\boldsymbol{I}_i^{input}\boldsymbol{F}_{int}\right)^2 &= 2\left(\boldsymbol{I}_i^{input}\boldsymbol{F}_{int}\right)\boldsymbol{I}_i^{input}\frac{d\boldsymbol{F}_{int}}{d\rho_i}+\boldsymbol{\lambda_3}^T\frac{d}{d\rho_i}\left(\boldsymbol{R}^{(NL)}\right)\\
&= 2F_i^{input}\boldsymbol{I}_i^{input}\left(\frac{\partial\boldsymbol{F}_{int}}{\partial\rho_i}+\frac{\partial\boldsymbol{F}_{int}}{\partial\boldsymbol{u}^{(NL)}}\frac{d\boldsymbol{u}^{(NL)}}{d\rho_i}\right)\\
&\quad+\boldsymbol{\lambda_3}^T\left(\frac{\partial\boldsymbol{R}^{(NL)}}{\partial\rho_i}+\frac{\partial\boldsymbol{R}^{(NL)}}{\partial\boldsymbol{u}^{(NL)}}\frac{d\boldsymbol{u}^{(NL)}}{d\rho_i}\right)\\
&= \left(2F_i^{input}\boldsymbol{I}_i^{input}\frac{\partial\boldsymbol{F}_{int}}{\partial\boldsymbol{u}^{(NL)}}+\boldsymbol{\lambda_3}^T\frac{\partial\boldsymbol{R}^{(NL)}}{\partial\boldsymbol{u}^{(NL)}}\right)\frac{d\boldsymbol{u}^{(NL)}}{d\rho_i}\\
&\quad+2F_i^{input}\boldsymbol{I}_i^{input}\frac{\partial\boldsymbol{F}_{int}}{\partial\rho_i}+\boldsymbol{\lambda_3}^T\frac{\partial\boldsymbol{R}^{(NL)}}{\partial\rho_i}
\end{aligned} \tag{3.73}$$

Similarly, choose $\boldsymbol{\lambda}_3$ such that the first term will disappear. This results in solving the following equation for $\boldsymbol{\lambda}_3$:

$$\left(2F_i^{input}\boldsymbol{I}_i^{input}\frac{\partial\boldsymbol{F}_{int}}{\partial\boldsymbol{u}^{(NL)}}+\boldsymbol{\lambda_3}^T\boldsymbol{K}_t\right)=0 \tag{3.74}$$

Here is made use of the fact that the partial derivative of the residual force vector with respect to the displacements gives the tangent stiffness matrix. The sensitivity can be written as:

$$\frac{d}{d\rho_i}\left(\boldsymbol{I}_i^{input}\boldsymbol{F}_{int}\right)^2 = 2F_i^{input}\boldsymbol{I}_i^{input}\frac{\partial\boldsymbol{F}_{int}}{\partial\rho_i}+\boldsymbol{\lambda_3}^T\frac{\partial\boldsymbol{R}^{(NL)}}{\partial\rho_i} \tag{3.75}$$

The partial derivative of the residual force vector has been determined previously. Hence the term $\dfrac{\partial\boldsymbol{F}_{int}}{\partial\rho_i}$ remains to be determined. Recall from Chapter 2 the expression for the internal force vector $\boldsymbol{F}_{int}$:

$$\boldsymbol{F}_{int}=\sum_{i=1}^{N_e}A_iE_il_i\left(\frac{1}{l^2}\boldsymbol{b}_i^T\boldsymbol{u}+\frac{1}{2l^2}\boldsymbol{u}^T\tilde{\boldsymbol{B}}\boldsymbol{u}\right)\left(\frac{1}{l_i^2}\boldsymbol{b}_i^T+\frac{1}{l_i^2}\boldsymbol{u}^T\tilde{\boldsymbol{B}}_i\right) \tag{3.76}$$

Realizing that $A_i=\rho_i^pA_0$, gives the following expression for the sensitivity:

$$\frac{\partial\boldsymbol{F}_{int}}{\partial\rho_i}=p\rho_i^{p-1}A_0E_il_i\left(\frac{1}{l^2}\boldsymbol{b}_i^T\boldsymbol{u}+\frac{1}{2l^2}\boldsymbol{u}^T\tilde{\boldsymbol{B}}\boldsymbol{u}\right)\left(\frac{1}{l_i^2}\boldsymbol{b}_i^T+\frac{1}{l_i^2}\boldsymbol{u}^T\tilde{\boldsymbol{B}}_i\right) \tag{3.77}$$

Substituting this expression yields the final expression for the sensitivity:

$$\begin{aligned}
\frac{d}{d\rho_i}\left(\boldsymbol{I}_i^{input}\boldsymbol{F}_{int}\right)^2 &= 2F_i^{input}\boldsymbol{I}_i^{input}p\rho_i^{p-1}A_0E_il_i\left(\tfrac{1}{l^2}\boldsymbol{b}_i^T\boldsymbol{u}+\tfrac{1}{2l^2}\boldsymbol{u}^T\tilde{\boldsymbol{B}}\boldsymbol{u}\right)\left(\frac{1}{l_i^2}\boldsymbol{b}_i^T+\frac{1}{l_i^2}\boldsymbol{u}^T\tilde{\boldsymbol{B}}_i\right)\\
&\quad+\boldsymbol{\lambda_3}^T\frac{\partial\boldsymbol{R}^{(NL)}}{\partial\rho_i}
\end{aligned} \tag{3.78}$$

Finally, the sensitivities of the entire objective function F_0 can be calculated. This can be obtained by summing the expression for the compliance sensitivity (equation 3.70) and the sensitivity of the reaction force for each prescribed displacement (equation 3.78).

TRAJECTORY CONSTRAINT

For the calculation of the trajectory sensitivities, the subscript j has been left out for clarity. As mentioned earlier for every output node j a trajectory constraint will be specified. Hence the displacements shown here, are those for the jth output node. Also, the trajectory constraint was specified before the loading was applied. Hence the displacements in the constraint are those obtained from $\boldsymbol{u}^{(NL)}$. As a result, the residual force vector $\boldsymbol{R}^{(NL)}$ is used in the adjoint sensitivity analysis. One final note, the Lagrange multipliers are collected in the vector $\boldsymbol{\lambda}_4$.

$$
\begin{aligned}
\frac{dG^{trajectory}}{d\rho_i} &= \frac{1}{\Delta_{max}}\frac{d}{d\rho_i}\left(\sqrt{((\boldsymbol{u}^{(NL)})^T\boldsymbol{I}_x - u_x^{traj})^2 + ((\boldsymbol{u}^{(NL)})^T\boldsymbol{I}_y - u_y^{traj})^2} - 1\right) \\
&+\boldsymbol{\lambda}_4^T\frac{d\boldsymbol{R}^{(NL)}}{d\rho_i} \\
&= \frac{1}{\Delta_{max}}\frac{d}{d\rho_i}\left(\sqrt{((\boldsymbol{u}^{(NL)})^T\boldsymbol{I}_x - u_x^{traj})^2 + ((\boldsymbol{u}^{(NL)})^T\boldsymbol{I}_y - u_y^{traj})^2}\right) \\
&+\boldsymbol{\lambda}_4^T\frac{d\boldsymbol{R}^{(NL)}}{d\rho_i} \\
&= \frac{1}{\Delta_{max}}\frac{2((\boldsymbol{u}^{(NL)})^T\boldsymbol{I}_x - u_x^{traj})\boldsymbol{I}_x + 2((\boldsymbol{u}^{(NL)})^T\boldsymbol{I}_y - u_y^{traj})\boldsymbol{I}_y}{2\sqrt{((\boldsymbol{u}^{(NL)})^T\boldsymbol{I}_x - u_x^{traj})^2 + ((\boldsymbol{u}^{(NL)})^T\boldsymbol{I}_y - u_y^{traj})^2}}\frac{d\boldsymbol{u}^{(NL)}}{d\rho_i} \\
&+\boldsymbol{\lambda_4}^T\left(\frac{\partial\boldsymbol{R}^{(NL)}}{\partial\rho_i} + \frac{\partial\boldsymbol{R}^{(NL)}}{\partial\boldsymbol{u}^{(NL)}}\frac{d\boldsymbol{u}^{(NL)}}{d\rho_i}\right) \\
&= \frac{1}{\Delta_{max}}\frac{(u_x^{act} - u_x^{traj})\boldsymbol{I}_x + (u_y^{act} - u_y^{traj})\boldsymbol{I}_y}{\sqrt{(u_x^{act} - u_x^{traj})^2 + (u_y^{act} - u_y^{traj})^2}}\frac{d\boldsymbol{u}^{(NL)}}{d\rho_i} \\
&+\boldsymbol{\lambda_4}^T\left(\frac{\partial\boldsymbol{R}^{(NL)}}{\partial\rho_i} + \frac{\partial\boldsymbol{R}^{(NL)}}{\partial\boldsymbol{u}^{(NL)}}\frac{d\boldsymbol{u}^{(NL)}}{d\rho_i}\right) \\
&= \left(\frac{1}{\Delta_{max}}\frac{(u_x^{act} - u_x^{traj})\boldsymbol{I}_x + (u_y^{act} - u_y^{traj})\boldsymbol{I}_y}{\sqrt{(u_x^{act} - u_x^{traj})^2 + (u_y^{act} - u_y^{traj})^2}} + \boldsymbol{\lambda_4}^T\frac{\partial\boldsymbol{R}^{(NL)}}{\partial\boldsymbol{u}^{(NL)}}\right)\frac{d\boldsymbol{u}^{(NL)}}{d\rho_i} \\
&+\boldsymbol{\lambda_4}^T\left(\frac{\partial\boldsymbol{R}^{(NL)}}{\partial\rho_i}\right) \\
&= \boldsymbol{\lambda_4}^T\left(\frac{\partial\boldsymbol{R}^{(NL)}}{\partial\rho_i}\right)
\end{aligned}
\tag{3.79}
$$

In the derivation $\boldsymbol{I}_x$ and $\boldsymbol{I}_y$ are vectors that contain zeros at every entry except for one, which corresponds to the entry of the output node. This entry contains the value 1. Also, for simplicity the sensitivity was shown only in 2D, but the exact same approach holds for 3D. Only a third term of the z-direction will be included as well.

The partial derivative of the non-linear residual force vector is given by equation 3.67. The Lagrange multipliers $\boldsymbol{\lambda}_4$ are obtained from equation 3.80.

$$
\frac{1}{\Delta_{max}}\frac{(u_x^{act} - u_x^{traj})\boldsymbol{I}_x + (u_y^{act} - u_y^{traj})\boldsymbol{I}_y}{\sqrt{(u_x^{act} - u_x^{traj})^2 + (u_y^{act} - u_y^{traj})^2}} + \boldsymbol{\lambda_4}^T\frac{\partial\boldsymbol{R}^{(NL)}}{\partial\boldsymbol{u}^{(NL)}} = 0 \tag{3.80}
$$

VOLUME CONSTRAINT

The sensitivity of the volume constraint can directly be determined and is equal to:

$$
\begin{aligned}
\frac{dG^{volume}}{d\rho_i} &= \frac{d}{d\rho_i}\left(\frac{V}{V_{max}+\alpha_{max}}-1\right) \\
&= \frac{d}{d\rho_i}\left(\frac{\sum_{i}^{N_e}\rho_i}{V_{max}+\alpha_{max}}-1\right) \\
&= \frac{1}{V_{max}+\alpha_{max}}
\end{aligned}
\tag{3.81}
$$

INPUT NODE CONNECTIVITY CONSTRAINT

As mentioned earlier the minimum number of elements $C^{min}_{input\ node}$ was set to 2. Therefore, the final sensitivity is given by:

$$
\frac{dG_j^{input\ node}}{d\rho_i} = \begin{cases} \dfrac{-1}{2+\alpha_{in}} & \text{if } i \in input \\ 0 & \text{otherwise} \end{cases}
\tag{3.82}
$$

Here the set $input$ contains the elements which are attached to the input node j. The sensitivity is only non-zero if the element is attached to the input node. Then it is equal to $-1/(2+\alpha_{in})$.

Finally, all the analytical sensitivities calculated were compared to the sensitivities obtained from central differences. The sensitivities were found to be the same. Hence the sensitivities were verified.

3.3.4. VERIFICATION

The problem formulation for the mechanism design should be able to find black-and-white mechanisms which follow a specific trajectory. Whether the tool is indeed able to find black-and-white mechanisms with a specified trajectory will be verified with a mechanism found by Kawamoto [30]. In his PhD Kawamoto also considered the design of articulated truss mechanisms. He considered a problem formulation illustrated in Figure 3.2a. On two nodes a displacement was prescribed and the objective was to find the mechanism where the output node (node 11 in the figure) displaces as much as possible to the right. Via brute force the optimal solution for this 2D problem was found to be the mechanism shown in Figure 3.2b.

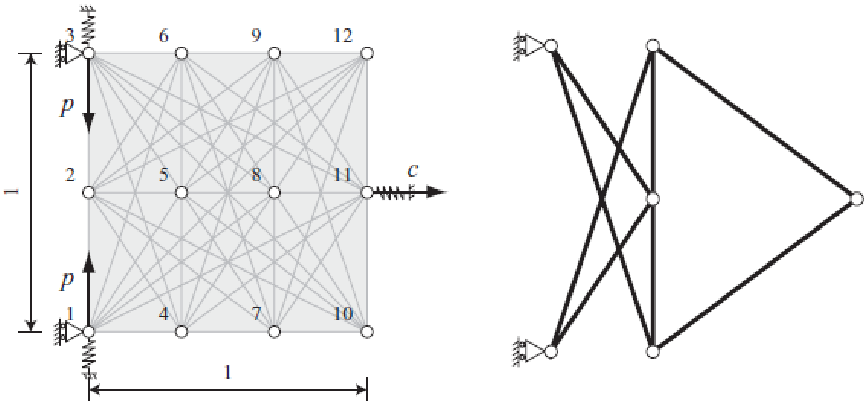

(a) Truss ground-structure for benchmark problem (initial geometry)

(b) Optimal solution for the benckmark problem (final geometry)

Figure 3.2: Scissors benchmark problem and solution by Kawamoto [30]

The kinematics is a result of the relative cross-sectional areas. The actual values of the areas are not relevant. The optimizer will steer towards either ρ_{min} or the upper bound, whether this is set to 0.1, 1 or 2 does not change the mechanisms found. Members with an area equal to ρ_{min} can be removed, whereas elements with significant cross-sectional areas (ideally all equal to the upper bound) cannot be removed without changing its kinematics. The upper bound has conveniently set to 1, just like Kawamoto did. Also the value of the Young's modulus does not influence the mechanisms found, therefore it has been set to 10 (just like Kawamoto did). Also the same size for the ground-structure was used, with dimensions 1-by-1.

On the input nodes a prescribed displacement of 0.5 was enforced, for node 1 an upward displacement and for node 3 a downwards displacement. In addition, on the output node a trajectory was specified which coincided with the displacement of the node for mechanism shown in Figure 3.2b. This means that the geometry has two input nodes and a single output node. In addition, the actuation has been done in 5 steps, hence the optimization problem can be written as:

$$\begin{aligned} \min_{\rho} F_0 &= \frac{1}{5}\sum_{k=1}^{5}\left[C_k + \sum_{i=1}^{2}\left(F_{i,k}^{input}\right)^2\right] \\ s.t. &= \left\{\begin{array}{lll} G^{trajectory} & = \frac{1}{5}\sum_{k=1}^{5}\left[R_k^{trajectory}-1\right] & < 0 \\ G^{volume} & = R^{volume}-1 & < 0 \\ G_1^{input\ node} & = 1-R_1^{input\ node} & < 0 \\ G_2^{input\ node} & = 1-R_2^{input\ node} & < 0 \\ 0 \leq \rho_{min} & \leq \rho_i & \leq 1 \end{array}\right. \end{aligned} \tag{3.83}$$

Running the simulation, for a strict trajectory constraint with Δ_{max} chosen to be 0.01. The mechanism found in the optimization was exactly the same mechanism (scissors) Kawamoto found, as can be seen in Figure 3.3. Op top the converged solution is shown, where all elements are included, below the post-processed geometry is shown. Here the elements with ρ_{min} are removed.

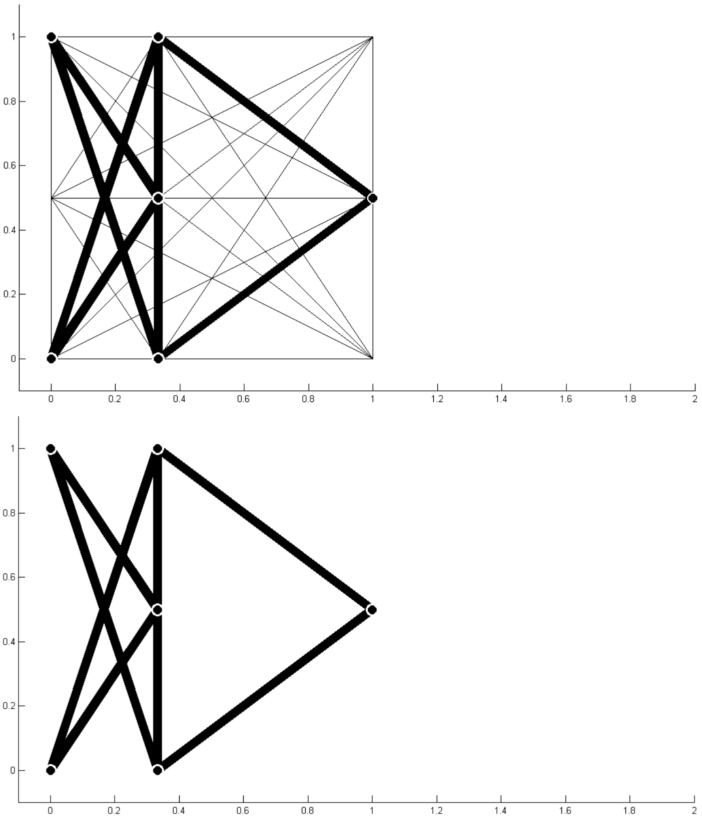

Figure 3.3: Topology of the scissors before post-processing (top) and after post-processing (bottom)

The corresponding optimization history is shown in Figure 3.4 for a random input vector. In blue the objective function is shown, which was converged after approximately 140 iterations. In red the trajectory constraint was shown. The original geometry was indeed not able to follow the specified trajectory and the constraint was violated at the start. Then, in green the volume constraint is shown. Finally, in pink the connectivity for first input node (the lower input node) and in yellow the connectivity for second input node 2 (the upper input node) was shown. In the optimized result all constraints are satisfied. It must be noted that all function values were normalized with the maximum value for the objective function (which for this optimization was the starting geometry). Hence the objective starts at the value 1.

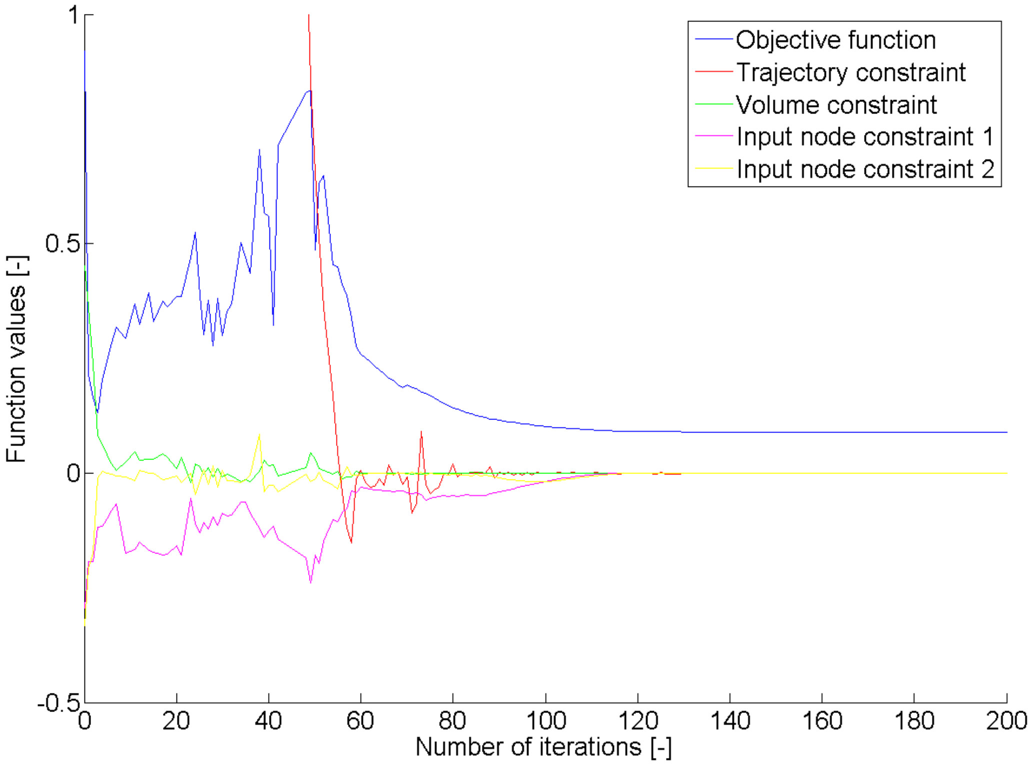

Figure 3.4: Optimization history of the mechanism design for the scissors

Finally, in Figure 3.5 the actuation of the mechanism is illustrated. This is done for 5 steps in the actuation process, both before and after the post-processing.

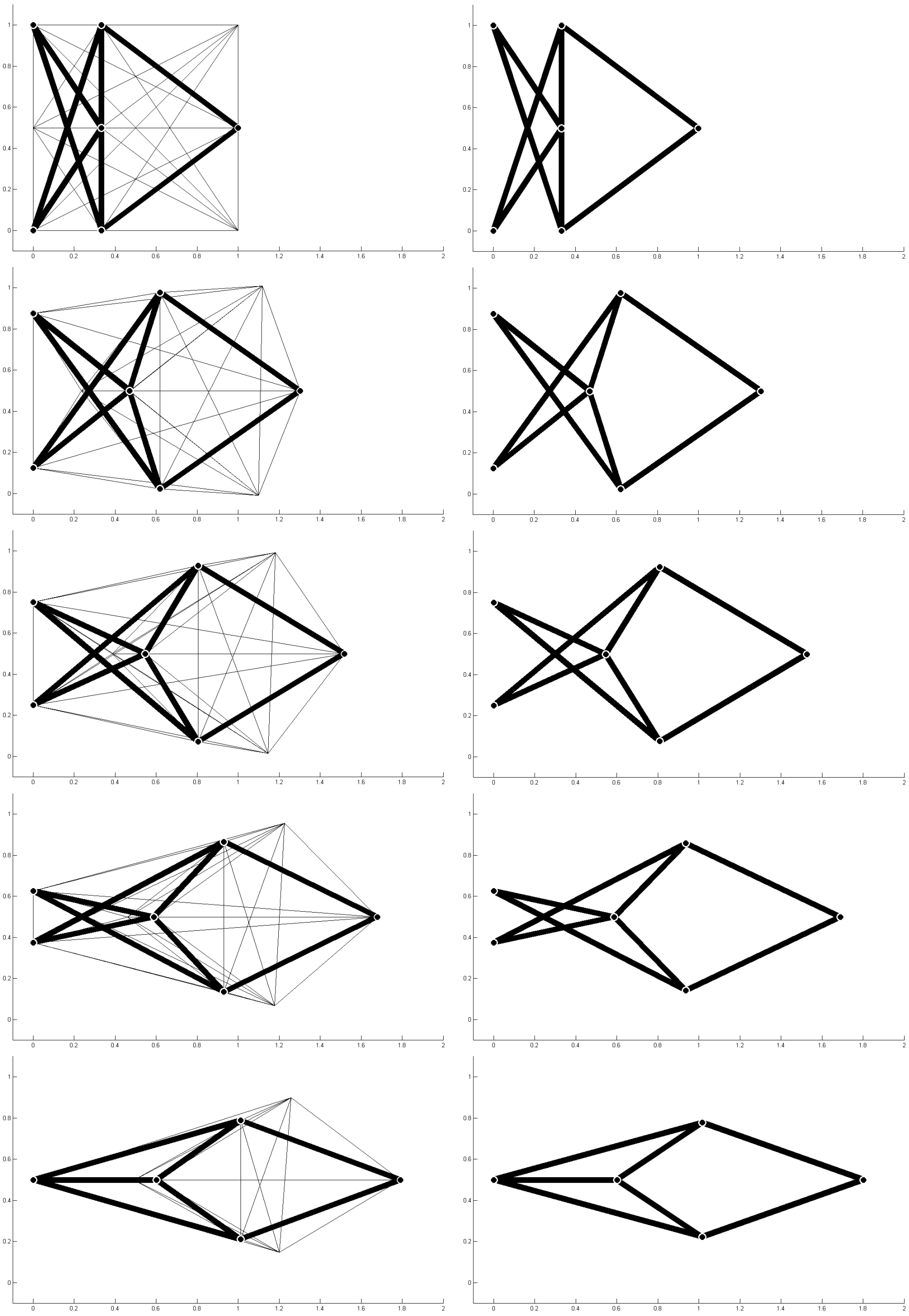

Figure 3.5: The five steps of the actuation of the scissors, before (left) and after (right) post-processing

3.4. MECHANISM SIZING

The second optimization sizes the individual truss members to obtain the minimum weight, while preventing failure. In contrast to the first optimization, penalization is no longer required. After post-processing the geometry obtained from the first optimization, only the necessary elements will remain. By removing the penalization the structural response from the finite element now accurately reflects the structure's ability to carry the aerodynamic loading. The stresses and strains from this finite element analysis can be used in the formulation of various failure modes. In addition, a linear buckling analysis is also performed to take global buckling into account.

3.4.1. OBJECTIVE

After the mechanism design, the sizing optimization is performed. As mentioned earlier the objective is minimum weight, repeated below.

$$F_0 = W = \rho^m \sum_{i=1}^{N_e} \rho_i A_0 l_i \tag{3.84}$$

The weight is calculated by multiplying the density of the material with the volume. The volume depends on the design variables ρ_i. Hence by formulating minimum weight, the optimizer tries to reduce the cross-sectional areas, until one or more failure constraints become active.

3.4.2. CONSTRAINTS

Several constraints are included in the optimization problem, these include the global buckling constraints, stress constraint in tension and compression, and local buckling constraint. Each of these constraints will be covered here.

GLOBAL BUCKLING CONSTRAINT

For global buckling several constraints were defined, a single constraint was given by:

$$G_i^{global\ buckling} = 1 - R_i^{global\ buckling} < 0 \quad i = 1, \ldots, N_{buckl} \times N_s \tag{3.85}$$

Ideally, all these constraints are combined into a single Kreisselmeier-Steinhauser function. However the use of this function has numerical limitations. This functions is the natural logarithm of a sum. So when the sum is equal to zero, the natural logarithm will be minus infinity. The sum would (numerically) be zero when all the buckling constraints are very negative. In practice this would mean than the structure would not buckle, however the optimizer will be stuck once this phenomenon occurs at a certain iteration. For various optimizations this was encountered. Therefore it was decided not to combine the various buckling constraints into a single Kreisselmeier-Steinhauser function, but several separate buckling constraints. In these constraints the buckling load factors are a function of the design variables.

TENSION STRESS CONSTRAINT

The final stress constraint for tension is given by:

$$G^{stress\ tension} = \frac{1}{K_s} ln\left(\sum_{j=1}^{N_t} e^{K_s G_j^{stress\ tension}}\right) < 0 \tag{3.86}$$

Where $G_j^{stress\ tension}$ is a stress constraint for a particular element in a step, given by:

$$G_j^{stress\ tension} = G_{i,k}^{stress\ tension} = \frac{\sigma_{i,k}}{\sigma_y} = \frac{\epsilon_{i,k} E_i}{\sigma_y} \tag{3.87}$$

In this constraint the strain of the ith element depends on the design variables ρ_i. If one assumes the same material for each element, then the Young's modulus and yield stress would be the same for all elements.

COMPRESSION STRESS CONSTRAINT

This constraint is very similar to the tension constraint, only with a minus in front of the actual stress ratio. In this way the constraint is violated if the stress exceeds the negative yield stress.

LOCAL BUCKLING CONSTRAINT

The last constraint is local buckling. The constraint was defined as:

$$G^{local\ buckling} = \frac{1}{K_s} ln\left(\sum_{j=1}^{N_{lb}} e^{K_s G_j^{local\ buckling}}\right) < 0 \tag{3.88}$$

With:

$$G_j^{local\ buckling} = G_{i,k}^{local\ buckling} = -\frac{4\epsilon_{i,k} l_i^2}{\rho_i \pi A_0} - 1 \tag{3.89}$$

In the local buckling constraint is depends in ρ_i directly, as well as via the strain indirectly.

3.4.3. SENSITIVITIES

In this section the sensitivities of the functions are derived. Similar to the previous optimization, the adjoint technique will be used.

WEIGHT

The sensitivities of the objective function can be derived as shown below:

$$\frac{dF_0}{d\rho_i} = \frac{d}{d\rho_i}\left(\rho^m \sum_{i=1}^{N_e} \rho_i A_0 l_i\right) \tag{3.90}$$

The density of the material, the length of the element and the maximum cross-sectional area are independent of the design variables. Hence, the sensitivities simply become:

$$\frac{dF_0}{d\rho_i} = \rho^m A_0 l_i \tag{3.91}$$

GLOBAL BUCKLING CONSTRAINT

The global buckling constraint is slightly more complicated. For convenience the subscript j has been left out. But for every buckling constraint the sensitivity is calculated as shown here. Similar to the first optimization (mechanism design), the residual force vector will be added. Since the eigenvalues of this problem are a function of $\boldsymbol{u}^{(L)}$, the linear residual force vector will be added. Also note that the vector containing the Lagrange multipliers is here denoted as $\boldsymbol{\eta}$, to avoid confusion with the λ indicating the eigenvalue. The derivation is shown for the critical eigenvalue, but also applies to any other eigenvalue.

$$\begin{aligned}
\frac{dG^{global\ buckling}}{d\rho_i} &= \frac{d}{d\rho_i}\left(1-\lambda_{cr}((\boldsymbol{\rho},\boldsymbol{u}^{(L)}(\boldsymbol{\rho}))\right)+\boldsymbol{\eta}^T\frac{d}{d\rho_i}\left(\boldsymbol{R}^{(L)}(\boldsymbol{\rho},\boldsymbol{u}^{(NL)}(\boldsymbol{\rho}),\boldsymbol{u}^{(L)}(\boldsymbol{\rho}))\right)\\
&= -\frac{d\lambda_{cr}((\boldsymbol{\rho},\boldsymbol{u}^{(L)}(\boldsymbol{\rho}))}{d\rho_i}+\boldsymbol{\eta}^T\frac{d}{d\rho_i}\left(\boldsymbol{K}_t(\boldsymbol{\rho},\boldsymbol{u}^{(NL)}(\boldsymbol{\rho}))\boldsymbol{u}^{(L)}(\boldsymbol{\rho})-\boldsymbol{F}\right)\\
&= -\left(\frac{\partial\lambda_{cr}((\boldsymbol{\rho},\boldsymbol{u}^{(L)}(\boldsymbol{\rho}))}{\partial\rho_i}+\frac{\partial\lambda_{cr}(\boldsymbol{\rho},\boldsymbol{u}^{(L)}(\boldsymbol{\rho}))}{\partial\boldsymbol{u}^{(L)}(\boldsymbol{\rho})}\frac{d\boldsymbol{u}^{(L)}(\boldsymbol{\rho})}{d\rho_i}\right)\\
&\quad+\boldsymbol{\eta}^T\left(\frac{d\boldsymbol{K}_t(\boldsymbol{\rho},\boldsymbol{u}^{(NL)}(\boldsymbol{\rho}))}{d\rho_i}\boldsymbol{u}^{(L)}(\boldsymbol{\rho})+\boldsymbol{K}_t(\boldsymbol{\rho},\boldsymbol{u}^{(NL)}(\boldsymbol{\rho}))\frac{d\boldsymbol{u}^{(L)}(\boldsymbol{\rho})}{d\rho_i}\right)\\
&= \left(-\frac{\partial\lambda_{cr}(\boldsymbol{\rho},\boldsymbol{u}^{(L)}(\boldsymbol{\rho}))}{\partial\boldsymbol{u}^{(L)}(\boldsymbol{\rho})}+\boldsymbol{\eta}^T\boldsymbol{K}_t(\boldsymbol{\rho},\boldsymbol{u}^{(NL)}(\boldsymbol{\rho}))\right)\frac{d\boldsymbol{u}^{(L)}(\boldsymbol{\rho})}{d\rho_i}\\
&\quad-\frac{\partial\lambda_{cr}(\boldsymbol{\rho},\boldsymbol{u}^{(L)}(\boldsymbol{\rho}))}{\partial\rho_i}+\boldsymbol{\eta}^T\frac{d\boldsymbol{K}_t(\boldsymbol{\rho},\boldsymbol{u}^{(NL)}(\boldsymbol{\rho}))}{d\rho_i}\boldsymbol{u}^{(L)}(\boldsymbol{\rho})\\
&= \left(-\frac{\partial\lambda_{cr}}{\partial\boldsymbol{u}^{(L)}}+\boldsymbol{\eta}^T\boldsymbol{K}_t\right)\frac{d\boldsymbol{u}^{(L)}}{d\rho_i}-\frac{\partial\lambda_{cr}}{\partial\rho_i}+\boldsymbol{\eta}^T\frac{d\boldsymbol{K}_t}{d\rho_i}\boldsymbol{u}^{(L)}
\end{aligned}\tag{3.92}$$

The partial derivatives of λ_{cr} with respect to the displacement vector and design variables have to be determined. Important to note is that both stiffness matrices are a function of the design variables ρ_i, where only the geometric stiffness matrix is a function of the displacement vector. Starting with $\partial\lambda_{cr}/\partial\boldsymbol{u}^{(L)}$ gives:

$$
\begin{aligned}
\frac{\partial \lambda_{cr}}{\partial \boldsymbol{u}^{(L)}} &= \frac{\partial}{\partial \boldsymbol{u}^{(L)}} \left(- \frac{\boldsymbol{\phi}_{cr}^T \boldsymbol{K}_L \boldsymbol{\phi}_{cr}}{\boldsymbol{\phi}_{cr}^T \boldsymbol{K}_G \boldsymbol{\phi}_{cr}} \right) \\
&= \frac{\boldsymbol{\phi}_{cr}^T \boldsymbol{K}_L \boldsymbol{\phi}_{cr}}{(\boldsymbol{\phi}_{cr}^T \boldsymbol{K}_G \boldsymbol{\phi}_{cr})^2} \left(\boldsymbol{\phi}_{cr}^T \frac{\partial \boldsymbol{K}_G}{\partial \boldsymbol{u}^{(L)}} \boldsymbol{\phi}_{cr} \right) \\
&= \frac{-\lambda_{cr}}{\boldsymbol{\phi}_{cr}^T \boldsymbol{K}_G \boldsymbol{\phi}_{cr}} \left(\boldsymbol{\phi}_{cr}^T \frac{\partial \boldsymbol{K}_G}{\partial \boldsymbol{u}^{(L)}} \boldsymbol{\phi}_{cr} \right) \\
&= \frac{-\lambda_{cr}}{\boldsymbol{\phi}_{cr}^T \boldsymbol{K}_G \boldsymbol{\phi}_{cr}} \left(\boldsymbol{\phi}_{cr}^T \frac{\partial \boldsymbol{K}_G}{\partial \boldsymbol{u}^{(L)}} \boldsymbol{\phi}_{cr} \right)
\end{aligned}
\tag{3.93}
$$

The j^{th} entry of the vector $\boldsymbol{\phi}_{cr}^T \frac{\partial \boldsymbol{K}_G}{\partial \boldsymbol{u}^{(L)}} \boldsymbol{\phi}_{cr}$ is given by:

$$
\boldsymbol{\phi}_{cr}^T \sum_{j=1}^{N_d} \frac{\rho^p A_{max} E_i}{l_i^3} \boldsymbol{b}_i^T \frac{\partial \boldsymbol{u}^{(L)}}{\partial u_j} \tilde{\boldsymbol{B}}_i \boldsymbol{\phi}_{cr} = \boldsymbol{\phi}_{cr}^T \sum_{j=1}^{N_d} \frac{\rho^p A_{max} E_i}{l_i^3} \boldsymbol{b}_i^T \boldsymbol{I}_j \tilde{\boldsymbol{B}}_i \boldsymbol{\phi}_{cr}
\tag{3.94}
$$

Here, $\boldsymbol{I}_j$ is a vector will containing zeros, except for the j^{th} entry, which is equal to one. With this the Lagrange multipliers can be calculated. Finally, the partial derivative of λ_{cr} with respect to the design variables is given by:

$$
\begin{aligned}
\frac{\partial \lambda_{cr}}{\partial \rho_i} &= \frac{\partial}{\partial \rho_i} \left(- \frac{\boldsymbol{\phi}_{cr}^T \boldsymbol{K}_L \boldsymbol{\phi}_{cr}}{\boldsymbol{\phi}_{cr}^T \boldsymbol{K}_G \boldsymbol{\phi}_{cr}} \right) \\
&= - \left(\frac{\boldsymbol{\phi}_{cr}^T \frac{\partial \boldsymbol{K}_L}{\partial \rho_i} \boldsymbol{\phi}_{cr}}{\boldsymbol{\phi}_{cr}^T \boldsymbol{K}_G \boldsymbol{\phi}_{cr}} - \frac{\boldsymbol{\phi}_{cr}^T \boldsymbol{K}_L \boldsymbol{\phi}_{cr}}{(\boldsymbol{\phi}_{cr}^T \boldsymbol{K}_G \boldsymbol{\phi}_{cr})^2} \left(\boldsymbol{\phi}_{cr}^T \frac{\partial \boldsymbol{K}_G}{\partial \rho_i} \boldsymbol{\phi}_{cr} \right) \right) \\
&= - \left(\frac{\boldsymbol{\phi}_{cr}^T \frac{\partial \boldsymbol{K}_L}{\partial \rho_i} \boldsymbol{\phi}_{cr}}{\boldsymbol{\phi}_{cr}^T \boldsymbol{K}_G \boldsymbol{\phi}_{cr}} + \frac{\lambda_{cr}}{\boldsymbol{\phi}_{cr}^T \boldsymbol{K}_G \boldsymbol{\phi}_{cr}} \left(\boldsymbol{\phi}_{cr}^T \frac{\partial \boldsymbol{K}_G}{\partial \rho_i} \boldsymbol{\phi}_{cr} \right) \right) \\
&= - \frac{\boldsymbol{\phi}_{cr}^T \frac{\partial \boldsymbol{K}_L}{\partial \rho_i} \boldsymbol{\phi}_{cr}}{\boldsymbol{\phi}_{cr}^T \boldsymbol{K}_G \boldsymbol{\phi}_{cr}} - \frac{\lambda_{cr}}{\boldsymbol{\phi}_{cr}^T \boldsymbol{K}_G \boldsymbol{\phi}_{cr}} \left(\boldsymbol{\phi}_{cr}^T \frac{\partial \boldsymbol{K}_G}{\partial \rho_i} \boldsymbol{\phi}_{cr} \right) \\
&= - \frac{1}{\boldsymbol{\phi}_{cr}^T \boldsymbol{K}_G \boldsymbol{\phi}_{cr}} \left(\boldsymbol{\phi}_{cr}^T \frac{\partial \boldsymbol{K}_L}{\partial \rho_i} \boldsymbol{\phi}_{cr} + \lambda_{cr} \left(\boldsymbol{\phi}_{cr}^T \frac{\partial \boldsymbol{K}_G}{\partial \rho_i} \boldsymbol{\phi}_{cr} \right) \right)
\end{aligned}
\tag{3.95}
$$

The other terms are simply given by:

$$
\begin{aligned}
\frac{\partial \boldsymbol{K}_L}{\partial \rho_i} &= \frac{p \rho_i^{p-1} A_{max} E_i}{l_i^3} \boldsymbol{b}_i \boldsymbol{b}_i^T \\
\frac{\partial \boldsymbol{K}_G}{\partial \rho_i} &= \frac{p \rho_i^{p-1} A_{max} E_i}{l_i^3} \boldsymbol{b}_i^T \boldsymbol{u}^{(L)} \tilde{\boldsymbol{B}}_i
\end{aligned}
\tag{3.96}
$$

With all the derivatives determined, the final sensitivity can be calculated. The sensitivity is given by Equation 3.92, where the partial derivatives of λ_{cr} are given by Equations 3.93 and 3.94.

TENSION STRESS CONSTRAINT

The next constraint is the tension stress constraint. First the total derivative of the Kreisselmeier-Steinhauser function will be given. This will be derived in this section, but is also used for the compression stress constraint and local buckling constraint.

$$\begin{aligned}
\frac{dG^{stress\ tension}}{d\rho_i} &= \frac{d}{d\rho_i}\frac{1}{K_s} ln\left(\sum_j^{N_t} e^{K_s G_j^{stress\ tension}}\right) \\
&= \frac{\sum_j^{N_t}\left(e^{K_s G_j^{stress\ tension}} \dfrac{dG_j^{stress\ tension}}{d\rho_i}\right)}{\sum_j^{N_t} e^{K_s G_j^{stress\ tension}}}
\end{aligned} \tag{3.97}$$

Now the total derivatives of the individual tension constraints have to be derived. Important to note is that or the derivation of the sensitivities a mechanism is assumed. In other words, the total strain would normally be a function of both $\boldsymbol{u}^{(NL)}$ and $\boldsymbol{u}^{(L)}$. However, for mechanisms the prescribed displacements and the corresponding displacement vector do not result in strains. Therefore the strain is only a function of the $\boldsymbol{u}^{(L)}$. This simplifies the derivation of the sensitivities. Hence the sensitivities can be written as:

$$\begin{aligned}
\frac{dG_j^{stress\ tension}}{d\rho_i} &= \frac{E}{\sigma_y}\frac{d\epsilon_j(\boldsymbol{u}^{(L)}(\boldsymbol{\rho}))}{d\rho_i} \\
&= \frac{E}{\sigma_y}\frac{d\epsilon_j(\boldsymbol{u}^{(L)}(\boldsymbol{\rho}))}{d\rho_i} + \boldsymbol{\lambda}^T \frac{d\boldsymbol{R}^{(L)}(\boldsymbol{\rho},\boldsymbol{u}^{(L)}(\boldsymbol{\rho}))}{d\rho_i}
\end{aligned} \tag{3.98}$$

The Lagrange vector is denoted as $\boldsymbol{\lambda}$. For clarity the dependencies are not shown, now the sensitivities become:

$$\begin{aligned}
\frac{dG_j^{stress\ tension}}{d\rho_i} &= \frac{E}{\sigma_y}\frac{\partial\epsilon_j}{\partial\boldsymbol{u}^{(L)}}\frac{d\boldsymbol{u}^{(L)}}{d\rho_i} + \boldsymbol{\lambda}^T\left(\frac{\partial\boldsymbol{R}^{(L)}}{\partial\rho_i} + \frac{\partial\boldsymbol{R}^{(L)}}{\partial\boldsymbol{u}^{(L)}}\frac{d\boldsymbol{u}^{(L)}}{d\rho_i}\right) \\
&= \left(\frac{E}{\sigma_y}\frac{\partial\epsilon_j}{\partial\boldsymbol{u}^{(L)}} + \boldsymbol{\lambda}^T\frac{\partial\boldsymbol{R}^{(L)}}{\partial\boldsymbol{u}^{(L)}}\right)\frac{d\boldsymbol{u}^{(L)}}{d\rho_i} + \boldsymbol{\lambda}^T\frac{\partial\boldsymbol{R}^{(L)}}{\partial\rho_i}
\end{aligned} \tag{3.99}$$

The partial derivatives of the linear residual force vector have already been determined in the sensitivities for the mechanism design, hence will not be repeated here. Also, the partial derivative of the strain with respect to the displacement vector has already been derived previously, and was given by Equation 2.25. With all the terms known, the sensitivities can be computed.

COMPRESSION STRESS CONSTRAINT

The sensitivities of the compression stress constraint are equal in magnitude but opposite in sign compared to the tension constraint.

LOCAL BUCKLING CONSTRAINT

Finally, the sensitivities of the local buckling constraint are needed. Again only the sensitivities for a single constraint will be derived. This will have to be repeated for each element in each step of the actuation. The sensitivities have to be combined as given by equation 3.97. Now the sensitivities for a single constraint is given by:

$$\begin{aligned}
\frac{dG_j^{local\ buckling}}{d\rho_i} &= \frac{d}{d\rho_i}\left(\frac{-4l_j^2\epsilon_j(\boldsymbol{u}^{(L)}(\boldsymbol{\rho}))}{\pi A_0\rho_j}\right) \\
&= \frac{-4l_j^2}{\pi A_0}\frac{d}{d\rho_i}\frac{\epsilon_j(\boldsymbol{u}^{(L)}(\boldsymbol{\rho}))}{\rho_j} \\
&= \frac{-4l_j^2}{\pi A_0}\frac{d}{d\rho_i}\frac{\epsilon_j(\boldsymbol{u}^{(L)}(\boldsymbol{\rho}))}{\rho_j} + \boldsymbol{\lambda}_{lb}^T\left(\frac{\partial \boldsymbol{R}^{(L)}}{\partial\rho_i} + \frac{\partial \boldsymbol{R}^{(L)}}{\partial \boldsymbol{u}^{(L)}}\frac{d\boldsymbol{u}^{(L)}}{d\rho_i}\right) \\
&= \frac{-4l_j^2}{\pi A_0}\left(\frac{\partial\epsilon_j}{\partial \boldsymbol{u}^{(L)}}\frac{d\boldsymbol{u}^{(L)}}{d\rho_j} + \frac{\partial}{\partial\rho_i}\frac{1}{\rho_j}\right) + \boldsymbol{\lambda}_{lb}^T\left(\frac{\partial \boldsymbol{R}^{(L)}}{\partial\rho_i} + \frac{\partial \boldsymbol{R}^{(L)}}{\partial \boldsymbol{u}^{(L)}}\frac{d\boldsymbol{u}^{(L)}}{d\rho_i}\right) \\
&= \left(\frac{-4l_j^2}{\pi A_0}\frac{\partial\epsilon_j}{\partial \boldsymbol{u}^{(L)}} + \boldsymbol{\lambda}_{lb}^T\frac{\partial \boldsymbol{R}^{(L)}}{\partial \boldsymbol{u}^{(L)}}\right)\frac{d\boldsymbol{u}^{(L)}}{d\rho_j} - \frac{4l_j^2}{\pi A_0}\frac{\partial}{\partial\rho_i}\frac{1}{\rho_j} + \boldsymbol{\lambda}_{lb}^T\frac{\partial \boldsymbol{R}^{(L)}}{\partial\rho_i}
\end{aligned} \tag{3.100}$$

The Lagrange multipliers are collected in the vector $\boldsymbol{\lambda}_{lb}$. This vector can be obtained as was done for the stress constraints. The partial derivative of the residual force vector with respect to the design variables is also previously determined. Only the term $\partial/\partial\rho_i(1/\rho_j)$ has to be determined, which is given below:

$$\frac{\partial}{\partial\rho_i}\frac{1}{\rho_j} = \begin{cases} 0 & \text{if } i \neq j \\ \dfrac{-1}{\rho_j^2} & \text{if } i = j \end{cases} \tag{3.101}$$

Finally, all the sensitivities derived in this chapter have been verified with finite differences. The sensitivities were found to be the same.

4

DESIGN CASES

In the previous two chapters the tool has been discussed in detail. In Chapter 2 the finite element analysis and the linear buckling analysis were covered. In Chapter 3 the optimization strategy, including the mechanism design and mechanism sizing, was explained. With these two optimizations, mechanisms for morphing winglets could be designed and sized.

Over the years there has been a significant growth in the regional air transport. These trajectories are characterized by relative short distances. As a result, the time associated with take-off and landing becomes significant compared to the entire duration, this in contrast to long-haul flights. Where for long-haul aircraft the winglet can be designed for cruise only, for regional aircraft the take-off and landing should be taken into account. Therefore in this thesis the design cases are focused on regional aircrafts, specifically the C295 military transport aircraft from airbus. A picture of this aircraft can be found in Figure 4.1.

Figure 4.1: Picture of Airbus C295, military transport aircraft [26]

Based on the C295, the dimensions of the winglet and the aerodynamic loading could be defined. For he design cases the length of the winglet is set to 2 meters. The width starts at 1 meter and has a taper ratio of a half, resulting in a width of 50 centimeters at the tip. The aerodynamic loading is simplified to a point load, acting in the middle of the winglet length (and in 3D at a quarter of the chord). The lifting force was estimated using Proteus, an aeroelastic model developed in house by the Aeroelasticity and Morphing Wings (AaM) research group of my faculty aerospace engineering of the Delft University of Technology. The aerodynamic force was estimated to be 5 [kN] in the maneuver load case of 2.5g. It is assumed that the loading remains constaint at 5 [kN] and remains perpendicular to the winglet. With these specifications the mechanisms could be designed and sized. In Section 4.1 the 2D results can be found and in Section 4.2 the 3D results.

4.1. TWO DIMENSIONAL MORPHING WINGLET

In this section the 2D mechanisms are covered. As a result of the geometric non-linearity the design space is non-convex, resulting in several (local) minima. To overcome this several optimizations are performed, each with a random design vector. From these optimizations 4 different mechanisms were obtained, which are presented in this section. These mechanisms are also sized to obtain the minimum weight, while satisfying several failure constraints. First the optimization problems are defined, followed by the results obtained from it.

4.1.1. PROBLEM FORMULATION

As mentioned in the beginning of this chapter, the winglet was set to 2 meters long. The width of the design space was set to 0.4 meters and the height to 0.3 meters. These dimensions were chosen to be the same as used in the previous work done by the AaM research group of my faculty aerospace engineering of the Delft University of Technology [21]. This design space is discretized by defining 3 nodes along the width and 3 nodes along the height, resulting in a total of 9 nodes. Connecting these 9 nodes with all possible combinations, results in truss members in the design space. The cross-sectional area of these 36 elements are used as design variables. An illustration of the design space could be found in Figure 4.2. To prevent rigid body motions, the upper and lower left nodes are pinned. This is illustrated by the roller supports. Also, the middle left node (indicated with the blue circle) is chosen to be the input node, whereas the most right node (the tip node of the winglet, indicated with the green circle) is selected for the output node. The actuation will be done in 5 steps. The horizontal displacement is prescribed, with a maximum actuation of 0.11 meters. The vertical displacement of the input node is free. For the output node a circular trajectory of 45 degrees is prescribed. The radius of this circular motion is set to 2.2 meters, which is equal to the winglet length plus half of the design space. This again is chosen to be the same as was done in the previous work of the faculty. The layout of the winglet itself is chosen such that in the middle of a winglet a node is present, where the aerodynamic loading will be acting on. This is illustrated by the red arrow.

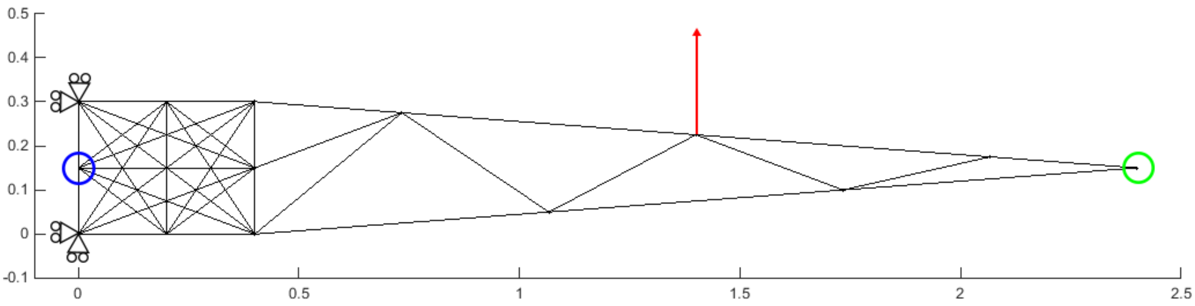

Figure 4.2: Truss ground-structure (design space) for 2D winglets

With this description, the following optimization problem could be defined for the mechanism design in 2D. As mentioned before only a single input node and a single output node are used, which together with the volume constraint, results in 3 constraints. For the output node the average of the trajectory constraint in each step is taken. The design variables ρ_i are the cross-sectional area scaling parameters. where A_i is given by:

$$A_i = \rho_i^3 A_0 \tag{4.1}$$

The penalization factor is set to 3, which is commonly done in this field. The lower bound for the design variables was chosen to be 0.001. This is very small, which would not affect the kinematics of the mechanism.

$$\begin{aligned} \min_{\rho} F_0 &= \frac{1}{5}\sum_{k=1}^{5}\left[C_k + \left(F_k^{input}\right)^2\right] \\ s.t. &= \left\{ \begin{array}{lll} G^{trajectory} & = \frac{1}{5}\Sigma_{k=1}^{5}\left[R_k^{trajectory} - 1\right] & < 0 \\ G^{volume} & = R^{volume} - 1 & < 0 \\ G^{input\ node} & = 1 - R^{input\ node} & < 0 \\ 0 \leq \rho_{min} & \leq \rho_i & \leq 1 \end{array} \right. \end{aligned} \tag{4.2}$$

The maximum allowable deviation for the output trajectory (Δ^{max}) was set to 0.1. The maximum number of elements in the design space (V^{max}) was set 4. And, as already mentioned earlier at least 2 elements should be attached to the input node.

Finally, for the mechanism design not the actual material properties are used, because only the relative cross-sectional areas determine which elements need to be removed and which ones are needed. Therefore the same material properties for the mechanism design were used as Kawamoto used for his optimizations [30]. The Young's modulus E was set to 10 and the cross-sectional area A_0 to 1. Finally, the aerodynamic loading has been set to 1 for convenience.

Once a mechanism is found, the individual elements of the mechanism are sized to obtain the minimum weight, under the condition that no failure occurs. In 2D it is assumed that two mechanisms would carry the total aerodynamic loading, which would yield a load of 2.5 [kN] for the 2D mechanisms. Also, as discussed in the previous chapter for stress in tension, stress in compression and local buckling a single constraint could be formulated. For the global buckling a set of constraints is added. Again the actuation will be done in 5 steps, where in each step the lowest three buckling modes are taken into account. This result in 15 global buckling constraints. This gives the following optimization problem:

$$
\begin{aligned}
\min_{\rho} F_0 &= \rho^m \sum_{i=1}^{N_e} \rho_i A_0 l_i \\
s.t. &= \begin{cases}
G_j^{global\ buckling} & & < 0 \quad j = 1, \dots, 15 \\
G^{stress\ tension} & & < 0 \\
G^{stress\ compression} & & < 0 \\
G^{local\ buckling} & & < 0 \\
0 \leq \rho_{min} & \leq \rho_i & \leq 1
\end{cases}
\end{aligned}
\tag{4.3}
$$

The material selected is aluminum 2024-T3. The Young's modulus (E) is 73.1 [GPa], the yield stress (σ_y) for tension and compression is 310 [MPa], and the material density (ρ^m) is 2780 [kg/m^3]. The results obtained from the optimizations are presented in the next section.

4.1.2. RESULTS

The resulted obtained from the mechanism design optimizations can be found in Figure 4.3. Four different mechanisms were found, each of which was able of follow the specified trajectory. This will be covered in more detail later on. The first mechanism consists of four elements, hence satisfies the volume constraint. In addition, two elements are attached to the input node.

The second mechanism has five thick elements. This is very interesting, since the volume constraint specified only four elements. However, looking closely at the mechanism, two of the elements have only a thickness which is half the maximum thickness. Therefore, mechanism 2 also complies with the volume constraint of four elements in total, which is this case results in two elements of a half. These two elements are a factor 2 smaller compared to the other three elements, but are several order of magnitude larger than the thin elements which need to be removed. These elements all have a cross-sectional area equal to the lower bound. this means that these two elements do influence the kinematics and should be maintained in the solution. This, in contrast to the other elements which have cross-sectional areas (almost) equal to the lower bound. This mechanism has a total of three elements attached to he input node.

The third mechanism is very similar to the second one. Both mechanisms follow the same trajectory. Where in the second mechanisms five elements turned out to be needed, here only four elements are needed. All other, very thin, elements need to be removed. Note that also three elements are attached to the input node.

The fourth and final mechanism also consists of four elements. Two of those elements are attached to the input node.

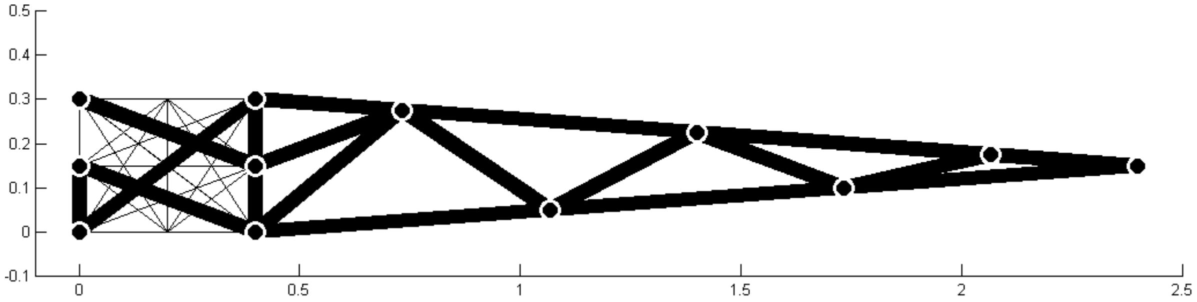

(a) Mechanism 1

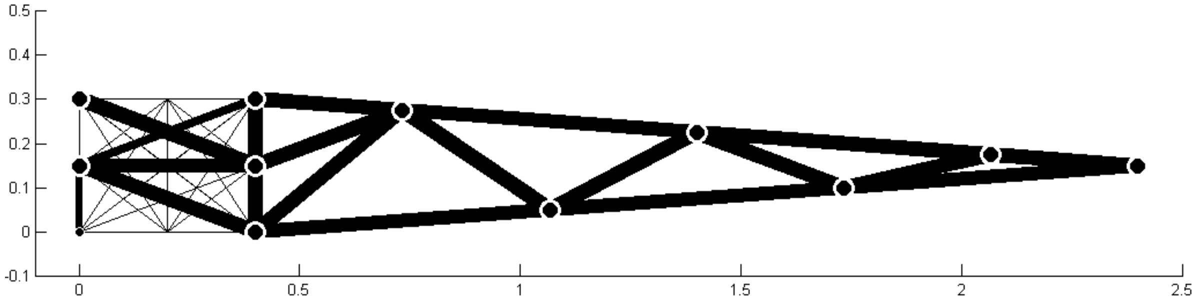

(b) Mechanism 2

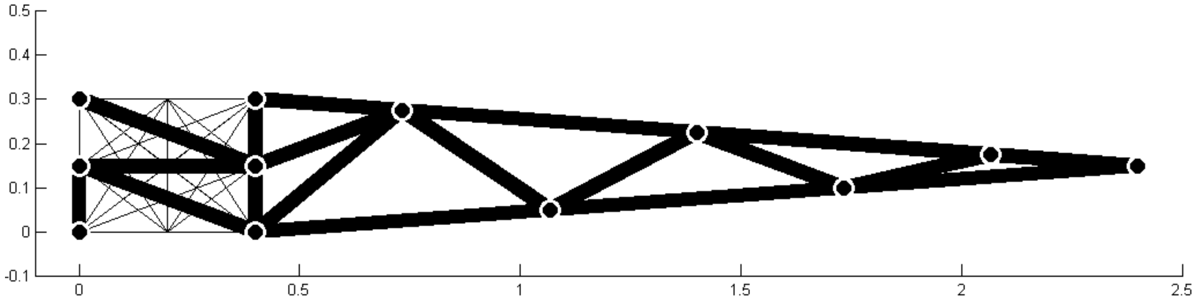

(c) Mechanism 3

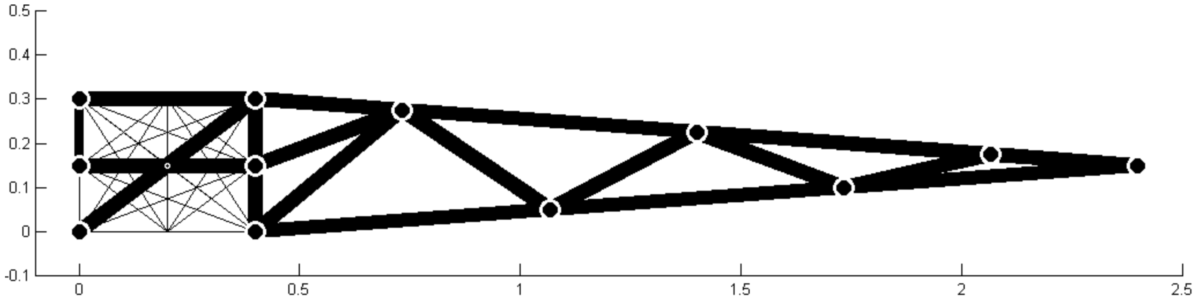

(d) Mechanism 4

Figure 4.3: Converged 2D winglet mechanisms before post-processing

The optimization histories of the four mechanisms are shown in Figure 4.4. Since the objective function for these optimizations does not represent a physical quantity, the results are normalized with the converged value of the objective function. This will give for all four mechanisms a value 1 for the converged objective function. Interesting to note is that for mechanism 1 the trajectory constraint is not active. This means that the mechanism is able to satisfy (on average) the trajectory constraint very well. The bounding box Δ_{max} could have been smaller at this mechanism could still be found. For the other mechanisms the trajectory constraint is active, which means that these mechanisms just satisfy the trajectory. For the mechanisms 2 and 3 it is interesting to note that the input node connectivity constraint is not active. This means that more than 2 elements are attached to the input node. This is confirmed by the topology, where indeed 3 elements are attached to the input node. Finally, for all mechanisms the volume constraint is active, which would mean that each mechanism consists of four elements, this is indeed the case. Also for mechanism two the total number of full elements would be four.

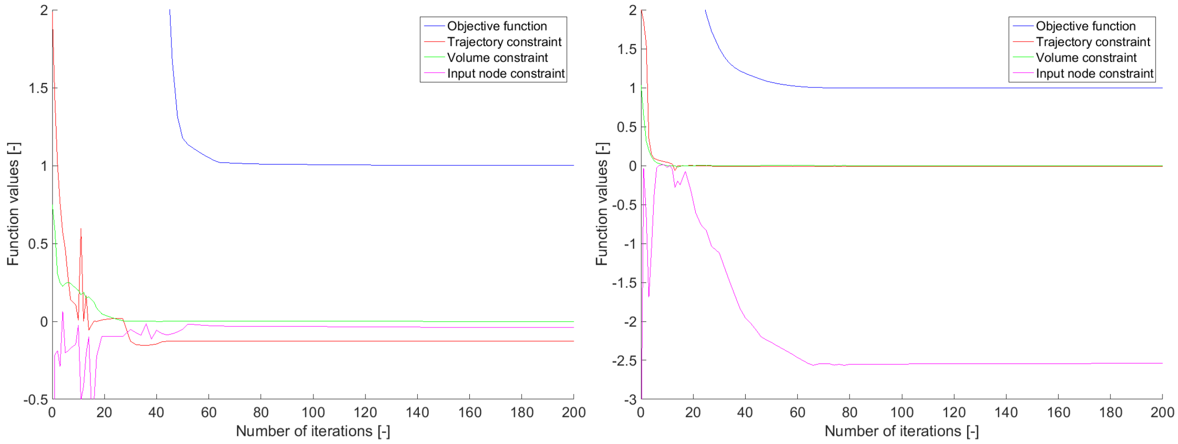

(a) Mechanism 1

(b) Mechanism 2

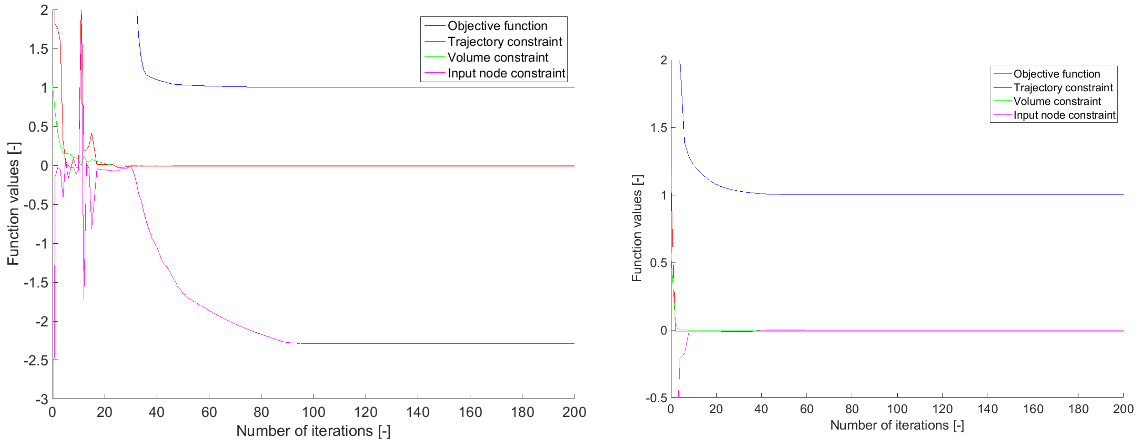

(c) Mechanism 3

(d) Mechanism 4

Figure 4.4: Optimization history of mechanism design for 2D winglets

The results obtained from the mechanism design are post-processed before the mechanism sizing could be done. With post-processing the very thin elements are removed, while the significant elements are maintained. This would yield the final mechanisms as shown in Figure 4.5.

The volume constraint and input node connectivity could be visualized in the topology. The trajectory, however, does not become clear form the geometry. Therefore the trajectory constraint is visualized in Figure 4.6. The target trajectory is plotted with the circular bounding box. Also mechanism 4 is included to have an illustrate how the trajectory is specified with respect to the mechanisms. As can be seen from the figure, mechanism one satisfies the trajectory constraint in every step. In each of the five steps the output node lies within the bounding box. For the other mechanisms this is not the case, in some instances the output node does lie within the bounding box, in other instances it lies beyond the bounding box. This can be explained by the fact that on average the nodes should lie within the bounding boxes, which allows for some flexibility in the designs. This was done on purpose, since this approach yields mechanisms like 2, 3 and 4, which would not have been found in the trajectory should be satisfied in each step. Then only mechanism 1 would be found, whereas the other mechanisms are also very worth considering. One final note, mechanism 1 lies in each step within the bounding box. This means that in each step the trajectory is satisfied, but not active. Hence the average of these steps would yield a constraint which is also not active. This explains why the trajectory constraint or mechanism 1 is not active.

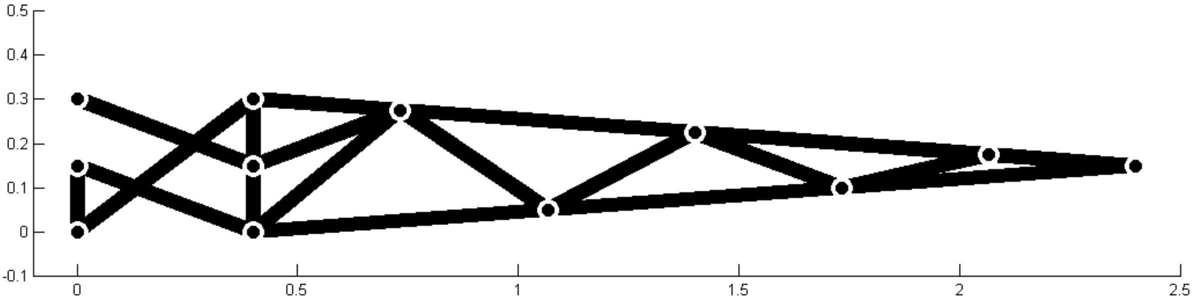

(a) Mechanism 1

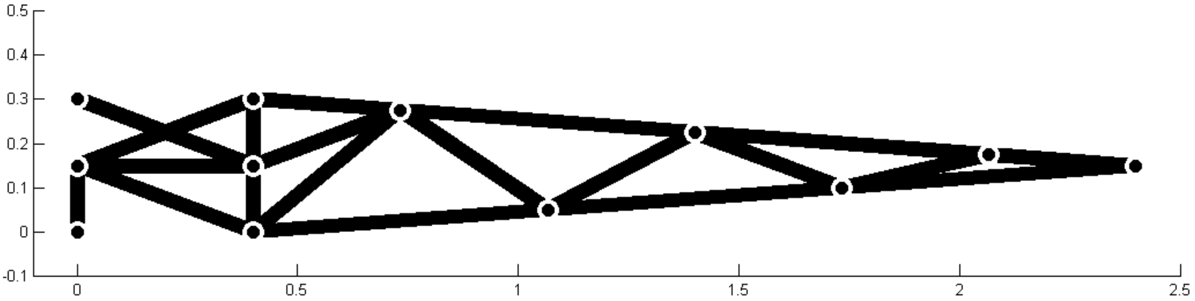

(b) Mechanism 2

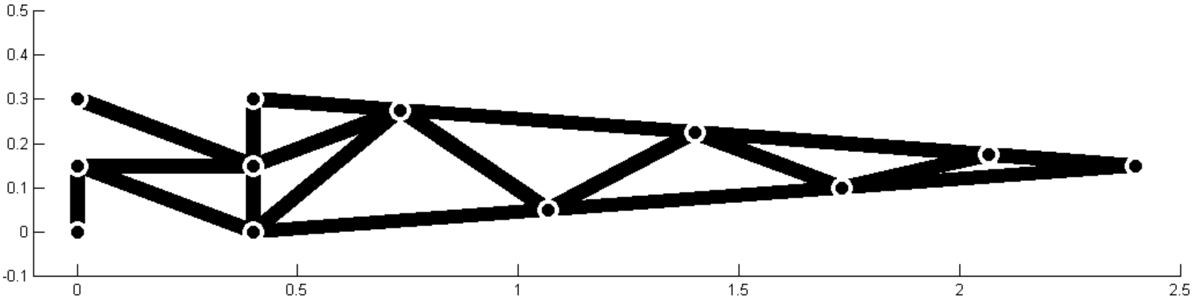

(c) Mechanism 3

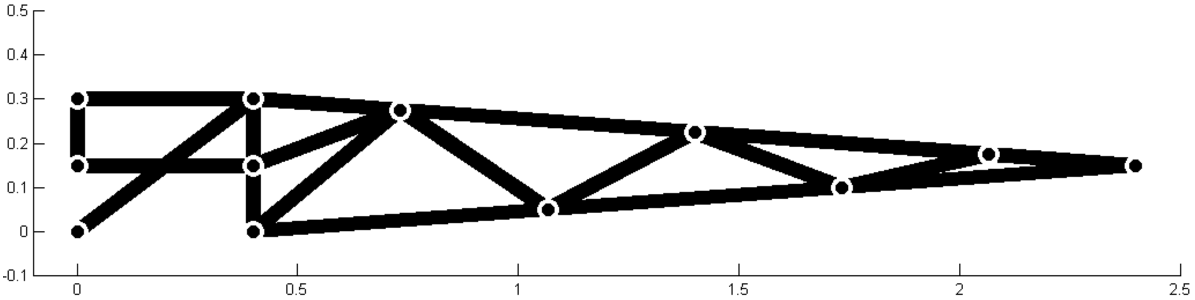

(d) Mechanism 4

Figure 4.5: Converged 2D winglet mechanisms after post-processing

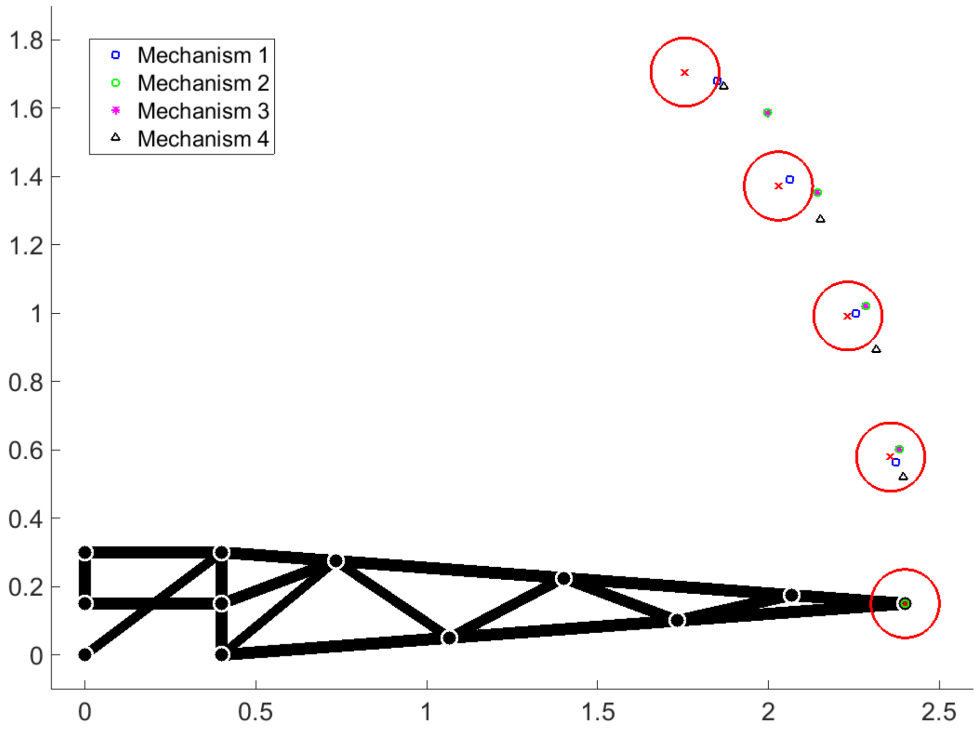

Figure 4.6: Trajectories of 2D winglets

The next optimizations are the sizing optimizations. As mentioned before, 15 global buckling constraints were specified and 3 other failure constraints. Hence a total of 18 constraints will have to be satisfied. The optimized results are shown in Figure 4.7. The mechanisms have weights ranging from 15.0 [kg] to 20.0 [kg]. Inspecting the geometries it is interesting to see that the upper element in the mechanism will always be the thickest. Clearly the mechanism consist of a load carrying part and an actuation part. In the figure the colors of the members represent the cross-sectional areas in square centimeters. Mechanisms 1 and 2 are the lightest with a weight of 15.2 [kg] and 15.0 [kg] respectively. Interesting to note is that mechanism 2, which consists of 5 elements, turns out to be lighter than mechanism 3, which consists of 4 elements. Therefore the minimum number of elements does not necessarily yield the lightest designs.

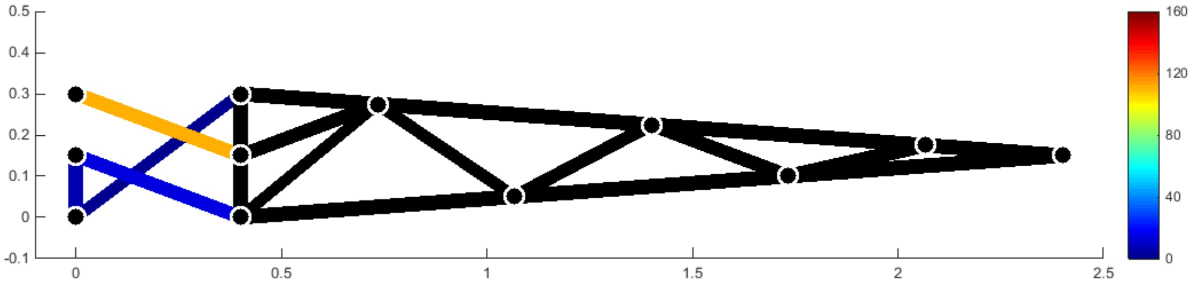

(a) Mechanism 1, weight 15.2 [kg]

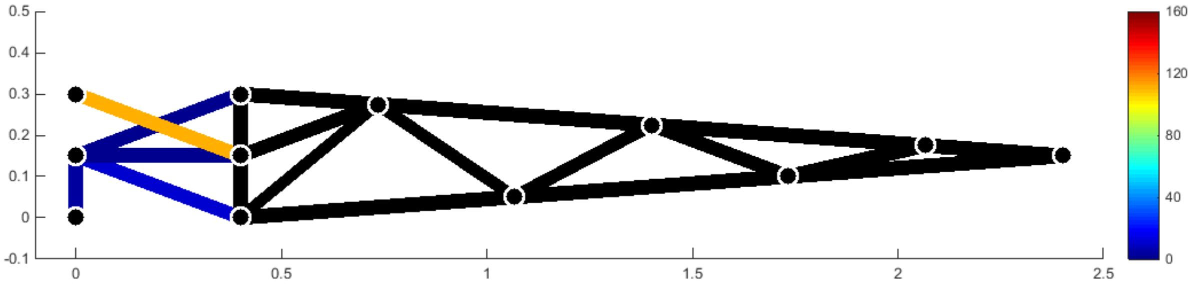

(b) Mechanism 2, weight 15.0 [kg]

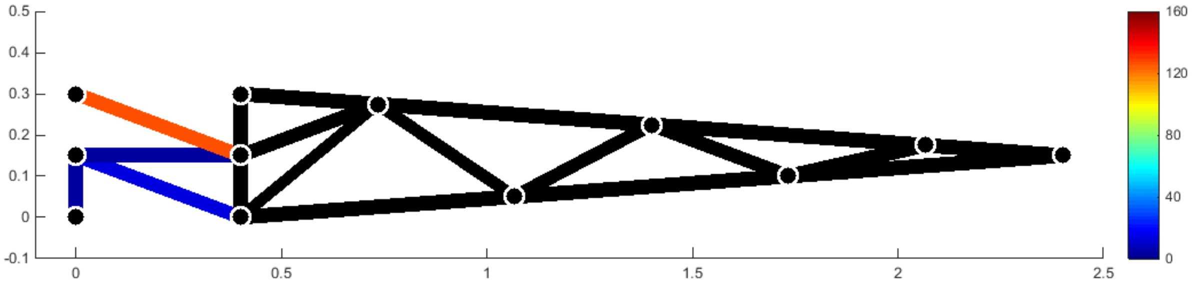

(c) Mechanism 3, weight 16.9 [kg]

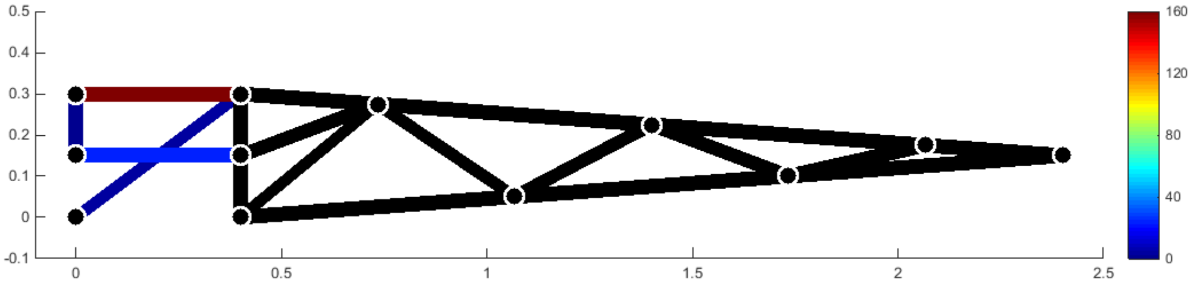

(d) Mechanism 4, weight 20.0 [kg]

Figure 4.7: Converged 2D winglet mechanisms after sizing. The colors give the cross-sectional areas in [cm^2].

The optimization histories for sizing are shown in Figure 4.8. In the left figures the optimization history is given, where also the weight (objective function) is visualized. The right figures zoom in on the constraints, to see which constraint or constraints become active. From these figures it becomes clear that global buckling is the critical failure mode for these geometries. The other failure modes (local buckling, stress in tension and stress in compression) are not driving the design. This is somewhat intuitive, since the structures are relatively large. During the optimizations the weight continuously decreases, and the constraints tend to go to zero, meaning that they become active. As mentioned earlier, 15 buckling modes are included. The lowest three buckling modes of each step are taken into account, therefore not all buckling modes could become active. Either 1 or 2 buckling modes become active, limiting the geometry to reduce further in weight.

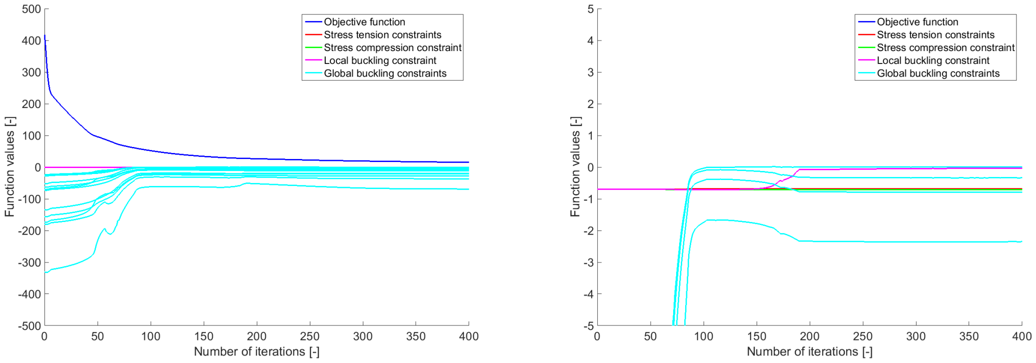

(a) Mechanism 1 (b) Mechanism 1 zoom

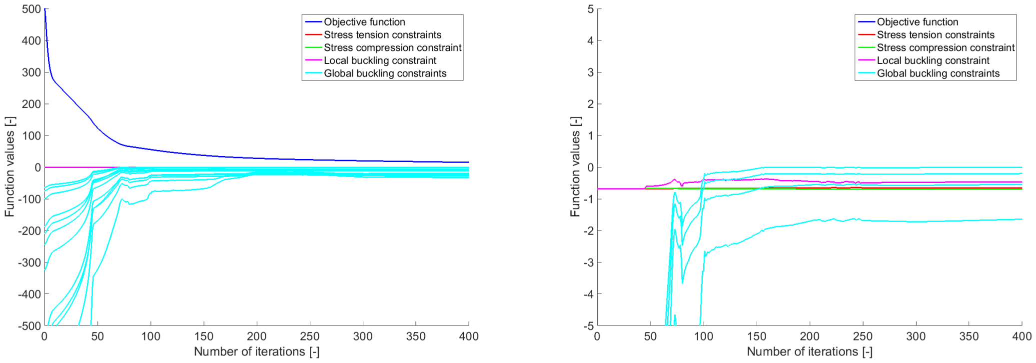

(c) Mechanism 2 (d) Mechanism 2 zoom

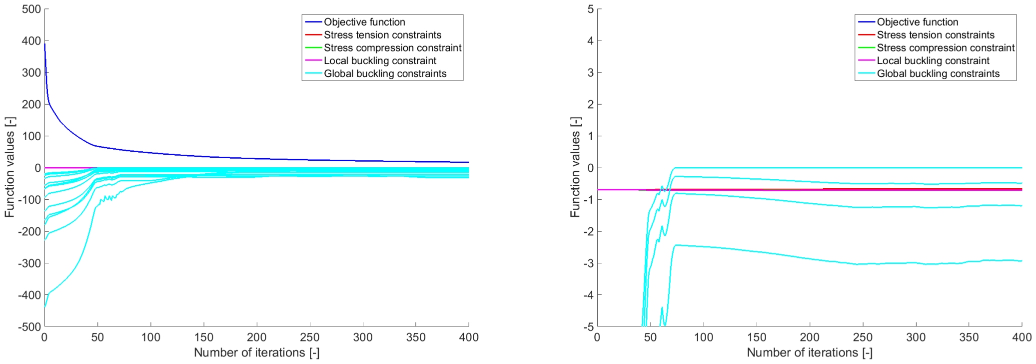

(e) Mechanism 3 (f) Mechanism 3 zoom

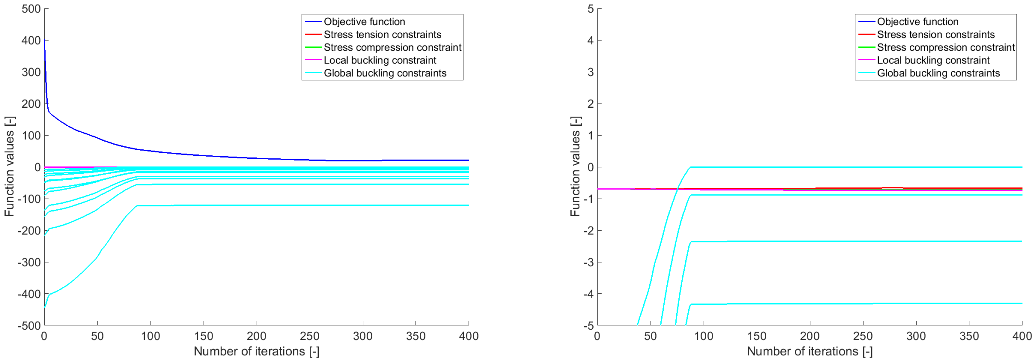

(g) Mechanism 4 (h) Mechanism 4 zoom

Figure 4.8: Optimization history of mechanism sizing for 2D winglets

4.2. THREE DIMENSIONAL MORPHING WINGLET

One of the research goals was to extend the tool to 3D. This has been done and the results are presented in this section. First the problem formulations are covered, which slightly deviate from the 2D optimizations, followed by the mechanisms found. In 3D two different mechanisms are shown, one mechanism can only change the cant angle, whereas the other mechanism can both change the cant angle and the toe angle. An illustration of the cant angle and the toe angle can be found in Figure 4.9 [42]. When the cant angle is zero, the winglet becomes a wing extension. The toe angle is the angle the winglet makes with the aircraft's vertical axis.

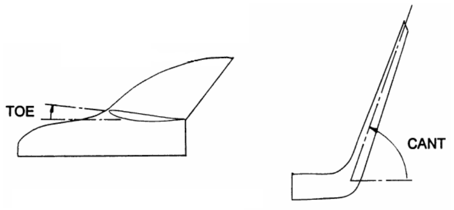

Figure 4.9: Illustration of the toe angle and cant angle of a winglet

4.2.1. PROBLEM FORMULATION

The dimensions of the winglet were already covered. The length was set to 2 meters, the width started at 1 meter, and was 50 centimeters at the tip. The width and the weight were kept the same and equal to 0.4 meters and 0.3 meters respectively. The depth is equal to the width of the winglet and therefore set to 1 meter. The total number of nodes in the design space was set to 18, again 3 by 3, but only 2 in the third direction. This is illustrated in Figure 4.10. Three different views of the design space are given in Figure 4.11. For clarity the nodes were amplified, the better visualize the design space.

Similar to the 2D design space, the corner nodes of the design space are pinned. This is illustrated with the triangles at the four corner nodes. Also, the middle two nodes were used as input nodes (illustrated with the blue circles). The actuation is only prescribed in the horizontal direction, where the other dimensions were free. the actuation will be done in 5 steps, up to 0.11 meters. The two most right nodes, the winglet tip nodes, were selected for the output nodes. This is illustrated with the green circles. For the first mechanism for both output nodes the same circular motion was prescribed as done in 2D. Hence for both nodes a trajectory of 45 degrees was specified. This trajectory would yield mechanisms which can change the cant angle of the winglet. For the second mechanism, however, a different trajectory was specified for the nodes. For one node 45 degrees was specified, where for the other node 55 degrees was specified. This was done to find mechanisms which both regulate the cant angle as well as the toe angle. The layout of the winglet was chosen such that in the middle of the winglet length and at a quarter chord a node is present for the aerodynamic loading. The loading is illustrated by the red arrow.

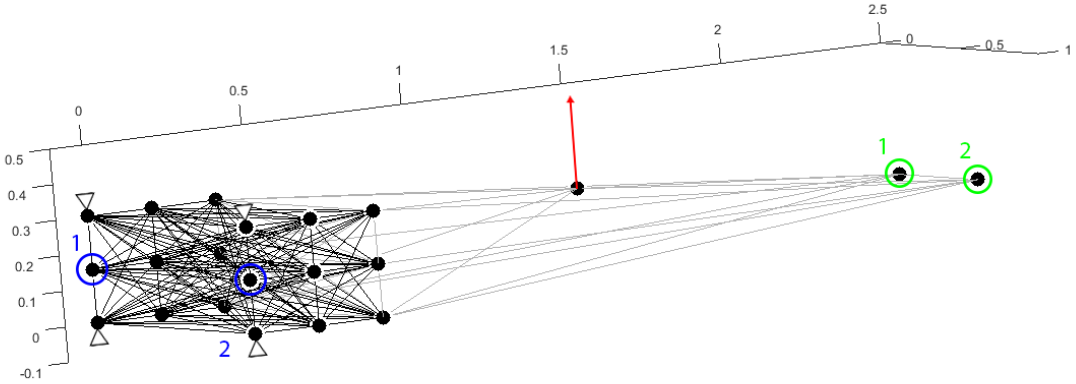

Figure 4.10: Truss ground-structure (design space) for 3D winglets

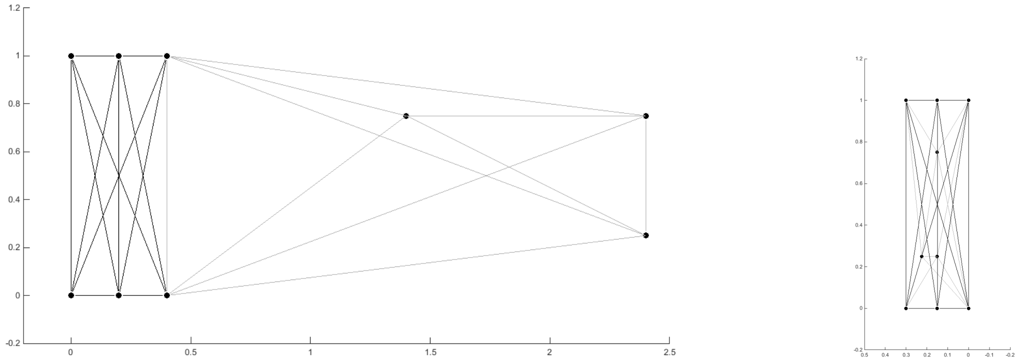

(a) Top view (b) Side view

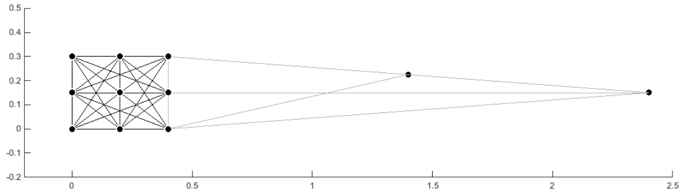

(c) Front view

Figure 4.11: Views of design space used for the 3D winglets

With this geometry, the optimization problem in 3D could be written as shown in Equation 4.4. The reaction force term in the objective function becomes a summation of the two input nodes. Also, given the two input nodes, two constraints are specified for the input node connectivity. In addition, two trajectory constraints are specified for the output nodes. Hence, a total of 5 constraints are defined. The variable Δ_{max} was kept the same as for 2D, where V_{max} was set to 10 elements. or the mechanism design the material properties are again set to 10 for the Young's modulus and 1 for the cross-sectional area.

$$
\begin{aligned}
\underset{\rho}{min}\, F_0 &= \frac{1}{5}\sum_{k=1}^{5}\left[C_k + \sum_{i=1}^{2}\left(F_{i,k}^{input}\right)^2 \right] \\
s.t. &= \left\{ \begin{array}{lll}
G_1^{trajectory} & = \frac{1}{5}\sum_{k=1}^{5}\left[R_{1,k}^{trajectory} - 1\right] & < 0 \\
G_2^{trajectory} & = \frac{1}{5}\sum_{k=1}^{5}\left[R_{2,k}^{trajectory} - 1\right] & < 0 \\
G^{volume} & = R^{volume} - 1 & < 0 \\
G_1^{input\ node} & = 1 - R_1^{input\ node} & < 0 \\
G_2^{input\ node} & = 1 - R_2^{input\ node} & < 0 \\
0 \leq \rho_{min} & \leq \rho_i & \leq 1
\end{array} \right.
\end{aligned}
\tag{4.4}
$$

Given the two input nodes, two input node constraints were specified. The first constraint refers to the first input node (indicated with the blue 1 in Figure 4.10) and the second constraint refers to the second input node (indicated with the blue 2 in Figure 4.10). Similarly, two output node constraints were specified. The first output node is indicated with the green number 1, the second output node with the green number 2, also shown in Figure 4.10.

The optimization problem for sizing remains unchanged compared to the 2D formulation. The same material properties are used, the actuation is done in 5 steps and in each step the three lowest buckling modes are taken into account. The problem formulation for the sizing can therefore be written as:

$$\begin{aligned} &\min_{\rho} F_0 = \rho^m \sum_{i=1}^{N_e} \rho_i A_0 l_i \\ &s.t. = \begin{cases} G_j^{global\ buckling} & < 0 \quad j = 1, ..., 15 \\ G^{stress\ tension} & < 0 \\ G^{stress\ compression} & < 0 \\ G^{local\ buckling} & < 0 \\ 0 \le \rho_{min} \quad \le \rho_i & \le 1 \end{cases} \end{aligned} \tag{4.5}$$

4.2.2. RESULTS

As mentioned earlier, the first mechanism is obtained when a trajectory of 45 degrees is specified for both nodes. The mechanism found can be seen in Figure 4.12. In blue the input trajectory is specified and in pink the target output trajectory. Also, only the post-processed geometry is shown, since the mechanism is very difficult to recognize given the many elements in the design space. It can be seen that the mechanism is able to follow the trajectory well. The actual location of the output nodes are given in green (when it lies within the bounding box) or red (when it lies outside the bounding box). Plotting the bounding boxes, as was done in 2D, was found to be unclear. The bounding boxes in 3D are spheres, which were difficult to represent in a clear way. Therefore it was decided to plot the actual nodal locations for the output nodes in green and red.

For this mechanism the output nodes lie in each step within the bounding box, hence all the locations are given in green. In fact, the mechanism is similar to the first mechanism found in 2D. The mechanism indeed follows a 2D trajectory. In 3D however, a few more elements are needed to prevent additional degrees of freedom. The final mechanism consists of 11 elements. As can be seen 8 elements actually carry the load and determine its kinematics, the other 3 are connected to the input nodes to restrain the out of plane displacements.

The optimization history for the 3D mechanism design is shown in Figure 4.13. Similar to the 2D cases, the objective does not represent a physical quantity. Hence, the values are normalized with respect to the converged objective function value. This can be seen in the optimization history, where the objective function converges to 1. Also, as can be seen, the volume constraint is active. This is expected, since the more material in the design space, the smaller the compliance. Hence for optimizations with compliance in the objective, the volume constraint is expected to be active. Also 1 input node constraint is active, while the other is not. This can be explained by the fact that before post-processing a bit more material is attached to the first input node. A bit more that a total of 2 was connected at the input node. As a result the constraint is not active. Similar behavior is observed when the two trajectory constraints are compared. Both constraints were not active, but one is more negative than the other. This can be explained by the fact that 10 elements were specified for the volume constraint. The actual mechanisms consists of 11 elements, which means that the total volume has to be distributed among these elements. This, in combination with the loading not acting in the middle of the chord, yields an unsymmetrical material distribution, explaining the different paths the two output nodes travel.

The second optimization would be the sizing. The optimized geometry can be found in Figure 4.14. The geometry is shown for two different color bars. The left sub-figure has he same color range as the 2D mechanisms, allowing for a good comparison. The right sub-figure has a slightly different scale, which amplifies the differences between the cross-sectional areas. The first thing to notice is that the left and right side are not sized the same. This could be explained by the fact that the loading is not acting in the middle of the chord. Also, similar to the 2D cases, the upper members are relatively large. Finally, the 3 elements connecting the left side of the mechanism with the right side have a small cross-sectional area. This confirms the primary role of these elements, i.e. preventing the additional degrees of freedom, rather than carrying the aerodynamic load. This could also explain why the 3D mechanism weights 48.0 [kg], which is more than twice the weight of a 2D mechanism. For 2D the aerodynamic loading was divided by 2 and two mechanisms would be needed to carry the aerodynamic load. The weight of a single mechanism in 2D ranged from 15.0 to 20.0 [kg]. Hence for the full aerodynamic load the total weight for the mechanisms would range from 30.0 to 40.0 [kg]. Comparing this to the 48.0 [kg] found for the 3D mechanism, the 3D mechanism is slightly heavier.

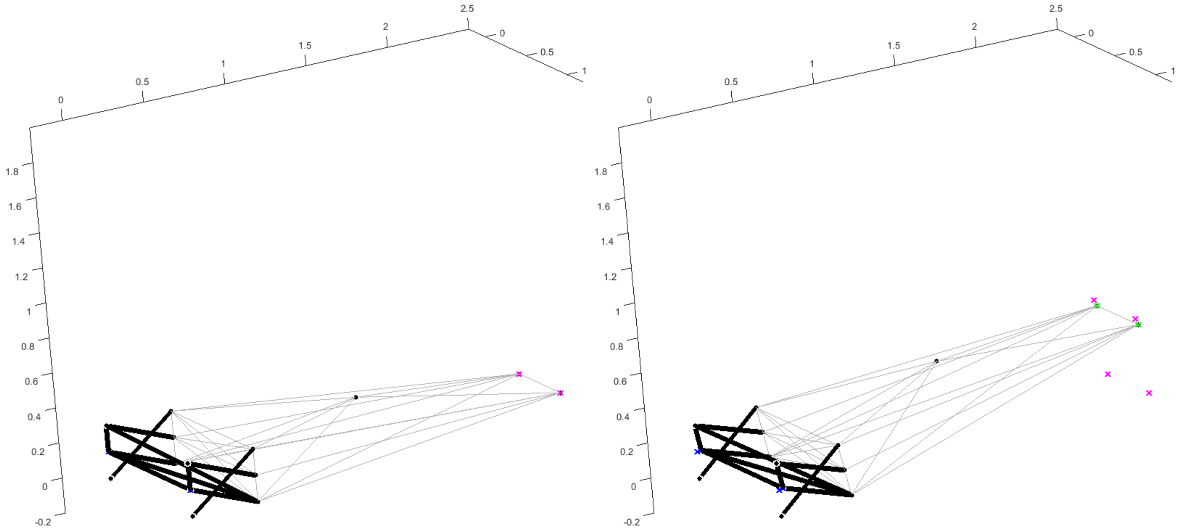

(a) Step 1

(b) Step 2

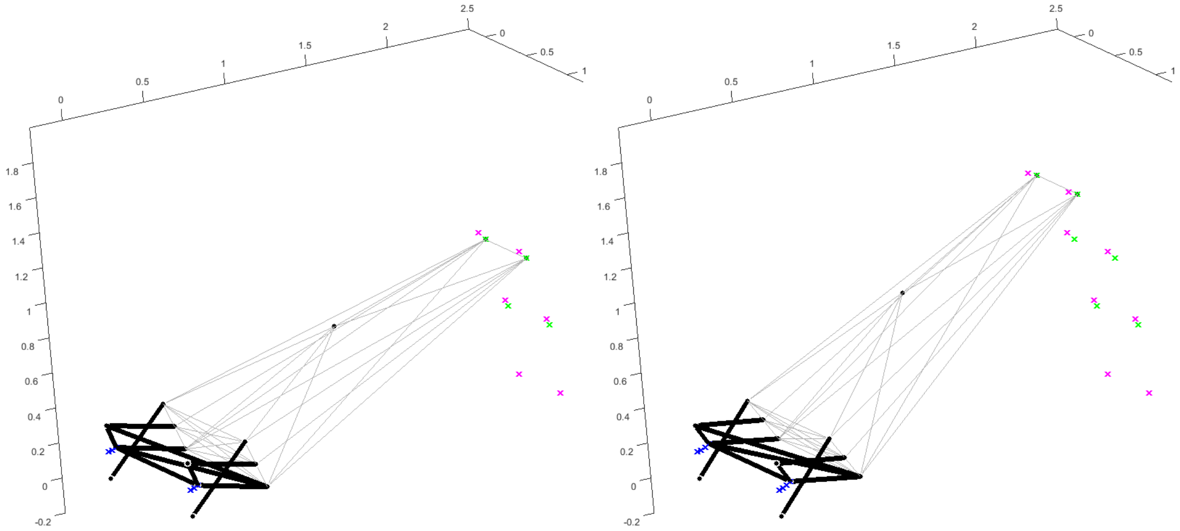

(c) Step 3

(d) Step 4

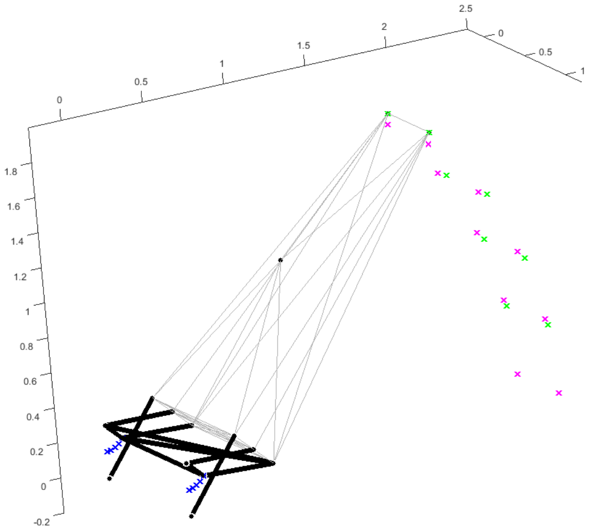

(e) Step 5

Figure 4.12: Actuation of 3D winglet 1 with the input trajectory (blue) and the target output trajectory (pink). The actual location of the output nodes is indicated in green if it lies within the bounding box and red if it lies outside the bounding box.

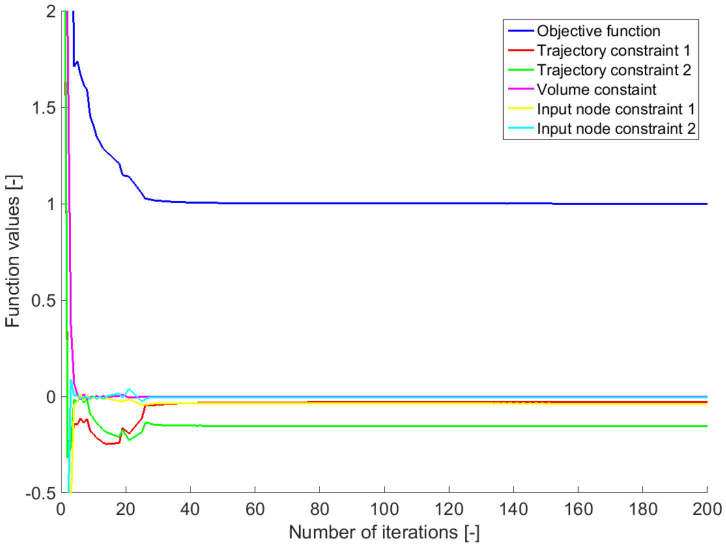

Figure 4.13: Optimization history of mechanism design for 3D winglet, mechanism 1

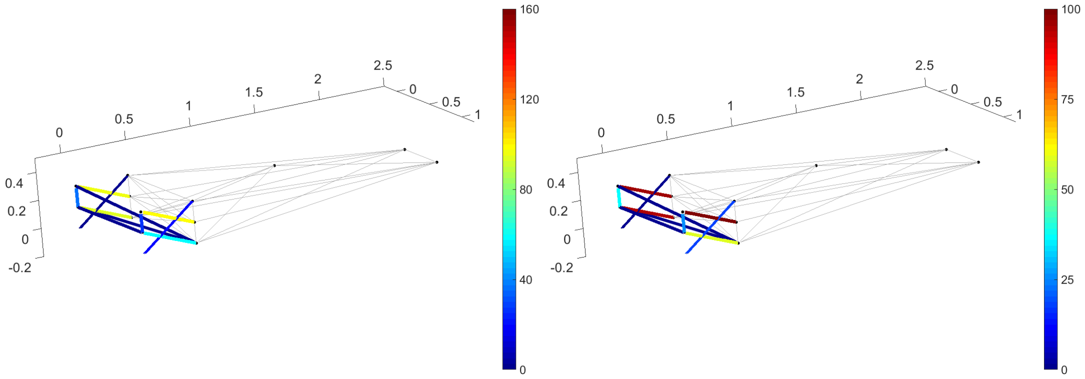

(a) Color bar from 0 to 160 cm^2

(b) Color bar from 0 to 100 cm^2

Figure 4.14: Converged 3D winglet mechanism 1 after sizing. The colors give the cross-sectional areas in [cm^2].

The optimization history of the sizing is given in Figure 4.15. Similar to the 2D, global buckling is the critical buckling mode. All the buckling constraints become less negative with decreasing weight, which is expected. In the first sub-figure the objective function can be seen. The weight decreases and reaches a minimum weight of 48.0 [kg]. In the second and third sub-figures the critical buckling mode can be seen. The other failure modes are not critical.

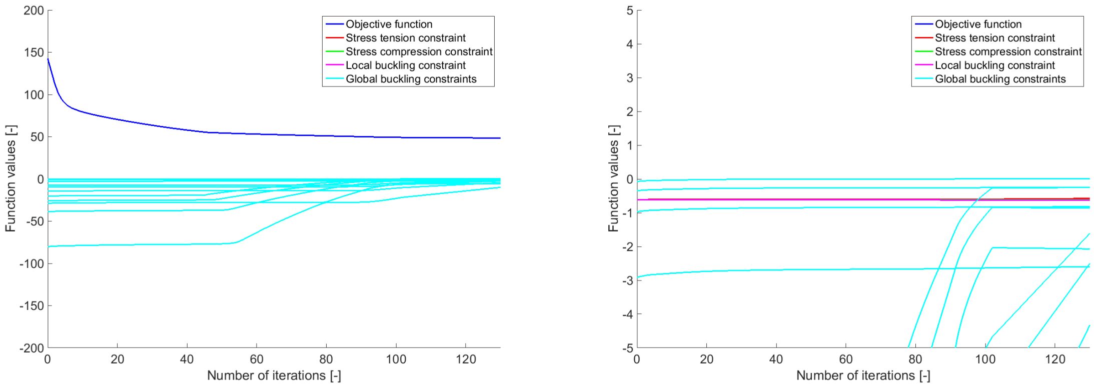

(a) Mechanism 1

(b) Mechanism 1 zoom 1

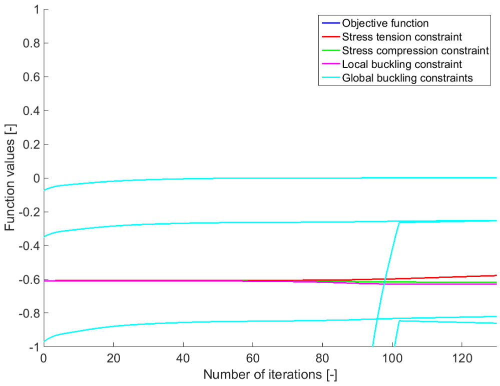

(c) Mechanism 1 zoom 2

Figure 4.15: Optimization history of mechanism sizing for 3D winglet, mechanism 1

For the second mechanism in 3D different trajectories were specified for the output nodes. For the first output node a 45 degrees rotation was specified. This is the same as done for the previous mechanisms. However, for the second output node 55 degrees rotation is specified. The result of these trajectories would yield a mechanism which both changes its cant angle as well as its toe angle during the actuation. The result obtain is given in Figure 4.16. The mechanism consists of 13 elements. How the mechanism deflects is given in 5 steps. As can be seen, the mechanism indeed changes the toe angle during the actuation. It was found that the maximum toe angle was 15 degrees. This is more than the difference between the 45 and 55 degrees, but that can be explained by the presence of the bounding box.

In blue the trajectories of the input nodes are given, in pink the target output node trajectories. The actual location of the output nodes are plotted in green when it falls within the bounding box, or in red when it lies outside of it. As can be seen in steps 3, 4, and 5 only the second output node lies outside the bounding box. This is possible, since only on average the output nodes should lie within these boxes.

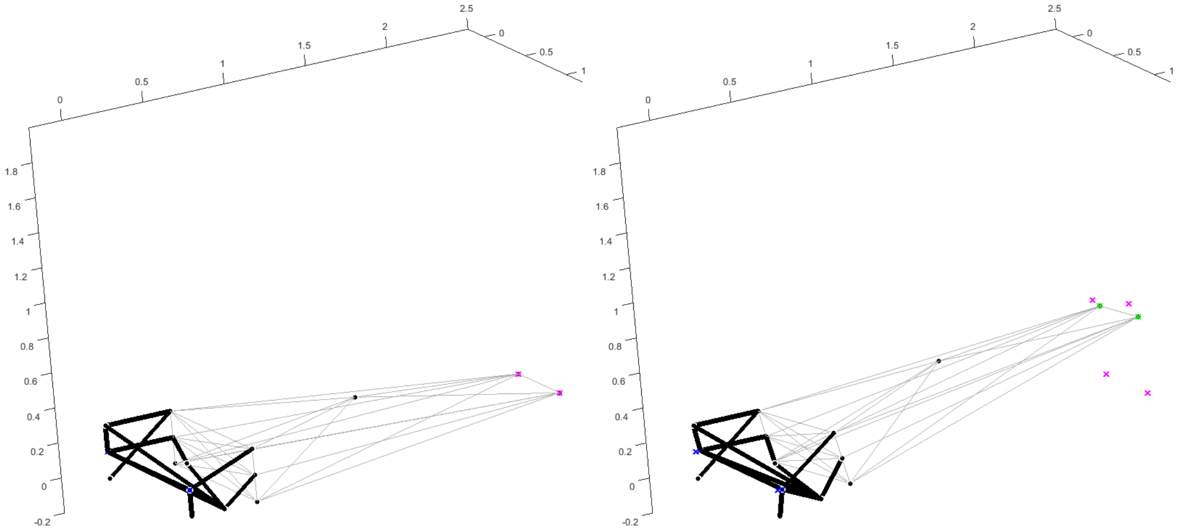

(a) Step 1 (b) Step 2

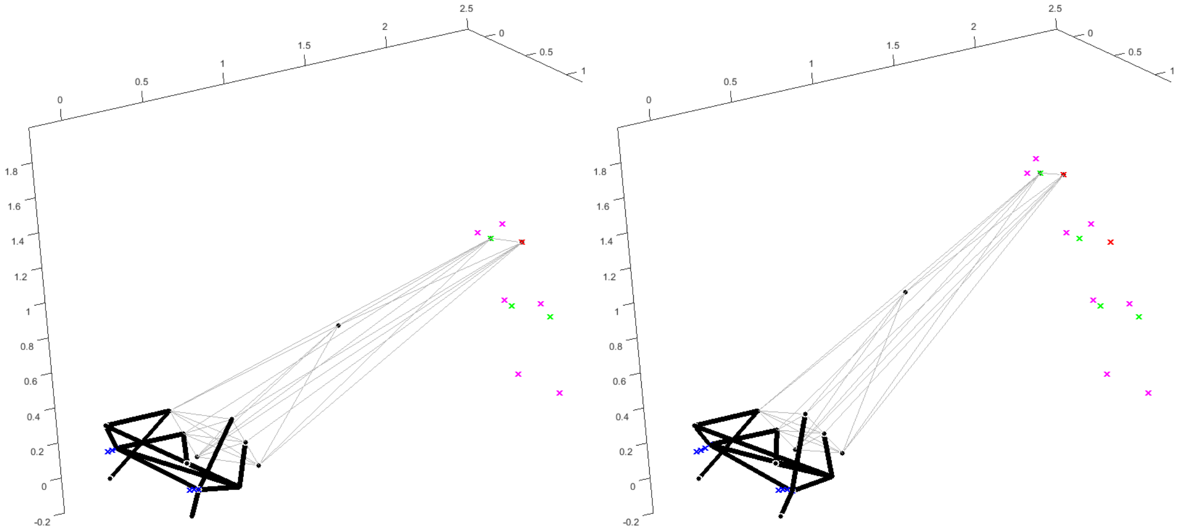

(c) Step 3 (d) Step 4

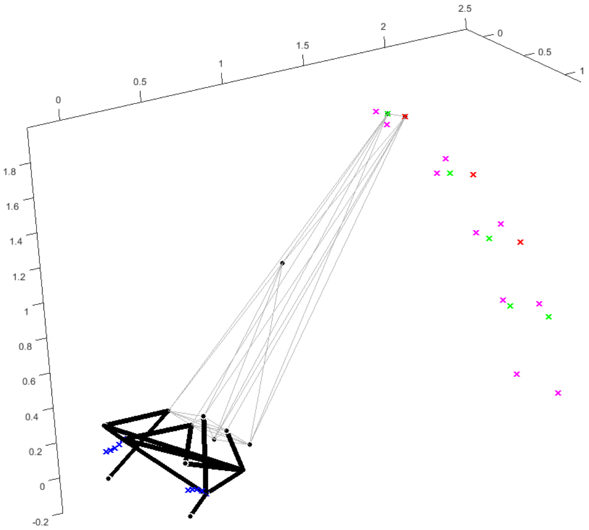

(e) Step 5

Figure 4.16: Actuation of 3D winglet 2 with the input trajectory (blue) and the target output trajectory (pink). The actual location of the output nodes is indicated in green if it lies within the bounding box and red if it lies outside the bounding box.

The optimization history is given in Figure 4.17. As done for every mechanism design, the objective function converges to 1. Interesting to note is that trajectory constraint for output node 1 is not active, which it is active for output node 2. This could also be seen from Figure 4.16. Output node 1 lies in each step within the bounding box. As a result the constraint cannot be active. The volume constraint (10 elements) is active. This volume is distributed among the 13 members of the mechanism, as a result not every member has ρ_i equal to 1. This explains why an input node constraint is active, while after post-processing more than 2 elements are present.

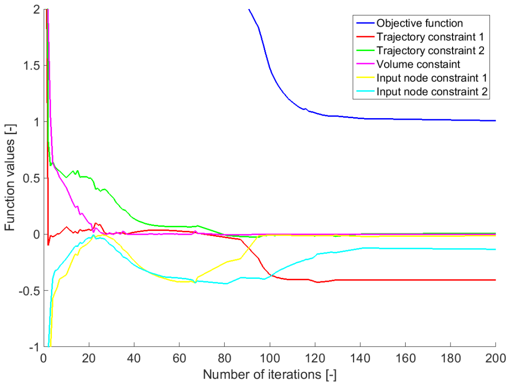

Figure 4.17: Optimization history of mechanism design for 3D winglet, mechanism 2

Now that the topology is known, the minimum weight can be determined. The sizing optimization has been performed and the results are given in Figure 4.18. The weight was found to be 102.7 [kg]. This is significantly higher than the weight calculated for the first 3D mechanism. This can be understood when inspecting the geometry in more detail. The mechanism is much more complicated than the mechanism which only regulates the cant angle. Due to the toe angle, the aerodynamic loading rotates out of plane, this results in an out of plane force, which can not be carried efficiently by the mechanism. In addition, the force also induces a torque, complicating the load case even further. As a result the geometry turned out to be quite sensitive to buckling. An interesting observation is how the different elements are sized. Most of the material is concentrated at one side of the mechanism, this in contrast to the previous mechanism. Hence the twist in the mechanism greatly influences what the final geometry looks like. Also, the optimization history provides insight in why this mechanism is heavier than the previous one found. In figure 4.18 the optimization history can be found. By zooming in on the constraints, it can be observed that the local buckling constraint becomes the critical buckling mode. Hence a different failure mode drives this geometry. By combining all local buckling constraints into a single Kreisselmeier-Steinhauser function, this constraint will always be more conservative. This means that the new constraint will always be more strict than the individual local buckling constraints. Once this constraint becomes active and thereby prevents additional weight reduction, the actual structure will not fail in local buckling. By using the Kreisselmeier-Steinhauser function and this constraint is active, a more conservative (i.e. higher) weight is obtained for the mechanism. Another possible explanation could be the non-convexity in the design space. This means that several local minima exist, of which one is found. Multiple runs have been performed, but did not yield a lower weight that given here. However, it could be that the lowest weight is not yet found. Also for 2D multiple runs were performed, but the vast majority of the runs did find the same weight. The increased size of the design space for 3D mechanisms makes it more difficult to find the global minimum.

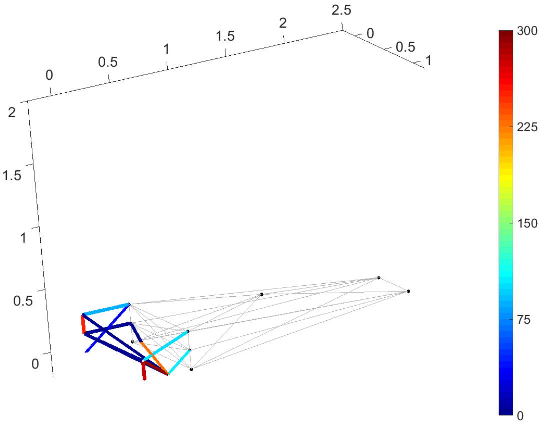

Figure 4.18: Converged 3D winglet mechanism 2 after sizing. The colors give the cross-sectional areas in [cm^2].

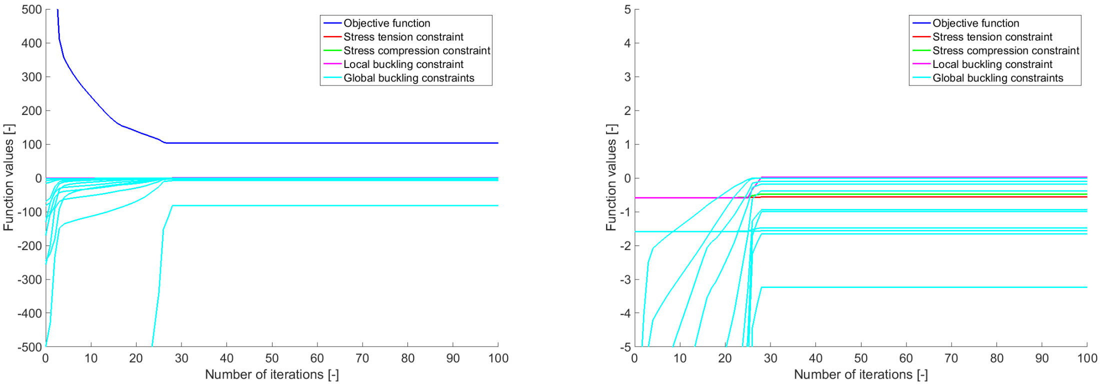

(a) Mechanism 2 (b) Mechanism 2 zoom

Figure 4.19: Optimization history of mechanism sizing for 3D winglet, mechanism 2

Finally, the difference in trajectory between mechanism 1 and 2 are illustrated in Figure 4.20. A 2D view of the mechanisms is shown. In blue the input trajectories are plotted and in pink the target output trajectories. In Figure 4.20a mechanism 1 is shown. As was already mentioned earlier in this chapter, mechanism 1 could be interpreted as 2 mechanisms, each one acting on the sides of the winglet. These two mechanisms are identical, resulting in the same input trajectory (which coincide in this figure) for both input nodes. Also, the same output trajectory was specified for both output nodes. When looking at the output nodes, these coincide in the figure as well, which confirms that mechanism 1 only changes the cant angle. When looking at mechanism 2 (Figure 4.20b), a different behavior is observed. The trajectories for the input nodes are different. Also the output trajectories differed, as previously explained. Interesting to note is that the output nodes do not coincide for mechanism 2, this clearly illustrates the toe angle. Hence, mechanism 2 influences both the cant angle as well as the toe angle.

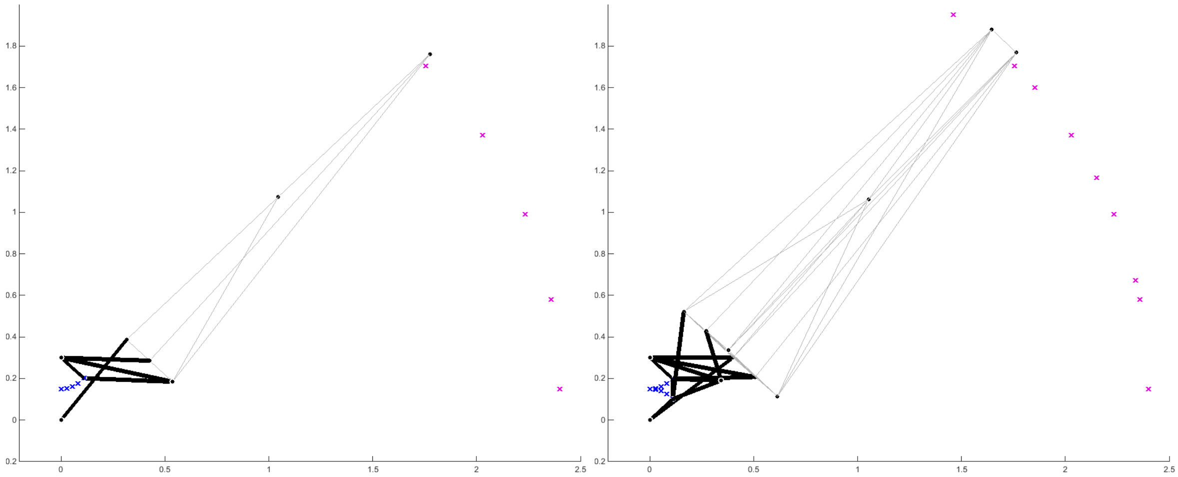
(a) Mechanism 1 with cant angle (b) Mechanism 2 with cant angle and toe angle

Figure 4.20: 2D view of 3D winglet mechanisms

4.3. TRADE-OFF

In the previous two sections the mechanisms for the 2D and 3D winglet were presented. In 2D 4 mechanisms were found, in 3D 2 mechanisms were given. In this section a trade-off is made between these various mechanisms. This will be done by comparing both the weight of the mechanisms and the efficiency. The efficiency is defined as the output work divided by the input work. At the input node(s) a displacement is prescribed, which requires a certain actuation force for equilibrium. The total input work is the average actuation force multiplied with the maximum actuation displacement. For all these mechanisms the input nodes were displaced over a distance of 0.11 meters. The actuation has been done in 100 steps to obtain an accurate average reaction force. The actuation forces are different for the various mechanisms. Part of the input work is used to carry the aerodynamic loading and to deflect the winglet, some energy is 'lost' by straining the members and is stored as strain energy. This energy will be released when unloaded, but it can not be used to deflect the winglet. Hence the ratio given by Equation 4.6 gives the efficiency for a mechanism:

$$\eta = \frac{W_{out}}{W_{in}} = \frac{W_{in} - U}{W_{in}} = 1 - \frac{U}{W_{in}} \tag{4.6}$$

Here it is assumed that no fiction is present in the hinges. The only efficiency losses occur due the strain energy of the truss members. To calculate the output work is challenging, since the aerodynamic force is not always perfectly perpendicular to winglet's surface. The aerodynamic force rotates with the same angle as the target output trajectory. The actual angle of the winglet could be slightly different, due to the bounding boxes specified for the trajectory. Therefore it has been decided to calculated the aerodynamic efficiency by calculating the strain energy (i.e. the energy loss) and calculate the mechanism efficiency using this energy loss.

Ideally, the mechanism is as light as possible and has the highest efficiency. Both factors are favorable and therefore preferred. The lighter the mechanism itself, the lighter the aircraft will be. This will result in a lower fuel consumption. For a given aerodynamic loading, the higher the efficiency the lower the input work required. The lower the input work, the smaller the actuator can be, which on its turn also results in a lower weight. For the different mechanisms the weight of the mechanisms (which excludes the actuator weight) is plotted versus the efficiency. To compare the 2D mechanisms with the 3D mechanisms, the weight of the 2D mechanisms is multiplied with a factor 2, since half the aerodynamic load was assumed to act on a 2D mechanism. The results can be found in Figure 4.21. The mechanisms 1, 2, 3, and 4 in 2D are denoted 2D1, 2D2, 2D3, and 2D4 respectively. In 3D the mechanisms are denoted as 3D1 and 3D2.

Interesting to note is that the 2D mechanisms are lower in weight than the 3D mechanisms. This can be explained by the fact that some elements in 3D are only present to prevent additional degrees of freedom in the mechanisms, while they carry hardly any load. Also, in 3D the aerodynamic loading acts at a quarter chord, resulting in a torsional moment. This gives a more complicated load case, which could also explain the increased weight. It must be noted that the weight optimization uses a simplified aerodynamic loading. A more advanced model of the loading could change the weight calculations for the various mechanisms. Further research would be required to obtain detailed weight estimations. Also, the actuator weight should then be taken into account.

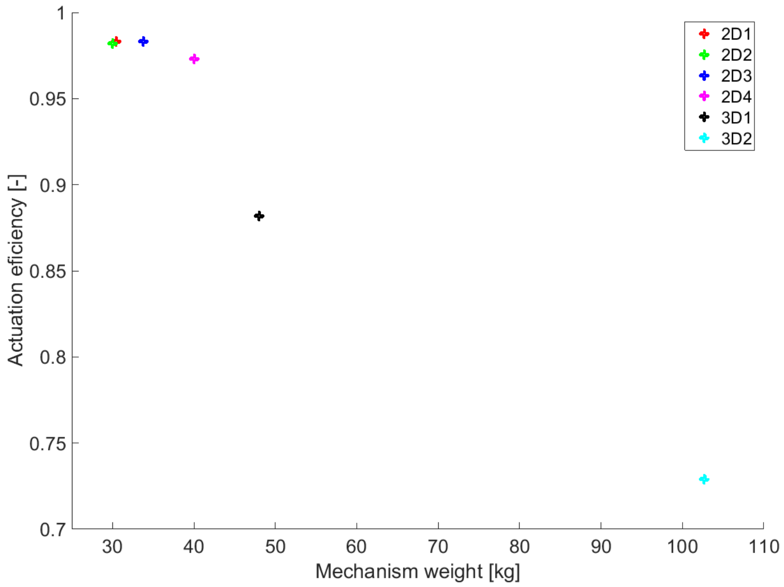

Figure 4.21: Winglet mechanisms trade-off, actuation efficiency versus mechanism weight. The weight of 2D mechanisms is multiplied with 2.

The efficiencies of the 2D mechanisms are very high, ranging between 97.3% and 98.3%. For these mechanisms only 1-2% is lost in the deformation of the mechanisms. This means that most of the input work is used to deflect/actuate the mechanism rather than to strain the elements. These high efficiencies are expected, since only energy is lost in the axial deformation of the truss members. In contrast to compliant mechanisms, where thin regions of the mechanisms are strained during actuation, no strain energy is stored in the hinges of the articulated mechanisms. When looking at 3D, the first mechanism also has a high efficiency of 88.2%. However, for the second mechanism an efficiency of 72.9% was found. This means that more than 25% of the energy that is put into the mechanism is stored as strain energy. Comparing the two mechanisms in 3D, the more complicated the trajectory of the winglet, the lower the efficiency. Additional 3D mechanisms will have to be examined to see whether this is true in general. To better understand why the efficiency of mechanism 3D2 is lower, a wireframe of the mechanism is shown before and after aerodynamic loading in Figure 4.22. As can be seen in the left sub-figure, the aerodynamic loading deflects the geometry. When zooming in on the mechanism, the elements experience a significant strain. As a consequence of these strains, the efficiency reduces.

Based on the results from Figure 4.21, the mechanisms 1 and 2 in 2D perform the best. These have the lowest weight and the highest efficiency. These mechanisms have an additional advantage when considering the morphing skin. The skin could fit between the upper and lower nodes of the mechanism, without any contact with the mechanism. This contact would increase the friction and results in additional wear of the skin. This should be taken into account for mechanism 4 for example. In 3D the mechanisms were found to be heavier, but there is an opportunity to design mechanisms with more complex trajectories.

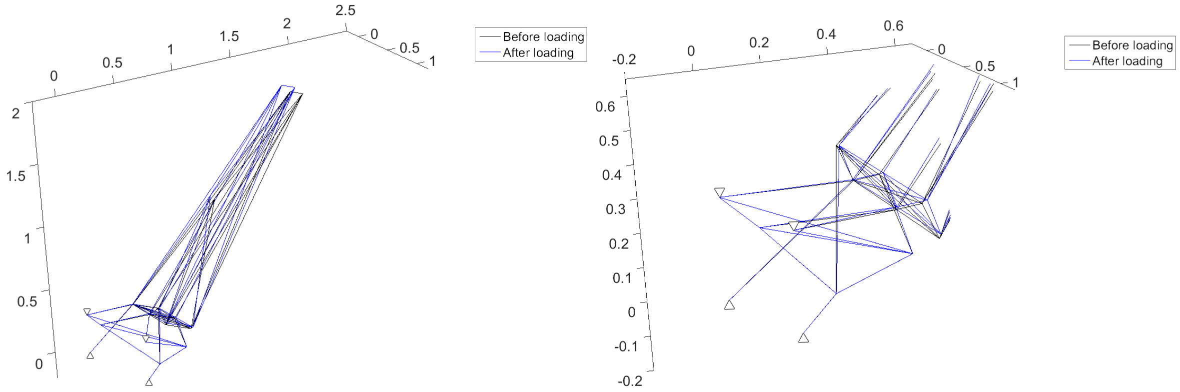

(a) Entire geometry (b) Zoomed in on mechanism

Figure 4.22: Mechanism 3D2 before (black) and after (blue) aerodynamic loading, last actuation step

5

CONCLUSIONS AND RECOMMENDATIONS

In Chapter 1 the following research objective was specified:

> *"Developing a software tool to design a mechanism for morphing winglets, using ground-structure based topology optimization, by improving, extending, and expanding the previous 2D inhouse tool."*

Based on this objective the following research goals were defined:

1. Improve previous tool
    (a) Increase robustness
    (b) Reduce computational time
    (c) Increase separation
2. Extend previous tool
    (a) Include multiple input nodes
    (b) Include multiple output nodes
    (c) Include buckling
3. Expand previous tool
    (a) Expand to 3D

In the Chapters 2 and 3 the tool developed in this thesis was discussed in detail. In Chapter 4 the results obtained from this tool were included. In this chapter will be discussed to what extend the tool meets the research goals. The conclusions are discussed in Section 5.1, the recommendations for future research will be covered in Section 5.2.

5.1. CONCLUSIONS

A tool for the design of articulated mechanisms was developed. It consists of two optimization steps, which was illustrated in Figure 1.5. The first optimization, mechanism design, focused on finding the topology for the mechanism to perform the specified trajectory. Once the topology was found, the second optimization sized the individual elements to obtain the minimum weight, while preventing failure. For this thesis mechanisms for morphing winglets were designed, both in 2D and in 3D.

The conclusions can be categorized into three. The first category contains the conclusions related to the improvements of the tool, the second covers the extensions and the third covers the conclusions related to the expansion.

5.1.1. IMPROVEMENTS

In the mechanism design the objective function was changed to one including compliance and the sum of the reaction forces at the input nodes squared. By selecting this objective, the optimizer tries to minimize the reaction forces at the input nodes and the compliance. The reaction forces will therefore be steered toward zero, yielding a mechanism. As a result, the trajectory will be performed without straining the elements needed for the topology. If elements would be strained, then the reaction force at the input nodes would be non-zero.

The compliance term was included to improve the separation, once a mechanism was found. By minimizing the compliance, for constant forces, the stiffness of the mechanism is maximized. Hence the compliance term promotes 0/1 solutions. Therefore, the current tool improves the separation.

Also, by minimizing the compliance, the degrees of freedom are automatically regulated. The mechanism will have the minimum number of degrees of freedom needed to perform the trajectory, due to the term containing the reaction forces. By including the compliance term, the optimizer will prevent any additional degrees of freedom in the mechanism. If an additional degree of freedom would be present, then one or more nodes would experience large displacements. With the minimum compliance term these displacements are minimized.

Another advantage of the compliance term is the opportunity to remove the incremental load increase in the previous tool. The incremental load increase was included to improve the separation, which is already promoted via the compliance term. By removing the incremental load the robustness of tool is improved. The previous tool experienced optimization which did not converge as a result of the incremental load increase, which is now improved. Another advantage of the removal of the incremental load is the improved computational time. In the previous tool for each load increment an optimization is performed, which considerably impacts the computational time.

Finally, in the previous tool the degrees of freedom were regulated with two additional load cases, each with a disturbance force. By minimizing the error between the target and actual trajectory for all three load cases, the best solution is the one where the disturbance forces do not affect the output trajectory. Hence, these additional load cases prevented more degrees of freedom that needed for the trajectory. The current tool has an objective which automatically regulates the degrees of freedom, thereby eliminating the need of two additional load cases. This resulted in a significant reduction in computational time.

With the current objective function the tool's robustness was increased, the computational time was reduced, and the separation was improved. Therefore it could be concluded that the tool was successfully improved.

5.1.2. EXTENSIONS

The next step was to extend the tool's capabilities. The previous tool was only able to include a single input node and a single output node. The current tool is able to have multiple input and output nodes. The number of input nodes and output nodes can be chosen freely. For each input node and output node a constraint is specified for the mechanism design. For the input node at least two elements should be attached, while for every output node a trajectory is specified. In the previous chapter different examples can be found where two input nodes and two output nodes were included in the design.

The previous tool sized the elements with a linear finite element analysis, only taken into account yielding as a failure mode. In each step an analysis was performed to find the cross-sectional area's, then for each element the largest cross-sectional area from all steps is selected. This does not necessarily give the lightest design, and does not account or buckling. Hence, the current tool included a second optimization, where the minimum weight was defined as the objective function, and various failure modes were included as constraints. The constraints prevent material failure in tension and compression, local buckling of the individual truss members, and global buckling.

The current tool is now compatible with multiple input and output nodes. Also, local and global buckling were included during the sizing. Therefore, it can be concluded that the tool's capabilities are successfully extended.

5.1.3. EXPANSION

Also, the tool should be expanded to 3D for practical applications. The changes required for 3D were limited to the analysis part. These changes were implemented and verified. Therefore it can be concluded that the tool was successfully expanded to 3D. Various 3D mechanisms for the winglet were found. By expanding the tool to 3D, the winglet deflection is no longer limited to 2D. Where the mechanism for the winglet in 2D is only able to is able to regulate the cant angle, the mechanism for the 3D winglet is able to regulate both the cant angle and the toe angle.

It can be concluded that the tool is successfully improved, extended, and expanded. The tool meets all the specified research goals, thereby meeting the overall research objective. The current tool successfully designed and sized 2D and 3D mechanisms. In 2D 4 different mechanisms were found, where the mechanisms 1 (2D1) and 2 (2D2) were found to perform the best. A trade-off was made on the mechanism efficiency and weight. For mechanisms 2D1 a weight of 15.2 [kg] and an efficiency of 98.3% was found. For 2D2 a weight of 15.0 [kg] and an efficiency of 98.2% was found. In 3D the mechanisms were found to be heavier (minimum weight was found to be 48.0 [kg]), but were able to perform more complex trajectories. Mechanism 3D2 was able to both regulate the cant angle as well as the toe angle. A variation in toe angle of up to 15 degrees was found.

5.2. RECOMMENDATIONS

In the future several aspects can be researched in more detail. These aspects can be categorized into two, the first would cover the recommendations within the scope defined for this thesis (internal), the second would be beyond this scope (external).

5.2.1. INTERNAL

In the current tool only the cross-sectional areas of the elements were used in the optimizer as design variables. The nodal locations could also be included to increase the flexibility of the tool. In that case the design vector would consist of both cross-sectional areas as well as nodal locations. This also means that the sensitivities of objective functions and constraints with respect to the nodal locations have to be determined.

Currently, only aluminum 2024-T3 is considered in the sizing optimizations. It would be interesting to see how different materials (with different yield stress, Young's modulus and density) would impact the weight of the mechanisms. Also combining different materials for different elements would be interesting to look at, since the current tool assumes the same material for all elements. Related to this, composites could also be considered in the design of these mechanisms. Since the truss members are only axially loaded, possible weight savings could be obtained when using composites.

Also, the design space of the test cases in this thesis were in 2D limited to 9 nodes and in 3D limited to 18 nodes. It is worth considering larger design spaces, where mechanisms might be found with a more continuous transition between the wing and the winglet. An example would be the hyper-elliptic cambered span (HECS) wing from NASA, where a very continuous transition can be observed. In this thesis the shape of the winglet does not change, for future research additional actuators could be considered within the winglet, allowing for a more advanced actuation.

In addition, in the current tool no fatigue is considered. The deflection of the winglet would be very repetitive. Assuming that for each flight the winglet will deflect once up and down, at least one cycle is performed for each flight. This will result in several thousands of cycles, which might become critical. An additional constraints for fatigue could be included.

Finally, in 3D it might be possible for elements to intersect. In 2D this would not be a problem, since an offset could be given in the third dimension. However in 3D this is not possible, which might result in mechanisms which are non-feasible. In the test cases this behavior was not observed, but this might be possible for more complex mechanisms. To solve this, the research done by Santer et. al. [50] might be useful. They incorporated this constraint to guarantee manufacturability.

5.2.2. EXTERNAL

Beyond the scope of the current research objective, one could consider a more accurate representation of the loading. Currently, this is simplified to a constant point load, acting in the middle of the winglet. Improvements could be a distributed loading or a loading that changes over time. Also, the aeroelasticity could be considered. Currently, the stiffness is not affected by he aerodynamic loading. When a more accurate loading is considered for the winglet, the structural representation of the winglet could also be improved. This is currently modeled as a structure, consisting of truss members. By modeling the winglet with aerodynamic profiles, the aeroelastic behavior will be more accurate. By incorporating this, the load introduction into the mechanism will also be more accurate. As a result, a more accurate weight optimization can be performed.

Also, the current weight optimization only takes the weight of the mechanism into account. The weight of the actuator is not included. An improved weight optimization also includes the weight of the actuator, which could be estimated based on the force-displacement requirements on the input nodes. In the current tool the weight of the mechanism is minimized, which also impacts the efficiency. Therefore, it might be possible that the minimum weight of the mechanism does not yield the minimum weight of the entire system, including the actuator.

In addition, the current tool is only verified. It would be interesting to validate the results. This can be done by manufacturing the mechanism and perform experiments. Other experiments in the wind tunnel, with a more accurate representation of the winglet, are also possible.

Given the general applicability of the tool, other applications can be considered as well. In this thesis only mechanisms for morphing winglets are designed and sized. The tool can also be used to design mechanisms for morphing leading edges, trailing edges, or even entire wing structures.

Also, the research objective was focused on the design of mechanisms for morphing winglets. The skin between the wing and the winglet, where the mechanism will be positioned, will experience large deformations. Additional research is needed on how the skin should be designed. Topology optimization can also be used to design morphing skins [29, 46], which could be used to design this part of the wing skin.

Finally, some remarks considering the manufacturability. During manufacturing some imperfections in the members could be introduced. This could decrease the performance of the geometry. Hence buckling could be considered with members which have initial imperfections. In addition, additional research would be needed on the design of the joints. Especially in 3D these joints could be challenging. Some sort of ball and socket joint might be needed.

BIBLIOGRAPHY

[1] D. Baker and M. I. Friswell. Determinate structures for wing camber control. *Smart Materials and Structures*, 18(3):1–13, 2009.

[2] K.-J. Bathe. *Finite Element Procedures in Engineering Analysis*. Prentice Hall, Upper Saddle River, New Jersey, 1982.

[3] M. P. Bendsøe. Optimal shape design as a material distribution problem. *Structural Optimization*, 202:193–202, 1989.

[4] M. P. Bendsøe and N. Kikuchi. Generating optimal topologies in structural design using a homogenization method. *Computer Methods in Applied Mechanics and Engineering*, 71(2):197–224, 1988.

[5] P. Bourdin, A. Gatto, and M. I. Friswell. The Application of Variable Cant Angle Winglets for Morphing Aircraft Control. In *24th Applied Aerodynamics Conference*, San Francisco, California, 2006.

[6] P. Bourdin, A. Gatto, and M. I. Friswell. Potential of Articulated Split Wingtips for Morphing-Based Control of a Flying Wing. In *25th AIAA Applied Aerodynamics Conference*, Miami, FL, 2007. American Institute of Aeronautics and Astronautics, Inc.

[7] P. Bourdin, A. Gatto, and M. I. Friswell. Aircraft Control via Variable Cant-Angle Winglets. *Journal of Aircraft*, 45(2):414–423, 2008.

[8] P. Bourdin, A. Gatto, and M. I. Friswell. Performing co-ordinated turns with articulated wing-tips as multi-axis control effectors. *Aeronautical Journal*, 114(1151):35–47, 2010.

[9] P. W. Christensen and A. Klarbring. *An Introduction to Structural Optimization*. Springer, 2009.

[10] M. Crisfield. *Non-Linear Finite Element Analysis*. John Wiley and Sons, New York, vol 1: ess edition, 1997.

[11] A. De Gaspari, S. Ricci, S. Vasista, and H. Monner. Morphing Devices for a Wing and Wingtip Based on Compliant Structures. In *4th EASN Association International Workshop on Flight Physics & Aircraft Design*, Aachen, Germany, 2014.

[12] J. D. Deaton and R. V. Grandhi. A survey of structural and multidisciplinary continuum topology optimization : post 2000. *Structural and Multidisciplinary Optimization*, 49:1–38, 2014.

[13] P. Eberhard and K. Sedlaczek. Grid-Based Topology Optimization of Rigid Body Mechanisms. In *III European Conference on Computational Mechanics*, 2006.

[14] J. Eves, V. V. Toropov, H. M. Thompson, P. H. Gaskell, J. J. Doherty, and J. Harris. Topology Optimization of aircraft structures with non-conventional configurations. In *8th World Congress on Structural and Multidisciplinary Optimization,*, Lisbon, Portugal, 2009.

[15] L. Falcão, A. A. Gomes, and A. Suleman. Multidisciplinary Design Optimisation of a Morphing Wingtip. In *2nd International Conference on Engineering Optimization*, Lisbon, Portugal, 2010.

[16] L. Falcão, A. A. Gomes, and A. Suleman. Aero-structural Design Optimization of a Morphing Wingtip. *Journal of Intelligent Material Systems and Structures*, 22(July):1113–1124, 2011.

[17] L. Falcão, A. A. Gomes, and A. Suleman. Design and Analysis of an Adaptive Wingtip. In *52nd AIAA/ASME/ASCE/AHS/ASC Structures, Structural Dynamics and Materials Conference*, 2011.

[18] M. I. Friswell. The prospects for morphing aircraft. In *IV ECCOMAS Thematic Conference on Smart Structures and Materials*, Porto, Portugal, 2009.

[19] M. I. Friswell, J. E. Herencia, D. Baker, and P. M. Weaver. The optimisation of hierarchical structures with applications to morphing aircraft. In *Second International Conference on Multidisciplinary Design Optimization and Applications*, Gijon, Spain, 2008.

[20] C. F. Gerald and P. O. Wheatley. *Applied Numerical Analysis (7th edition)*. Pearson, 2003.

[21] E. Gillebaart and R. De Breuker. Optimisation of a mechanical linkage for a morphing winglet. In *Proceedings of the DeMEASS VI Conference*, Ede, The Netherlands, 2014.

[22] A. A. Gomes, L. Falcão, and A. Suleman. Optimisation of multistable composites for morphing wingtips. In - *8th World Congress on Structural and Multidisciplinary Optimization*, Lisbon, Portugal, 2009.

[23] A. A. Gomes, L. Falcão, and A. Suleman. Study of an Articulated Winglet Mechanism. In *54th AIAA/ASME/ASCE/AHS/ASC Structures, Structural Dynamics, and Materials Conference AIAA*, Boston, MA, 2013. American Institute of Aeronautics and Astronautics, Inc.

[24] J. C. Gomez and E. Garcia. Morphing unmanned aerial vehicles. *Smart Materials and Structures*, 20(10):16, 2011.

[25] J. K. Guest, J. H. Prévost, and T. Belytschko. Achieving minimum length scale in topology optimization using nodal design variables and projection functions. *International Journal for Numerical Methods in Engineering*, 61:238–254, 2004.

[26] IANS. *Airbus Military launches improved C295W transport for India*, 2013 (accessed February 11, 2016).

[27] D. Inoyama, B. P. Sanders, and J. J. Joo. Conceptual design and multidisciplinary optimization of in-plane morphing wing structures. *Proceedings of SPIE*, 01(1):1–11, 2006.

[28] D. Inoyama, B. P. Sanders, and J. J. Joo. Topology Optimization Approach for the Determination of the Multiple-Configuration Morphing Wing Structure. *Journal of Aircraft*, 45(6):1853–1862, 2008.

[29] J. J. Joo, G. W. Reich, and J. T. Westfall. Flexible Skin Development for Morphing Aircraft Applications via Topology Optimization. *Journal of Intelligent Material Systems and Structures*, 20(November):1969–1985, 2009.

[30] A. Kawamoto. *Generation of Articulated Mechanisms by Optimization Techniques*. PhD thesis, Technical University of Denmark, 2004.

[31] A. Kawamoto. Path-generation of articulated mechanisms by shape and topology variations in non-linear truss representation. *International Journal for Numerical Methods in Engineering*, 64(12):1557–1574, 2005.

[32] A. Kawamoto, M. P. Bendsøe, and O. Sigmund. Articulated mechanism design with a degree of freedom constraint. *International Journal for Numerical Methods in Engineering*, 61(9):1520–1545, 2004.

[33] A. Kawamoto, M. P. Bendsøe, and O. Sigmund. Planar articulated mechanism design by graph theoretical enumeration. *Structural and Multidisciplinary Optimization*, 27(4):295–299, 2004.

[34] A. Kawamoto, T. Matsumori, S. Yamasaki, T. Nomura, T. Kondoh, and S. Nishiwaki. Heaviside projection based topology optimization by a PDE-filtered scalar function. *Structural and Multidisciplinary Optimization*, 44:19–24, 2011.

[35] S. I. Kim and Y. Y. Kim. Topology optimization of planar linkage mechanisms. *International Journal for Numerical Methods in Engineering*, 98(February):265–286, 2014.

[36] M. Kintscher, H. P. Monner, and O. Heintze. Experimental Testing of a Smart Leading Edge High Lift Device for Commercial Transportation Aircrafts. In *27th International Icongress of the aeronautical sciences*, Nice, France, 2010.

[37] M. H. Kobayashi. On a biologically inspired topology optimization method. *Communications in Nonlinear Science and Numerical Simulation*, 15(3):787–802, 2010.

[38] G. Kotucha and K. Hackl. Density gradient based regularization of topology optimization problems. *Proceedings in Applied Mathematics and Mechanics*, 5(1):423–424, 2005.

[39] K. J. Lu and S. Kota. Design of Compliant Mechanisms for Morphing Structural Shapes. *Journal of Intelligent Material Systems and Structures*, 14(June):379–390, 2003.

[40] K. J. Lu and S. Kota. An Effective Method of Synthesizing Compliant Adaptive Structures using Load Path Representation. *Journal of Computational Science and Technology*, 16(April):307–317, 2005.

[41] A. Mauchle, R. De Breuker, and J. Simpson. Design and demonstration of a leading edge actuation system through topology optimisation. In *23rd International Conference on Adaptive Structures and Technologies (ICAST)*, pages 418–429, Nanjing, China, 2012, 2012.

[42] M. D. Maughmer, T. S. Swan, and S. M. Willits. Design and Testing of a Winglet Airfoil for Low-Speed Aircraft. *Journal of Aircraft*, 39(4):654–661, 2002.

[43] K. Maute and M. Allen. Conceptual design of aeroelastic structures by topology optimization. *Structural and Multidisciplinary Optimization*, 27(1-2):27–42, 2004.

[44] K. Maute and G. W. Reich. Integrated Multidisciplinary Topology Optimization Approach to Adaptive Wing Design. *Journal of Aircraft*, 43(1):253–263, 2006.

[45] C. B. W. Pedersen, T. Buhl, and O. Sigmund. Topology synthesis of large-displacement compliant mechanisms. *International Journal for Numerical Methods in Engineering*, 50:2683–2705, 2001.

[46] G. W. Reich, B. Sanders, and J. J. Joo. Development of Skins for Morphing Aircraft Applications via Topology Optimization. In *48th AIAA/ASME/ASCE/AHS/ASC Structures, Structural Dynamics, and Materials Conference*, Honolulu, Hawaii, 2007.

[47] G. I. N. Rozvany, editor. *Optimization of Large Structural Systems*. Kluwer Academic Publisher, volume ii edition, 1993.

[48] G. I. N. Rozvany. A critical review of established methods of structural topology optimization. *Structural and Multidisciplinary Optimization*, 37(3):217–237, 2008.

[49] M. Sankrithi and J. Frommer. Controllable winglets, 2010.

[50] M. Santer and S. Pellegrino. Topology Optimization of Adaptive Compliant Aircraft Wing Leading Edge. In *48th AIAA/ASME/ASCE/AHS/ASC Structures, Structural Dynamics, and Materials Conference*, Honolulu, Hawaii, 2007.

[51] M. Santer and S. Pellegrino. Topological Optimization of Compliant Adaptive Wing Structure. *AIAA journal*, 47(3):523–534, 2009.

[52] A. Shelton, A. Tomar, J. Prasad, M. J. Smith, and N. Komerath. Active Multiple Winglets for Improved Unmanned-Aerial-Vehicle Performance. *Journal of Aircraft*, 43(1):110–116, 2006.

[53] L. Shili, G. Wenjie, and L. Shujun. Optimal Design of Compliant Trailing Edge for Shape Changing. *Chinese Journal of Aeronautics*, 21:187–192, 2008.

[54] O. Sigmund. On the Design of Compliant Mechanisms Using Topology Optimization. *Mechanics of Structures and Machines: An International Journal*, 25(4):493–524, 1997.

[55] O. Sigmund. Morphology-based black and white filters for topology optimization. *Structural and Multidisciplinary Optimization*, 33(4-5):401–424, 2007.

[56] O. Sigmund and K. Maute. Topology optimization approaches - A comparative review. *Structural and Multidisciplinary Optimization*, 48:1031–1055, 2013.

[57] O. Sigmund and J. Petersson. Numerical instabilities in topology optimization: A survey on procedures dealing with checkerboards, mesh-dependencies and local minima. *Structural Optimization*, 16(1):68–75, 1998.

[58] S. Sleesongsom and S. Bureerat. Using Opposite-Based Population-Based Incremental Learning and Multigrid Ground Elements. *Mathematical Problems in Engineering*, 2015:16, 2015.

[59] S. Sleesongsom, S. Bureerat, and K. Tai. Aircraft morphing wing design by using partial topology optimization. *Structural and Multidisciplinary Optimization*, 48:1109–1128, 2013.

[60] M. J. Smith, N. Komerath, R. Ames, and O. Wong. Performance analysis of a wing with multiple winglets. In *19th Applied Aerodynamics Conference*. American Institute of Aeronautics and Astronautics, Inc., 2001.

[61] J. Sodja, M. J. Martinez, J. C. Simpson, and R. De Breuker. Experimental Evaluation of the Morphing Leading Edge. In *23nd AIAA/AHS Adaptive Structures Conference*, Kissimmee, Fl, 2015. American Institute of Aeronautics and Astronautics, Inc.

[62] M. Stolpe and K. Svanberg. An alternative interpolation scheme for minimum compliance topology optimization. *Structural and Multidisciplinary Optimization*, 22:116–124, 2001.

[63] K. Svanberg. The method of moving asymptotes a new method for structural optimization. *International Journal for Numerical Methods in Engineering*, 24:359–373, 1987.

[64] K. Svanberg. A class of globally convergent optimization methods based on conservative convex separable approximations. *SIAM Journal on Optimization*, 12(2):555–573, 2002.

[65] G. A. A. Thuwis, M. M. Abdalla, and Z. Gürdal. Optimization of a variable-stiffness skin for morphing high-lift devices. *Smart Materials and Structures*, 19(12):1–10, 2010.

[66] G. A. A. Thuwis, R. De Breuker, and J. Simpson. Conceptual design of an actuation system for a morphing leading edge high-lift device using topology optimisation. In *22nd International Conference on Adaptive Structures and Technologies (ICAST)*, Corfu, Greece, 2011.

[67] B. Trease and S. Kota. Adaptive and controllable compliant systems with embedded actuators and sensors. *Proceedings of SPIE*, 6525:13, 2007.

[68] N. Ursache, T. Melin, A. Isikveren, and M. I. Friswell. Morphing Winglets for Aircraft Multi-phase Improvement. In *7th AIAA Aviation Technology Integration and Operations Conference (ATIO)*, Belfast, Northern Ireland, 2007. American Institute of Aeronautics and Astronautics, Inc.

[69] R. Vos, J. Scheepstra, and R. Barrett. Topology optimization of pressure adaptive honeycomb for a morphing flap. In *Active and Passive Smart Structures and Integrated Systems 2011*. SPIE, 2011.

[70] F. Wang, B. S. Lazarov, and O. Sigmund. On projection methods, convergence and robust formulations in topology optimization. *Structural and Multidisciplinary Optimization*, 43(6):767–784, 2011.

[71] E. White, B. Rawdon, Z. Hoisington, and C. Droney. Aircraft with movable winglets and method of control, 2014.

[72] J. Wittmann, M. Hornung, and H. Baier. Mission performance optimization via morphing wing tip devices. In *Proc. DGLR - 2010*, Hamburg, Germany, 2010.

[73] T. Xinxing, G. Wenjie, S. Chao, and L. Xiaoyong. Topology optimization of compliant adaptive wing leading edge with composite materials. *Chinese Journal of Aeronautics*, 27(6):1488–1494, 2014.

[74] M. Zhang, R. Nangia, S. Ricci, and A. Rizzi. Design and Shape Optimization of Morphing Winglet for Regional Jetliner. In *2013 Aviation Technology, Integration, and Operations Conference*, Los Angeles, CA, 2013. American Institute of Aeronautics and Astronautics, Inc.

A

ABAQUS INPUT FILE 3D VON MISES TRUSS

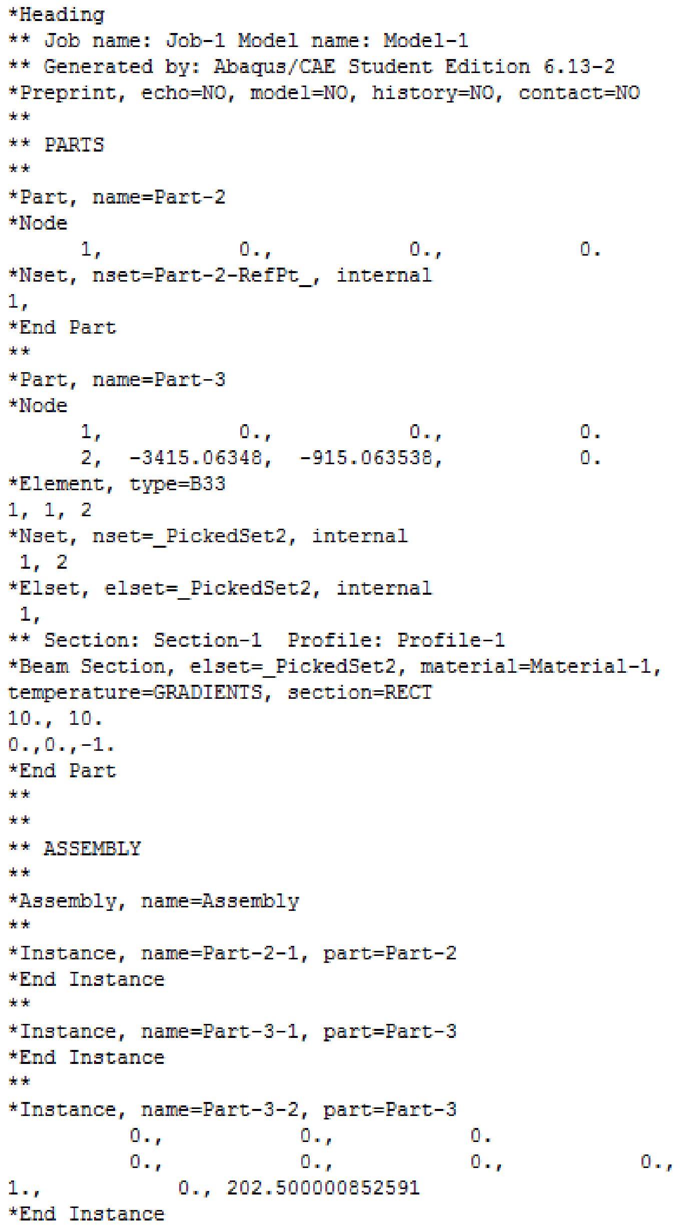

```
*Heading
** Job name: Job-1 Model name: Model-1
** Generated by: Abaqus/CAE Student Edition 6.13-2
*Preprint, echo=NO, model=NO, history=NO, contact=NO
**
** PARTS
**
*Part, name=Part-2
*Node
      1,           0.,           0.,           0.
*Nset, nset=Part-2-RefPt_, internal
1,
*End Part
**
*Part, name=Part-3
*Node
      1,           0.,           0.,           0.
      2,  -3415.06348,  -915.063538,           0.
*Element, type=B33
1, 1, 2
*Nset, nset=_PickedSet2, internal
 1, 2
*Elset, elset=_PickedSet2, internal
 1,
** Section: Section-1  Profile: Profile-1
*Beam Section, elset=_PickedSet2, material=Material-1,
temperature=GRADIENTS, section=RECT
10., 10.
0.,0.,-1.
*End Part
**
**
** ASSEMBLY
**
*Assembly, name=Assembly
**
*Instance, name=Part-2-1, part=Part-2
*End Instance
**
*Instance, name=Part-3-1, part=Part-3
*End Instance
**
*Instance, name=Part-3-2, part=Part-3
          0.,           0.,           0.
          0.,           0.,           0.,           0.,
1.,           0., 202.500000852591
*End Instance
```

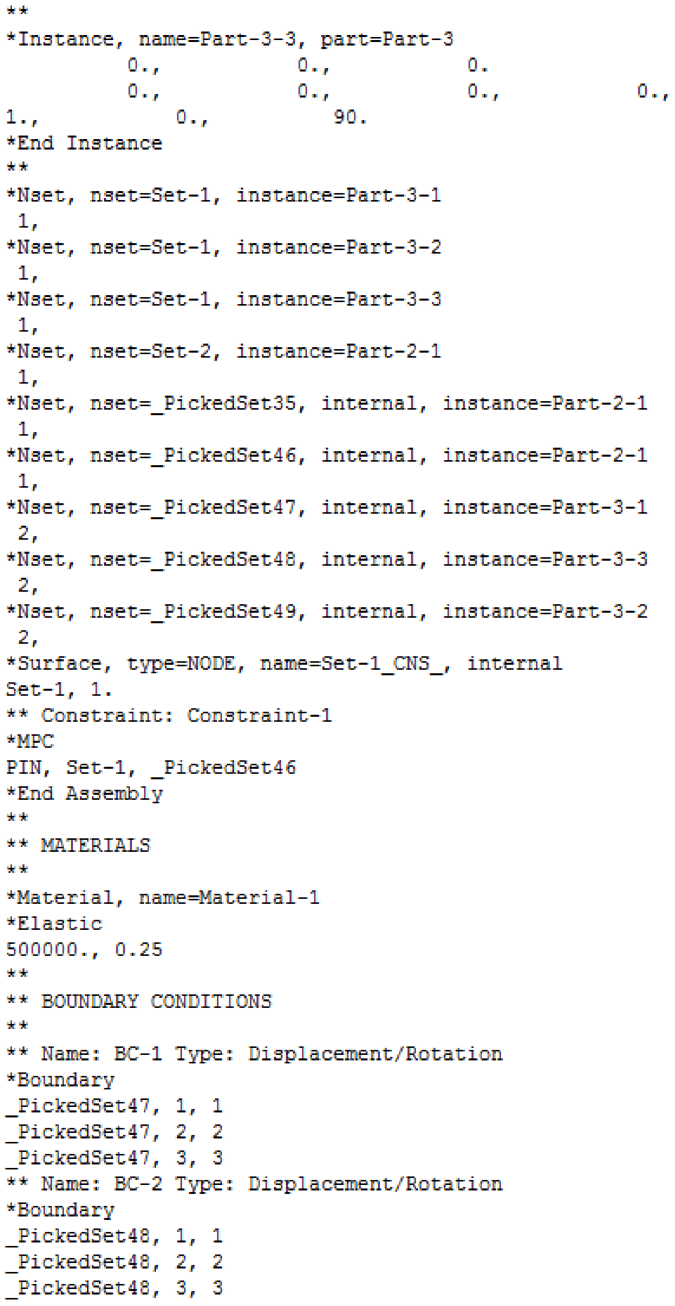

```
**
*Instance, name=Part-3-3, part=Part-3
          0.,           0.,           0.
          0.,           0.,           0.,           0.,
1.,           0.,          90.
*End Instance
**
*Nset, nset=Set-1, instance=Part-3-1
 1,
*Nset, nset=Set-1, instance=Part-3-2
 1,
*Nset, nset=Set-1, instance=Part-3-3
 1,
*Nset, nset=Set-2, instance=Part-2-1
 1,
*Nset, nset=_PickedSet35, internal, instance=Part-2-1
 1,
*Nset, nset=_PickedSet46, internal, instance=Part-2-1
 1,
*Nset, nset=_PickedSet47, internal, instance=Part-3-1
 2,
*Nset, nset=_PickedSet48, internal, instance=Part-3-3
 2,
*Nset, nset=_PickedSet49, internal, instance=Part-3-2
 2,
*Surface, type=NODE, name=Set-1_CNS_, internal
Set-1, 1.
** Constraint: Constraint-1
*MPC
PIN, Set-1, _PickedSet46
*End Assembly
**
** MATERIALS
**
*Material, name=Material-1
*Elastic
500000., 0.25
**
** BOUNDARY CONDITIONS
**
** Name: BC-1 Type: Displacement/Rotation
*Boundary
_PickedSet47, 1, 1
_PickedSet47, 2, 2
_PickedSet47, 3, 3
** Name: BC-2 Type: Displacement/Rotation
*Boundary
_PickedSet48, 1, 1
_PickedSet48, 2, 2
_PickedSet48, 3, 3
```

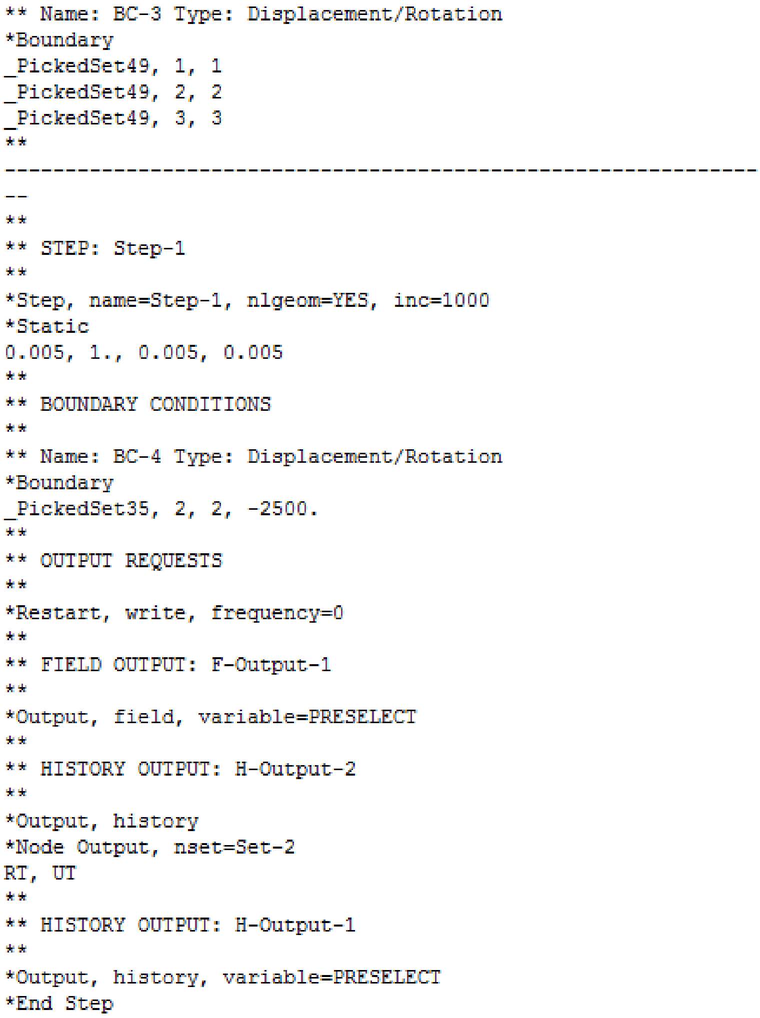

```
** Name: BC-3 Type: Displacement/Rotation
*Boundary
_PickedSet49, 1, 1
_PickedSet49, 2, 2
_PickedSet49, 3, 3
**
--------------------------------------------------------------
--
**
** STEP: Step-1
**
*Step, name=Step-1, nlgeom=YES, inc=1000
*Static
0.005, 1., 0.005, 0.005
**
** BOUNDARY CONDITIONS
**
** Name: BC-4 Type: Displacement/Rotation
*Boundary
_PickedSet35, 2, 2, -2500.
**
** OUTPUT REQUESTS
**
*Restart, write, frequency=0
**
** FIELD OUTPUT: F-Output-1
**
*Output, field, variable=PRESELECT
**
** HISTORY OUTPUT: H-Output-2
**
*Output, history
*Node Output, nset=Set-2
RT, UT
**
** HISTORY OUTPUT: H-Output-1
**
*Output, history, variable=PRESELECT
*End Step
```